TOTAL LIGHTNING CHARACTERISTICS OF ORDINARY CONVECTION

A Thesis

by

SHANE MICHAEL MOTLEY

Submitted to the Office of Graduate Studies of
Texas A&M University
in partial fulfillment of the requirements for the degree of

MASTER OF SCIENCE

August 2006

Major Subject: Atmospheric Sciences

TOTAL LIGHTNING CHARACTERISTICS OF ORDINARY CONVECTION

A Thesis

by

SHANE MICHAEL MOTLEY

Submitted to the Office of Graduate Studies of
Texas A&M University
in partial fulfillment of the requirements for the degree of

MASTER OF SCIENCE

Approved by:

Chair of Committee,	Larry Carey
Committee Members,	Richard Orville
	Benjamin Giese
Head of Department,	Richard Orville

August 2006

Major Subject: Atmospheric Sciences

ABSTRACT

Total Lightning Characteristics of Ordinary Convection. (August 2006)

Shane Michael Motley, B.S., University of California at Davis

Chair of Advisory Committee: Dr. Larry D. Carey

Twenty-two isolated, non-severe, warm season thunderstorms (ordinary thunderstorms) were examined to test possible correlations between three-dimensional lightning flash characteristics and the complex evolution of the microphysical and kinematic processes involved in the electrical development of thunderstorms. Nine of the thunderstorm cases examined occurred within range of Vaisala Inc.'s Dallas-Fort Worth (DFW) Lightning Detection and Ranging (LDAR) network and the other thirteen cases occurred within range of the Texas A&M University Houston LDAR Network. Cloud-to-ground (CG) flash data were obtained from the National Lightning Detection Network (NLDN). The kinematic and microphysical properties of each convective cell were inferred from level II Weather Surveillance Radar 1988-Doppler data.

Lightning properties were compared to radar reflectivity, Vertically Integrated Liquid, Severe Hail Index, and Vertically Integrated Ice (VII) (i.e. the measure of the precipitation ice water content in and above the mixed phase (-40°C < T < -10° C zone). In addition, total lightning (intra-cloud (IC) and CG) characteristics were compared against CG lightning characteristics to determine if total lightning data provide stronger correlations to convective intensity and state (i.e., developing, mature, dissipating) than CG lightning data alone.

The results show that VII is well correlated to the total flash rate with r^2 values of 0.45 and 0.81 for Houston and Dallas cases, respectively, whereas CG flashes show much weaker correlations to VII. The cases also follow the conventional model of lightning within ordinary storms with IC dominating over CG lightning in the initial stages of convective development. An average of 19 IC flashes occur before the first CG flash with an average lead-time between the first IC to the first CG of 12 minutes. Flash heights showed little correlation to VII, which is in disagreement with past studies suggesting that strong correlations exist between flash heights and storm intensity.

Integration of the results from this study into an operational forecast setting could lead to improvements in the nowcasting of lightning threats using radar, numerical weather prediction via assimilation of total lightning data, and the nowcasting of severe weather and lightning hazards to aviation.

ACKNOWLEDGMENTS

I would like to give a sincere thank you to my committee chair, Dr. Larry Carey, and committee members, Dr. Richard Orville and Dr. Benjamin Giese. Without their continuous support, advice, and direction none of this would have been possible. Thank you to Martin Murphy and Nick Demetriades of Vaisala for providing a large portion of the data used in this study and the technical support they offered during the course of our study. I also would like to thank Brandon Ely and Jerry Guyness for their development of the Texas A&M University LDAR system, which provided the majority of the data for this project.

I also have my peers to thank for their help, motivation, and source of continuous entertainment during stressful times. I would like to individually acknowledge Brandon Ely and Scott Steiger for their patience and willingness to help with the various questions that developed throughout the thesis.

I owe my deepest debt of gratitude to my family. They have provided me with continuous support and encouragement that helped me get through the most difficult times throughout my academic career. Thank you everyone for making this possible.

TABLE OF CONTENTS

Page

ABSTRACT……..... iii

ACKNOWLEDGMENTS…..……..... v

TABLE OF CONTENTS…….……..... vi

LIST OF TABLES…….....….…..... viii

LIST OF FIGURES……...……..... x

1. INTRODUCTION AND MOTIVATION ...……..... 1

1.1 Lightning and Its Importance……..... 1
1.1.2 Motivation via Past Work……..... 4
1.1.2.1 Past Research Utilizing Total Lightning Data……..... 6
1.2 Idealized Ordinary Convective Cells……..... 8
1.2.1 Cumulus Stage……..... 9
1.2.2 Mature and Dissipating Stage……..... 11
1.3 Past Studies Motivating the Non-Inductive Charge Hypothesis…..... 11
1.3.1 Charging Mechanisms……..... 13
1.3.1.1 Inductive Charging……..... 14
1.3.1.2 Non-Inductive Charging……..... 15
1.4 Thunderstorm Charge Structure……..... 22
1.4.1 Lightning Development and Propagation……..... 26
1.5 Hypothesis and Related Questions……..... 30

2. DATA AND METHODOLOGY……...……..... 33

2.1 Lightning Detection and Ranging Network……..... 33
2.1.1 VHF Flash Data……..... 45
2.2 National Lightning Detection Network……..... 47
2.3 Radar Data……..... 49
2.3.1 Weather Surveillance Radar -1988 Doppler (WSR-88D)…….... 49
2.3.2 Environmental Conditions Relating to Radar Reflectivity…….... 53
2.3.3 Radar Reflectivity Parameters……..... 54
2.3.4 Individual Cell Tracking Via Radar……..... 58
2.4 Convective Cell Bounds……..... 60
2.5 Statistics Performed……..... 64
2.6 Environmental Conditions……..... 66

Page

3. RESULTS……..……..... 68

3.1 Cell Locations……..... 68
3.1.1 Synoptic Setup……..... 72
3.2 Evolution of Lightning, Kinematics and Microphysics in Ordinary Convective Cells……..... 77
3.2.1 Dallas Fort-Worth Cases……..... 77
3.2.1.1 27 June 2001……..... 77
3.2.1.2 22 July 2005……..…..... 101
3.2.1.3 05 August 2005……..... 102
3.2.1.4 06 August 2005……..…..... 105
3.2.2 Houston Cases……..…..... 107
3.2.2.1 20 August 2005……..... 107
3.2.2.2 25 August 2005……..... 111
3.2.2.3 13 September 2005……..... 113
3.3 Integrated Results and Trends……..... 116

4. DISCUSSION……..... 127

4.1 Comparisons to Conventional Model of Lightning and Cell Evolution……..... 127
4.1.2 Bimodal Distributions in VHF Source Densities……..... 133
4.1.3 Flash Heights……..... 134
4.1.4 Location of Upper Positive Charge Region……..... 137
4.1.5 Correlations Between Total Flash Characteristics and Radar Parameters……..... 137
4.1.6 Benefits of Total, Over CG, Lightning Data……..... 141
4.1.7 CG Lead Times……..... 143

5. CONCLUSIONS. ……..... 145

REFERENCES……..……..... 149

APPENDIX A……..... 158

VITA..... 165

LIST OF TABLES

TABLE Page

1 Weather-related deaths per year in last 30 years (1959-1990), and death and injury totals in 1994 (adapted from Curran et al. 2000). Data were obtained from the National Oceanic and Atmospheric Administration (NOAA) *Storm Data* publication…… 3

2 The time span between cell initiation and the time at which the average 30 dBZ contour crosses the -10° C isotherm (INTN TO -10°C) for all 22 cases…… 69

3 Columns from left to right: The cell identification number of all 22 cells; month, day, and year cell developed; LDAR location cell occurred; maximum LDAR estimated total lightning flash rate (Max FR); average distance (Ave Dist) from center of respective LDAR network..... 70

4 The maximum flash rates observed from several studies examining ordinary non-severe thunderstorms (From Williams 2001)…… 71

5 Upper air conditions for each day examined showing values for Convective Available Potential Energy (CAPE); Convective Inhibition (CIN); 0-6 km shear, the height of the -10°C and -20°C isotherms, and the Bulk Richardson Number (R)……..... 76

6 The storm total IC/CG ratio (i.e. ratio between all IC flashes and all CG flashes for a given storm) for all 22 storms…….. 109

7 The time (hh:mm) from cell initiation to the time at which the average 30 dBZ contour crosses the -10° C isotherm. Average and standard deviation for all 22 case are listed at bottom of table……. 118

8 Times of initiation (INTN), first VHF source (1st VHF), first NLDN detected CG (1st CG), and the times between cell initiation and the first VHF source (1st VHF – INTN), the time between the first CG and cell initiation (1st CG – INTN), and the time between the first CG and first VHF source (1st CG – 1st VHF) with negative times representing the cases in which the first CG occurred prior to the first VHF source (Note: negative times treated as a zero minute lead time (i.e. 00:00) in averages). All times are reported in hh:mm format with INTN, 1st VHF, and 1st CG reported in UTC. The average for all Dallas cases (DFW average), Houston cases (HOU average) and

TABLE Page

cases combined (HOU and DFW average) are reported…….. 120

9 The times after initiation (h:mm) of maximum IC flash rates (max IC) and maximum CG flash rates (max CG). The time between the maximum IC and maximum CG flash rates are given showing most cases display maximum IC flash rates prior to maximum CG flash rates……... 128

LIST OF FIGURES

FIGURE Page

1 A conceptual model of the global electrical circuit. The constant positive conduction current to the ground, which occurs in fair weather, is generally attributed to thunderstorm generation. Thunderstorms act as the generators responsible for driving current from the earth back into the electrosphere. R_c is the columnar resistance, which is greater in the lower atmosphere. Typical altitudes are shown, which are not drawn to scale. (Source: MacGorman and Rust, 1998)…….. 2

2 Idealized model of ordinary thunderstorm showing (a) The towering cumulus stage, (b) mature stage, and (c) dissipating stage. Velocity vectors (arrows) and temperature/height profiles for the idealized case are shown (From Ray 1986, p. 333)……. 10

3 Depiction of the polarity of charge gained by graupel as a function of temperature and liquid water content (LWC) disagreement between Takahashi (1978) and Saunders et al. (1991). The bold dashed lines show the values of temperature and LWC at which the charge on graupel changed polarity as measured by Saunders et al. Curved lines show the charge gained (values in fC) by graupel as a function of LWC and temperature by Takahashi (1978). (From MacGorman and Rust 1998, p. 67)…… 18

4 A schematic model showing the two major stages of charge accumulation in thunderstorms. The developing stage shows graupel (triangle) charging negatively and snow crystals (hexagons) charging positively. The heavier graupel particles descend and as they fall below the -10° C level they are electrified positively (snow crystals negative) due to riming electrification. This results in a tripole structure of charge. (from Takahashi 1984)…… 20

5 Tripole structure of a thunderstorm with upper and lower positive (+) charge regions and main negative (-) charge region (from MacGorman and Rust 1998)…….. 23

6 Charge distributions from electric field (E) soundings showing multiple charge regions within the convective updrafts of three types of thunderstorms. Vertical dashed

FIGURE Page

lines represent an electric field sounding (labeled with year and Julian day –yyddd- along horizontal axis). Values to the right of the date information show balloon ascent rate between surface and 12 km in ms^{-1} (or top of sounding, if below 12 km). Negative (positive) charge layers are represented by solid (open) ellipses, with larger ellipses for layers deeper than 1 km. Surface heights are indicated by horizontal bars. Short slanted lines indicate heights of 0°, -10°, and -20°C in each sounding. (From Stolzenburg et al. 1998)…….. 25

7 Four types of lightning effectively transferring cloud charge to ground. Only the initial leader is shown for each of the four types with the direction of leader propagation and polarity of cloud charge effectively lowered to the ground shown (From Rakov and Uman 2003)…… 27

8 Illustration showing the cloud-to-ground lightning flash process (from Uman 1987)…… 29

9 Map depicting the locations of the seven Dallas LDAR sensors (green circles). Large black ring surrounding the network depicts a 100 km range from the center of the network…… 34

10 Map depicting the locations of the twelve Houston LDAR sensors (colored circles). The green circles represent sensors that were in operation during the time of this study, while the red circled are sensors that were inoperable and/or partially installed. The large black ring surrounding the network depicts a 100 km range from the center of the network. The red outline shows the Houston Urban area and industrial suburbs…… 35

11 Time-of-arrival system showing location of ground strike. The hyperbola on which a lightning flash is located is defined by the time at which the signal arrives at two or more stations. The intersection of hyperbolas from two different stations define the location of the strike (from MacGorman and Rust, 1998)…….. 37

12 Composite reflectivity scan from the WSR-88D KHGX radar on October 31, 2005 at 22:43 UTC *(Source: NOAA NCDC)*……. 40

13 Altitude (km) versus radial distance from center of the

FIGURE Page

Houston LDAR network of VHF sources detected in a 1 km thick slice for the time period of 19Z on 10/31/05 to 03Z on 11/01/05. Slice oriented parallel to the convective line from the center of the network as shown in fig 2.8. Notice the dramatic drop off of sources at approximately 135 km. *Source: Ely et al. (2006*)…… 41

14 Scatter plot (Red points = Dallas; Blue points = Houston) showing correlations between the number of sources per flash and the distance of a cell from the center of the network for Houston and Dallas network…… 44

15 WSR-88D Volume Coverage Pattern 11 (VCP-11). Scanning strategy consists of 14 elevation scans in approximately 5 minutes (from http://www.srh.noaa. gov/radar/radinfo/)……..... 50

16 WSR-88D Volume Coverage Pattern 21 (VCP-21). This scanning strategy consists of 9 scans in 6 minutes (from http://www.srh.noaa.gov/radar/radinfo/)…… 51

17 3-D depiction of radar reflectivity, dBZ shown. a) Vertical cross section taken through a cell occurring on 27 June 2001 during peak intensity at 1457 UTC (t = 35 minutes). Shaded cylinder constructed around cell shows bounds of the cell. Cross-section grid box spacing is 4km in the vertical plane and 5km in the horizontal plane. (b) Same as (a), but for cell 1 with vertical cross section taken during peak intensity at 1825 UTC (t = 40) minutes)…….. 61

18 Location (red diamonds) and cell identification numbers from Table 2 for the nine cases examined in Dallas. Green circles represent location of LDAR sensors. Black ring represents 100 km range from center of the LDAR network…… 73

19 Same as Figure 18, but for all 13 Houston cases. Note: the two red circles represent inoperable sensors during period of study…….. 74

20 Three panel plots (labeled a, b, and c) for case 1 where: a) Time (after cell initiation) height (km) cross sections of VHF source density (colored shading), flash origin

FIGURE Page

locations (x), CG times (*) and radar reflectivity (dBZ, contoured starting at 5 dBZ every 5 dBZ). b) 5-minute running average of lightning flash rate for total lightning data (blue line), CG flash rate (red line), and the 75th percentile (green line) and median (orange line) of flash heights. c) Vertically Integrated Liquid (VIL, kg m^{-2}; green line), Severe Hail Index (SHI, J m^{-1} s^{-1}; red line), and Vertically Integrated Ice (VII) mass (kg*10^{6}; Blue line) integrated from the height of the -10° C isotherm to echo top multiplied through by cell area and 10^{-6}…… 78

21 Same as Fig. 20, but for case 2……. 79

22 Same as Fig. 20, but for case 3……..... 80

23 Same as Fig. 20, but for case 4. …….. 81

24 Case 5, which is the same as Fig. 20 except for the addition of the 95th (light blue line) and median (dark red line) flash heights in frame b.. …….. 82

25 Same as Fig. 20, but for case 6. . ……...……. 83

26 Same as Fig. 20, but for case 7. . …….…… 84

27 Case 8, which is the same as Fig. 20 except for the addition of the 95th (light blue line) and median (dark red line) flash heights in frame b. ..... . ……. 85

28 Same as Fig. 20, but for case 9. . …… 86

29 Same as Fig. 20, but for case 10. . …….. 87

30 Same as Fig. 20, but for case 11. …… 88

31 Same as Fig. 20, but for case 12. …… 89

32 Same as Fig. 20, but for case 13. …… 90

33 Same as Fig. 20, but for case 14. …… 91

34 Same as Fig. 20, but for case 15. …… 92

35 Same as Fig. 20, but for case 16. …… 93

FIGURE Page

36 Same as Fig. 20, but for case 17. …… 94

37 Same as Fig. 20, but for case 18. …… 95

38 Same as Fig. 20, but for case 19. …… 96

39 Same as Fig. 20, but for case 20. …… 97

40 Same as Fig. 20, but for case 21. …… 98

41 Same as Fig. 20, but for case 22. …… 99

42 The maximum radar reflectivity (dBZ) in a given volume scan versus total flash rate (flashes min^{-1})…….. 123

43 Rate of ascent (km min^{-1}) of 20 dBZ contour from the point at which it crosses the -20° C contour to the time of peak flash rate……. 124

44 a) Scatter plot of the total flash rate (flashes min^{-1}) vs. vertically integrated ice mass (kg) multiplied by cell area and 10^{-6} for both Dallas and Houston cases. Red points indicate individual data values for Dallas and blue points indicate individual data values for Houston. The red and blue lines represent the equation of best fit for Dallas and Houston data, respectfully. The R squared values are also displayed for both Dallas (red) and Houston (blue) showing strong correlations between the total flash rate and vertically integrated ice mass. This strong correlation is likely attributed to increase in charge that occurs with an increase in the ice available for non-inductive charging. b) Same as (a), but with CG flash rate for both Dallas (red points) and Houston (blue points)…….. 125

45 Plot of the IC/CG ratio as a function of the total flash rate showing the IC/CG ratio decreases for decreasing total flash rate. (From Rutledge et al. 1992)……. 131

46 Scatter plot of VII versus 75th percentile heights for all 22 cases. . …… . ..…… ……. 136

47 Similar to Fig. 44 except with the exclusion of case 7……. 142

FIGURE Page

A1 Similar to figure 44 except values of Z_e^{ice} are adjusted by ±3 dB in eqn. (14). -3 dB means 3 dB were subtracted from the observed value of Z_e^{ice} and +3 dB means 3 dB were added to the observed value of Z_e^{ice}. Houston points are represented by blue (purple) diamonds for +3 dB (-3 dB) and Dallas points are represented by short, red (orange) lines for +3 dB (-3 dB) all of which are visible. Best-fit lines are shown for each scatter with the area spanning the slopes Houston (Dallas) highlighted in blue (red)……..... 162

A2 Similar to A1 except for different values of ρ_i……. 163

A3 Similar to A1 except for different values of N_o…… 164

1. INTRODUCTION AND MOTIVATION

1.1 Lightning and Its Importance

Lightning, because of its ability to injure, kill, and cause extensive property damage, is a significant concern to weather forecasters and the public alike. Lightning is defined as a self-propagating atmospheric electrical discharge that results from the accumulation of positive and negative space charge, typically occurring within convective clouds (Uman, 1986). This electrical breakdown plays a key role in the global electrical circuit, which drives fair weather current leaked from the ionosphere to Earth, back up into the ionosphere (Fig 1).

However, even with over one hundred years worth of lightning related studies, questions regarding how charge separation occurs in thunderstorms, especially to the point of electrical breakdown, still remain. These lingering unknowns lead to the potential for significant lightning related hazards. For example, the National Lightning Safety Institute (NLSI) estimates lightning related damage in the 4-5 billion dollar range annually across the United States. Cloud-to-ground (CG) lightning is also the number two killer in convective weather related fatalities, only to be surpassed by flash flooding (Curran et al. 2000) (Table 1). Investigating the unknowns involved in thunderstorm electrification and lightning may help alleviate the risk of lightning related fatalities, aviation mishaps, fires, and other lightning related dangers.

This thesis follows the style of Atmospheric Research.

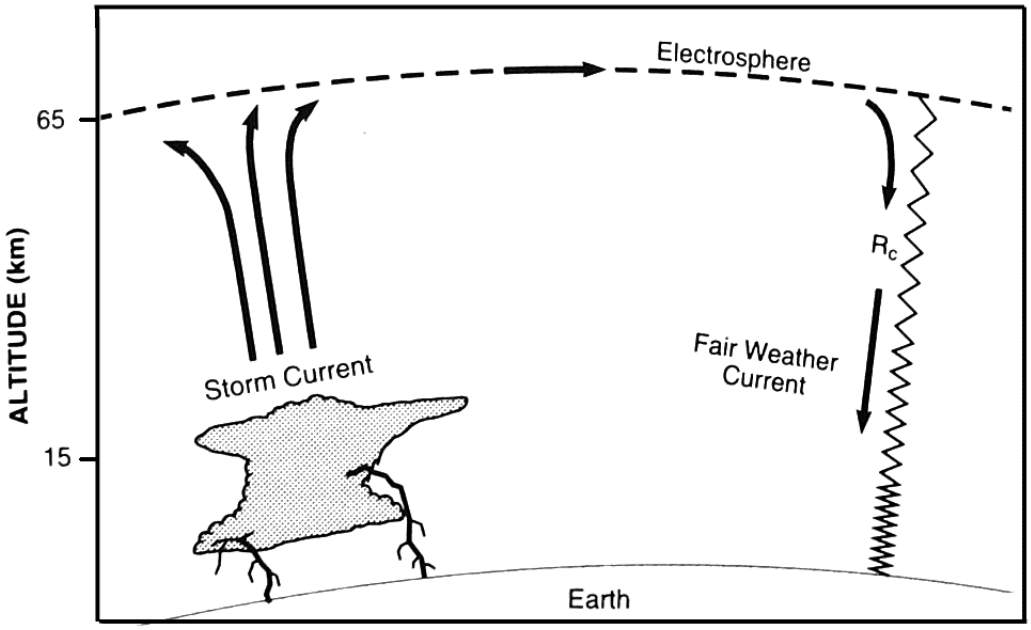

Fig. 1. A conceptual model of the global electrical circuit. The constant positive conduction current to the ground, which occurs in fair weather, is generally attributed to thunderstorm generation. Thunderstorms act as the generators responsible for driving current from the earth back into the electrosphere. R_c is the columnar resistance, which is greater in the lower atmosphere. Typical altitudes are shown, which are not drawn to scale. (Source: MacGorman and Rust, 1998)

Table 1. Weather-related deaths per year in last 30 years (1959-1990), and death and injury totals in 1994 (adapted from Curran et al. 2000). Data were obtained from the National Oceanic and Atmospheric Administration (NOAA) *Storm Data* publication.

Weather Type	30-yr deaths per year	1994 deaths	1994 injuries
Flash Flood	139	59	33
River Flood		32	14
Lightning	87	69	484
Tornado	82	69	1067
Hurricane	27	9	45
Extreme Temperature		81	298
Winter Weather		31	2690
Thunderstorm Wind		17	315
Other High Wind		12	61
Fog		3	99
Other		6	59
Total		388	5165

1.1.2 Motivation via Past Work

Given the obvious threat that CG lightning poses to life and property, several studies have focused on the possible correlations between CG lightning and various parameters provided by operational radar (e.g. Buechler and Goodman 1990; Watson et al. 1995; Gremillion and Orville 1999; Vincent et al. 2003). Buechler and Goodman (1990) examined the ability of the National Weather Service's (NWS) Weather Surveillance Radar 1988 Doppler (WSR-88D) to identify and track convective cells capable of producing lightning. They discovered the storm tracking algorithms used by the WSR-88D were inadequate for identifying and tracking small, potentially hazardous, thunderstorms. The inability of the algorithm to adequately identify or track storms prior to lightning production was attributed to the heavy emphasis the algorithm places on the radial length of the 30 dBZ contour at the lowest (0.5°) scan. Lightning can occur before the specified threshold triggers the tracking of a cell (Goodman et al. 1988; Dye et al. 1989), thereby lowing the probability of detection.

Watson et al. (1995) examined potential correlations between the vertical integral of liquid water content and CG lightning flash rates with inconclusive results. Gremillion and Orville (1999) displayed more promising results toward the ability to forecast the onset of CG lightning by examining the evolution of radar reflectivity heights for 39 non-severe Florida thunderstorms. They determined that CG lightning occurred with an 84% POD and 7% FAR when radar reflectivity values of 40 dBZ occurred at or above the -10° C isotherm. However, Dye et al. (1988) points out that the microphysics driving thunderstorm electrification may vary across different geographic regions, which could result in the onset of electrification occurring at substantially different reflectivity values.

Vincent et al. (2003), however, show similar results to Gremillion and Orville (1999) in 50 North Carolina thunderstorms in which the onset of CG activity occurs with a 100% POD and 37% FAR after the 40 dBZ echo reaches the -10° C isotherm. Another study of 28 Florida thunderstorms by Hondl and Eilts (1994) suggest that the 10 dBZ echo detected near the freezing level might serve as an indicator of a developing thunderstorm. However, the location of the 10 dBZ echo at the 0° C isotherm is easily reached with most convective and non-convective cells, therefore limiting the use of this parameter to summer thunderstorms over Florida. In addition, several polarimetric radar studies of isolated Florida thunderstorms suggest the driving force behind significant electrification is closely tied to the freezing of supercooled raindrops, which may or may not be coincident with a 10 dBZ echo at the 0° C isotherm (e.g. Jameson et al. 1996; Bringi et al. 1997).

Although these studies provide very promising results for CG forecasting, CG lightning comprises only a small subset of the total lightning within a thunderstorm. Past research suggests the onset of total lightning (which includes intracloud (IC) and CG lightning) is related to both the kinematic and microphysical properties of a thunderstorm. Since these properties can be inferred by radar, it is possible that improvements in total lightning, rather than CG lightning alone, could be achieved. These improvements are essential to aviation forecasting that could help mitigate the lightning related hazards that are responsible for more than 50% of military aircraft weather-related in-flight mishaps (NLSI, 2006). In addition, total lightning information may also lead to improvements in the onset of CG lightning, which poses a significant threat to large outdoor public venues. It becomes obvious that improvements in total lightning

forecasting have the potential to provide significant benefits toward applications in which first flash information is crucial. Therefore, devising methods to associate the evolution of lightning to the convective intensity and state requires an accurate and detailed depiction of the three-dimensional (3-D) location of total lightning.

1.1.2.1 Past Research Utilizing Total Lightning Data

The ability to map out lightning in 3-D is made possible by monitoring the time of arrival of the VHF radiation produced by the above ground portions of both IC and CG lightning. Sensors used to monitor the radiation use time of arrival (TOA) techniques to pinpoint the location of the radiation sources. Multiple sources can be combined into a single flash by grouping sources based on assumed lightning propagation characteristics. Grouping multiple radiation sources into a single flash is performed by placing temporal and spatial constraints on multiple sources based on lightning propagation speeds. The sensor networks used in this study are called Lightning Detection and Ranging (LDAR) networks. With the advent of continuously operational three-dimensional (3-D) lightning mapping systems such as the LDAR networks, complete observations of a thunderstorm's lightning development are now routinely available.

Prior to the development of continuously operational systems, coordinated field studies were necessary to monitor and record total lightning characteristics of thunderstorms. Taylor et al. (1984) examined the total lightning data from four severe Oklahoma thunderstorms showing that intracloud lightning accounted for approximately 71% of the total lightning activity. Both Williams et al. (1989a) and Goodman et al. (1988) observed thunderstorms in which IC lightning dominated during the early stages

of convective development, with CG lightning activity lagging the initial IC activity by 5-10 minutes. Both studies also noted that the onset of IC activity occurs after a rapid increase in radar-inferred intensity above the mixed-phase zone, with CG activity occurring after the main reflectivity core begins to descend. Carey and Rutledge (1996) examined possible correlations between ice processes within convective clouds and thunderstorm electrification. Their results show that significant correlations exist between the CG flash rate and the graupel volume below the melting level, with peaks in the ice volume corresponding to peaks in the CG flash rate. They also show a strong correlation between the IC flash rate and graupel volume aloft. Proctor (1991) focused on the locations of VHF sources to show that the origin of flashes display a bimodal distribution with peaks occurring at 5.3 and 9.2 km amsl or -3.3° C and -27.7° C, which coincide with the location of main charge layers as will be discussed in subsequent sections.

More recent studies examining correlations between three-dimensional lightning flash characteristics and convective intensity (e.g. magnitude of updraft) and state (e.g. early, mature, and dissipating phases) have shown promising results; however, emphasis has focused primarily on complex modes of convection (e.g., supercells and squall lines), often with only a limited portion of the cell's life time examined. (e.g. Ray et al. 1987; Coleman et al. 2003; Lang et al. 2004a,b; Carey et al. 2005; Wiens et al. 2005; Steiger et al. 2005). Although it is the most ubiquitous and fundamental cell type, ordinary, single-cell convection has received relatively little recent attention in the lightning community. Placing an emphasis on ordinary convection allows for a more direct approach to the complex evolution of the microphysical and kinematic processes involved in the electrical development of thunderstorms.

1.2 Idealized Ordinary Convective Cells

A thunderstorm is formally defined as a convective cloud that produces lightning. This term, however, is often too general to describe the wide rage of thunderstorm types, which are classified into categories based on the storm's degree of severity, longevity, organization, or other related features. The kinematics and microphysics within a thunderstorm are controlled by various atmospheric parameters. Weisman and Klemp (1982) employed a three-dimensional numerical cloud model to examine various environmental parameters that may control the convective type. Two of these parameters, buoyancy and vertical wind shear, appeared to be the primary controls of convective type with high levels of shear and buoyancy typically leading to increasingly complex convective types (e.g. supercells, multicell convective complexes). Weisman and Klemp adopted a parameter combining buoyancy and shear, called the bulk Richardson number, R, to provide operational forecasters a quick means to assess the potential for various convective modes. The bulk Richardson number is given by:

$$R = \frac{B}{1/2U^2} \qquad (1)$$

where B is the buoyant energy in the storm's environment (J kg^{-1}) and U is a measure of the vertical wind shear (s^{-1}) (Ray 1986, p. 353). Results show that higher shear and buoyancy values tend to favor supercellular convective modes (or R between 10 and 40), while low shear and lower buoyancy values tend to favor ordinary multicellular convective modes (or R > 30). Byers and Braham (1949) conducted the first documented study on the internal structure of thunderstorms occurring in a convectively unstable, weakly sheared environment, which they referred to as "airmass" thunderstorms. As

shown by their study, the approximate 1 hour lifetime of the airmass thunderstorm consisted of one or more individual convective cells, with each cell undergoing three distinct stages: cumulus, mature, and dissipating.

1.2.1 Cumulus Stage

If a parcel of air is less dense than the surrounding air, it will rise with the potential to mark the first stages of convective development. This initial stage, which occurs for all convection, is the cumulus stage and denotes the beginning of a thunderstorm's updraft. According to Kingsmill and Wakimoto (1991), thermal gradients are the dominant force driving upward motions during the cumulus stage, which prevail throughout this period. A conceptual model of the cumulus stage of an idealized ordinary is shown in Fig. 2a. The image represents the vertical cross-section of a thunderstorm occurring in a weakly sheared environment during the cumulus stage of development and shows a strong updraft with both liquid and solid hydrometers present.

Goodman et al. (1988) and Tuttle et al. (1989) used radar observations to indicate that the initial precipitation development during this stage, within humid environments is dominated by collision-coalescence growth. The development of solid hydrometers typically occurs in the later stages of development (Tuttle et al. 1989; Kingsmill and Watkimoto 1991), as growth by accretion-freezing dominates, which is the process by which supercooled water droplets freeze upon contact of an ice hydrometer, resulting in growth. The presence of precipitation sized ice during this period often coincides with the first lightning discharges within the storm (e.g. Carey and Rutledge 1996). The entire

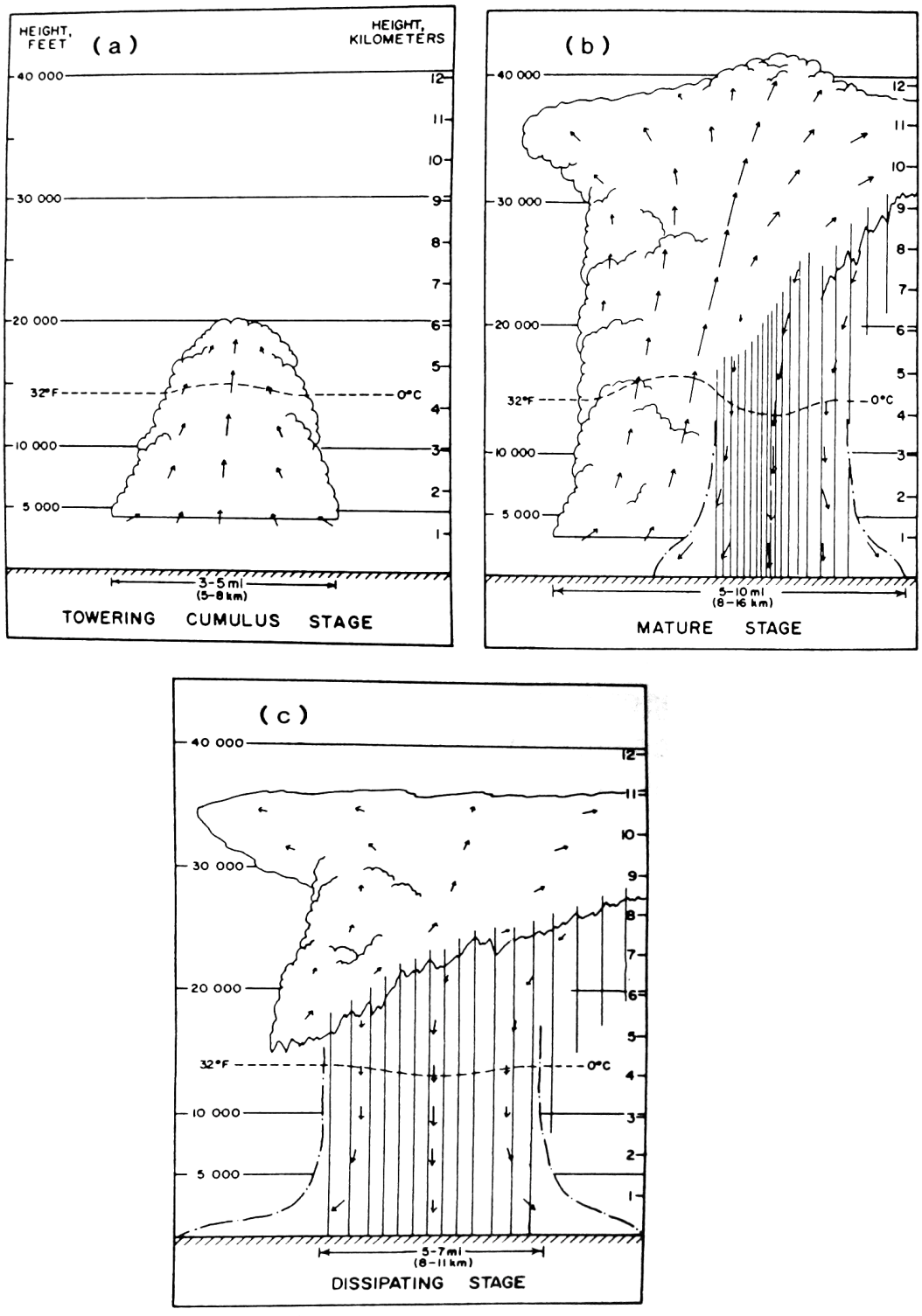

Fig. 2. Idealized model of ordinary thunderstorm showing (a) The towering cumulus stage, (b) mature stage, and (c) dissipating stage. Velocity vectors (arrows) and temperature/height profiles for the idealized case are shown (From Ray 1986, p. 333).

cumulus stage, according to Byers and Braham (1949), typically lasts between 10 and 15 minutes before the cell reaches the mature stage, which they define as the point at which precipitation reaches the ground.

1.2.2 Mature and Dissipating Stage

Kingsmill and Wakimoto (1991) define the onset of mature stage as the moment that the radar-detected precipitation core begins to descend. A conceptual model of the mature stage is shown in Fig 2b. At this time, the low level (between 0 and 2 km) flow field remains similar to that of the cumulus stage; however, at the midlevels (7 km) the flow field becomes much more complex as downdrafts become established and coexist with the main updraft. The descent of the precipitation core may be attributed to the immense amount of glaciation that occurs during this period (Tuttle et al. 1989). This leads to the development ice particles, which—if larger than a few millimeters—descend faster than raindrops (Prupacher and Klett 1978), thus leading to the core's descent. As rain continues to fall throughout the mature stage, the downdraft area increase in size until it eventually extends throughout the cell. This period marks the end of the mature stage and the beginning of the dissipating stage (Fig. 2c). At this point, the cell can no longer sustain an updraft, which eventually leads to a subsequent collapse of the storm and an end to its lifespan. This whole process typically lasts from 45-90 minutes.

1.3 Past Studies Motivating the Non-Inductive Charge Hypothesis

Several studies have shown the apparent correlation between the evolution of lightning and electric fields to the convective intensity and state, as seen in the kinematic

and microphysical fields, of a given storm. Lhermitte and Williams (1985) employed a triple-Doppler network to relate the radar reflectivity and motion fields to the structure of electrical discharges of a storm. Their research demonstrated that the lightning-producing negative charge centers were located just above (1 km or less) the level at which large precipitation particles were suspended (i.e. mean particle vertical velocities of zero) in the updraft.

Williams et al. (1989a) examined isolated convective storms in Alabama and found consistent relationships between the convective growth and lightning type. Their study documented the prevalence of IC over CG lightning during early stages of thunderstorm development, changing over to predominately CG lightning during later stages. Similar results were noted in a study conducted by Goodman et al. (1988) in which polarimetric radar was used for the first time to correlate the presence of graupel and hail to the total lightning flash rate. As in Williams et al. (1989a), Goodman et al. (1988) also documented the prevalence of IC lightning over CG lightning during the early stages of convective development, with CG lagging the initial IC activity by 5 minutes.

Carey and Rutledge (1996) also used polarimetric radar to examine the temporal evolution of the microphysical, kinematic, and electrical evolution within a multi-cellular convective storm in Colorado. They noted a strong correlation between the IC flash rate and the accumulation of graupel and hail particles suspended by vigorous updrafts. In addition, all three studies (Goodman et al. 1988; Williams et al. 1989a; and Carey and Rutledge 1996) noted a descent in the main precipitation core prior to the onset of CG flashes. Carey and Rutledge (1996) also noted peaks in the CG flash rates during periods

in which the graupel and hail were present within mixed phase precipitation below the freezing level of the storm. Williams et al. (1989a) also suggests the descent of ice provides an additional positive charge beneath the main negative charge region, which provides the electrical bias required to cause CG lightning.

These studies all showed trends that suggested the presence of ice within a thunderstorm is correlated to thunderstorm electrification. In examining this correlation, Carey and Rutledge (2000) used C-band polarimetric radar to test whether or not lightning production is linked to the presence of ice hydrometeors within the mixed phase region of convective cells. The results of their study concluded that lightning production is critically linked to ice processes. This particular study also noted CG lightning associated with the descent of graupel and frozen drops.

The fairly robust correlation between lightning and ice processes shown in past studies raises the questions regarding the role that ice plays within the process of thunderstorm electrification.

1.3.1 Charging Mechanisms

The transfer of charge between two conductors occurs when one rubs against the other within an electric field. This process is more complex within convective clouds, since cloud particles have a wide range of surface conductivities (Saunders, 1993). Therefore, given the complexities associated with thunderstorm electrification, we still do not fully understand how the electrification actually occurs. This has resulted in a number of theories, some of which continue to gain acceptance throughout the meteorological community.

1.3.1.1 Inductive Charging

Despite some controversy, a few studies suggest that the strong electric fields generated in a thunderstorm result from particles interacting in an existing electric field. This process is known as inductive charging, in which the pre-existing "fair weather" electric field owes its existence to the positive charge within the highly conductive region of the atmosphere called the ionosphere, the negative charge of the Earth's surface, and the less conductive portion of the atmosphere sandwiched between the two through which current continuously flows (MacGorman and Rust, 1998). Much of the controversy surrounding this theory stems from past results demonstrating that the vertical fair weather electric field, which is about 0.1 kV m^{-1} near the earth's surface (Rakov and Uman, 2003), is insufficient to account for the charging observed in thunderstorms (MacGorman and Rust 1998). Nevertheless, the two primary methods believed to be responsible for inductive charging are 1) Wilson's selective ion capture mechanism and 2) rebounding collisions of two polarized hydrometeors (MacGorman and Rust 1998). The ion capture method suggests that polarized falling hydrometeors selectively capture negative charge from ions as long as the hydrometer's velocity is greater than the ion's velocity. According to this principal, if the selective ion capture occurred between the positive and negative regions of a thunderstorm, precipitation particles would tend to capture negative charge, thus increasing the amount of charge in the negative charge region. However, in most thunderstorms having precipitation, ion densities are too low to account for the charges observed in thunderstorms (MacGorman and Rust 1998).

The second inductive charging mechanism suggests that the existing electric field acts to polarize cloud particles and precipitation particles, which upon colliding results in a transfer of charge between the two particles (Sartor 1954). Attempts to provide further support for this inductive charging theory have been somewhat problematic due to the number of conditions that the theory must satisfy. For example, Gaskell (1981) and Illingworth and Caranti (1985) showed that the brief contact time between ice crystals and graupel pellets is too short for the charge to flow between the two. Moreover, differential sedimentation of charged particles could actually lead to a decrease in thunderstorm charge if positively (negatively) charged particles move to negative (positive) charge regions. However, Gaskell et al. (1978), Christian et al. (1980), and Marshall and Winn (1982) show that graupel pellets carry charges much larger than can be explained by inductive charging. In addition, research has shown that this process can only account for thunderstorm electrification in the presence of electric fields greater than 10 kV m^{-1}, which is much higher than the 0.1 kV m^{-1} available from the fair weather current (Rakov and Uman 2003). Therefore, current evidence suggests that although the inductive charging may contribute to thunderstorm electrification, it can only become a significant contributor later in the development of the thunderstorm when the electric field has increased via other mechanisms (Saunders 1993; MacGorman and Rust 1998).

1.3.1.2 Non-Inductive Charging

Of all the hypothesized mechanisms attempting to explain thunderstorm charging, the most widely accepted theory is the non-inductive, graupel-ice charging mechanism first proposed by Reynolds et al. (1957), which occurs independently of the local electric

field strength. Early work by Reynolds et al. and colleagues showed that graupel pellets acquired a net negative charge upon collisions with ice crystals in the presence of supercooled liquid water and no charge transfer occurred in the absence of ice crystals. They suggested the charge transfer was due to a temperature difference between the ice crystals and graupel. Therefore, several studies sought to examine the effects of liquid water content and temperature on charging (e.g. Takahashi 1978; Gaskell and Illingworth 1980; Jayaratne et al. 1983).

These and other experiments examining the non-inductive charging hypothesis have shown that the amount and sign of charging on riming graupel pellets is dependant on several parameters. Laboratory studies of charge transfer to riming graupel by Takahashi (1978) show that the magnitude and sign of the charge deposited on the graupel depended on the temperature and liquid water content, results that were later generally confirmed by Saunders et al. (1991) even though specific differences were noted. In addition to the requirement that supercooled water droplets need to be present for charging to occur, laboratory experiments by Jayaratne et al. (1983) and Keith and Saunders (1990) suggested that charging also depended on the size of the ice crystal colliding with the graupel, the impact velocity, and any contaminates in the water particles.

Further work by Saunders and Brooks (1992) attempted to explain discrepancies in Takahashi's work related to the strength of charge at different liquid water contents and discrepancies in the sign of the charge in warm temperature, low liquid water situations (Fig. 3). The results did not provide conclusive evidence to resolve the latter

issue; however, they did determine that the cloud liquid water content was overestimated due to the liquid water measuring technique used in Takahashi's experimental setup.

This idea was explored further in a laboratory study by Saunders and Peck (1998), which suggested that the magnitude of charge depends on the crystal size and graupel velocity, while the sign of the riming graupel pellet is a function of the temperature and the rime accretion rate (RAR = EW × V), where EW is the equivalent liquid water content (i.e. adjusted liquid water content to account for droplets being swept around graupel pellets instead of colliding with them) and V is crystal/graupel relative velocity. In the case of temperature dependencies, when the temperature is below (above) a critical temperature value, the falling graupel particles take on a negative (positive) charge.

The rime accretion rate comes into play when considering the results by Jayaratne and Saunders (1985) and Baker et al. (1987), which showed that charging depended on the presence of liquid drops on the graupel surface and that droplets not colliding with the graupel had no effect on the charging of the graupel. Therefore, since the amount of water droplets colliding with the graupel in a given volume, rather than the amount of droplets alone, controls the charging of the graupel, the EW was developed as a better means to assess the potential charge of the graupel. Thus the amount of liquid water drops collected by riming graupel (the rime accretion rate), has an effect on the charge. Increases in the rime accretion rate can be achieved through an increase in the vertical

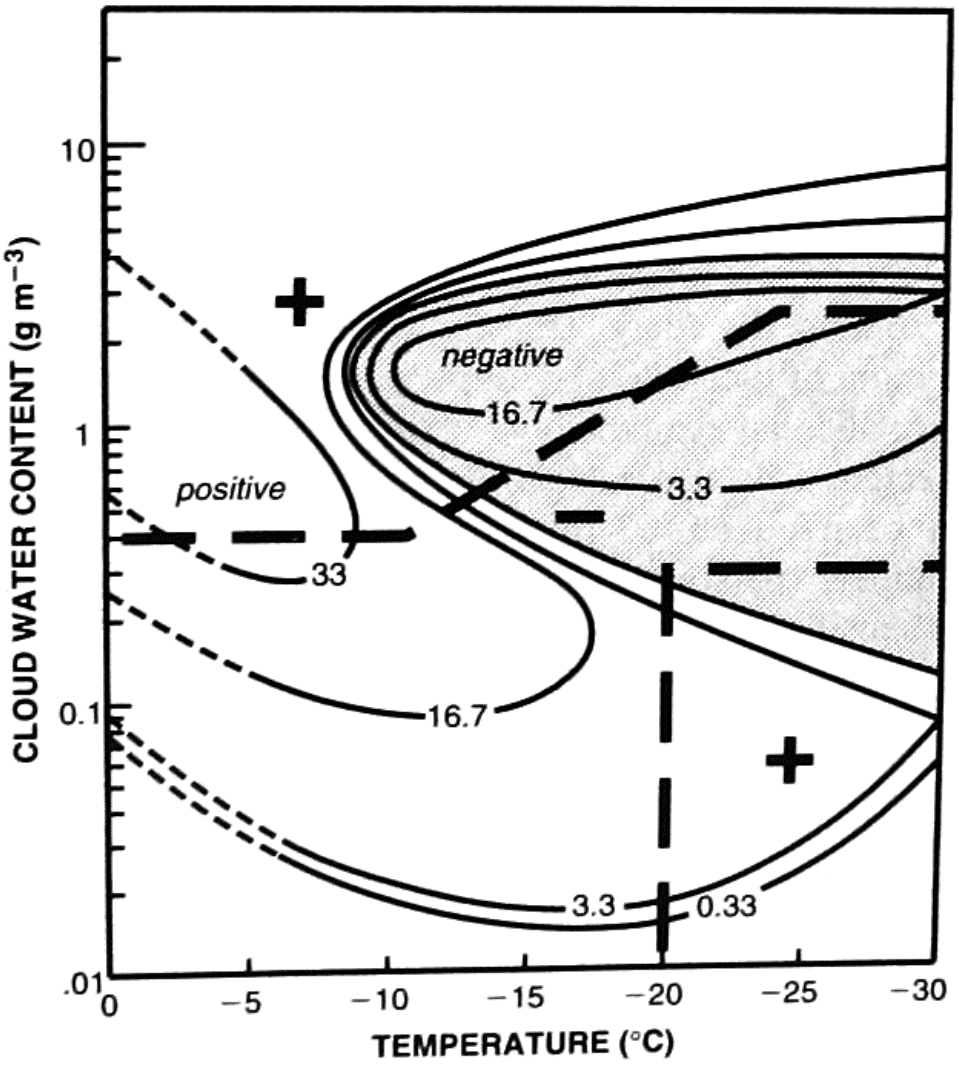

Fig. 3. Depiction of the polarity of charge gained by graupel as a function of temperature and liquid water content (LWC) disagreement between Takahashi (1978) and Saunders et al. (1991). The bold dashed lines show the values of temperature and LWC at which the charge on graupel changed polarity as measured by Saunders et al. Curved lines show the charge gained (values in fC) by graupel as a function of LWC and temperature by Takahashi (1978). (From MacGorman and Rust 1998, p. 67).

velocity of the graupel, or an increase in the liquid water content such that more drops are collected. Drop size distributions may also affect the rime accretion rate since very small droplets are more likely to be swept around the graupel leading to a decrease in the collection efficiency (Khain et al. 2001).

Research by Avila et al. (1995) suggests that the charge transfer to graupel may be directly related to the temperature contrast between graupel particles and the surrounding air. This temperature contrast, however, still accounts for dependencies of liquid water content since more drops leads to higher rime rates and more latent heat is released as drops freeze to the graupel. In the absence of liquid water drops, Avila et al. were able to produce similar charging of graupel based on temperature contrasts. Other mechanisms controlling the charge sign reversal may be attributed to the size of the ice particles colliding with the graupel.

The temperature at which charge reversal is located is generally thought to exist in close proximity to the main negative charge region, which usually lies between -10° C and -20° C (e.g. Williams 1989b; MacGorman and Rust 1998). Takahashi et al. (1999) suggest the sign reversal is paramount to the both tripole structure regions (positive charge above and below main negative charge) and the fixed height of the midlevel charge region (see Sec. 1.4). They attribute this to negatively charge ice crystals that are carried aloft by weak updrafts to combine with negatively charge graupel falling from above (Fig. 4), which enhances the mid level charge as precipitation increases. Above the main negative charge region the upward moving positively charged ice crystals enhance the upper positive charge region while positively charge graupel pellets falling below the main negative charge region help to enhance the lower positive charge region.

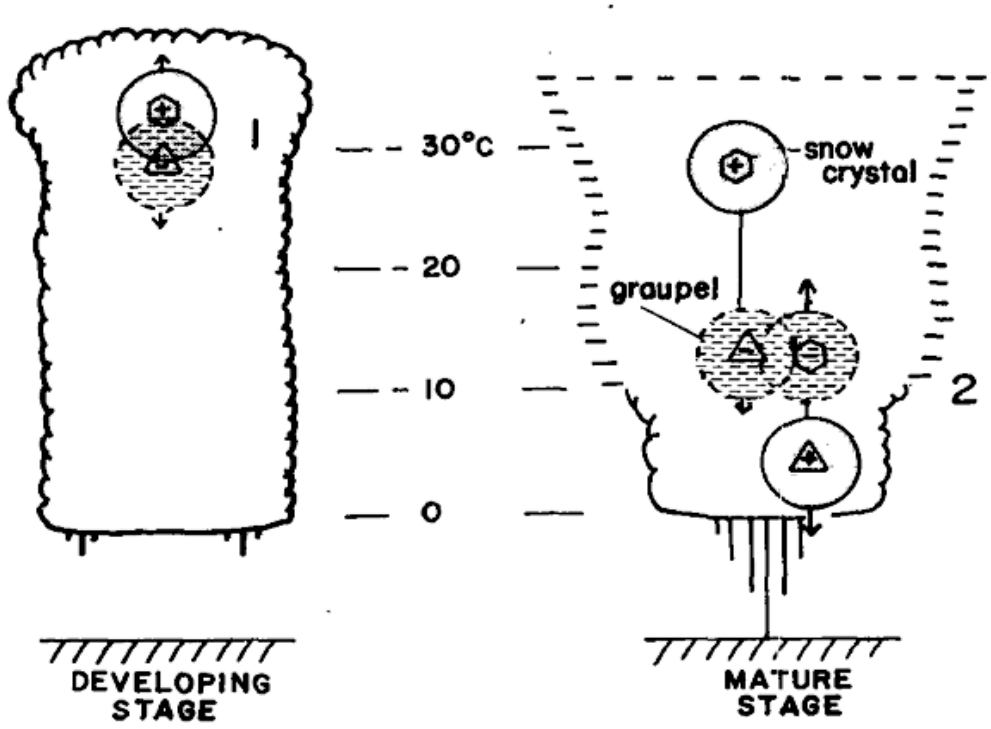

Fig. 4. A schematic model showing the two major stages of charge accumulation in thunderstorms. The developing stage shows graupel (triangle) charging negatively and snow crystals (hexagons) charging positively. The heavier graupel particles descend and as they fall below the -10° C level they are electrified positively (snow crystals negative) due to riming electrification. This results in a tripole structure of charge. (from Takahashi 1984).

Avila et al. (2005) show that the charging on graupel reverses from negative to positive where larger crystals and aggregates are present in the cloud. They suggest that graupel pellets growing by riming charge positively in regions where irregular large crystals or aggregates prevail in thunderstorms. Therefore, since large aggregates are uncommon at heights above the -20° C isotherm (Hobbs et al. 1974), this process may help explain the development of the lower positive charge region as updrafts weaken and mixed phase hydrometeors descend.

An in-situ study performed by Dye et al. (1988) examined two small thunderstorms in which aircraft equipped to measure the electric field, liquid water content, and particles larger than about 50 μm made several passed through the storms at the -12° C and -20° C level. Passes through the -12° C level revealed the presence of supercooled water and ice particles existing in a net negative charge region whereas a net positive charge was found at the -20° C level. Both charge regions contained relative maxima in ice particle concentration and size with high correlations found between ice particle collision rates to regions of charge. The findings are also suggestive of the charge transfer occurring from the ice particles in the presence of supercooled water, which is consistent with the non-inductive charge hypothesis.

Comprehension of the non-inductive charging mechanism is still empirically based, with uncertainty present in the exact microphysics driving the process. However, the current understanding of this mechanism provides a reasonably good representation of the gross charge structure observed in thunderstorms. Moreover, the laboratory studies agree with the results from several field studies showing correlations between the onset of electrical development and the occurrence of riming precipitation within the storm

(e.g. Goodman et al. 1988; Carey and Rutledge 1996; Carey and Rutledge 2000). The charge reversal temperature may also help explain the increase in CG during weakening stages of thunderstorms, as ice crystals start to descend leading to the development of a lower positive charge layer as discussed below.

1.4 Thunderstorm Charge Structure

Past studies suggest that the gross charge structure of a thunderstorm resembles a dipole or tripole structure of charge as depicted in Fig. 5 with the main positive charge region located above the main negative chare region (i.e. a positive dipole structure), which is typically located around the -10° C to -20° C isotherm (e.g., Williams 1989b; MacGorman and Rust 1998). The lower positive region shown in Fig. 5 may not be present throughout the lifespan of the storm, but past research suggests the development of the lower positive charge region is essential in the development of cloud to ground lightning (e.g. Williams 1989a). The processes that control the development of the lower positive charge region are not completely understood, but current theories point to drop breaking, lightning charge deposition, positive corona discharge, ice crystal size, positive charge associated with melting, and the aforementioned temperature dependence on graupel charging in non-inductive charging (Williams 1989b; Avila et al. 2005).

Of the various theories, the most widely accepted theory for the lower positive charge layer is the aforementioned temperature dependence of the NIC mechanism (Krehbiel 1986; Williams 1989b). Explaining the lower positive region with the drop break or the melting theory is difficult because most of the precipitation in this layer is

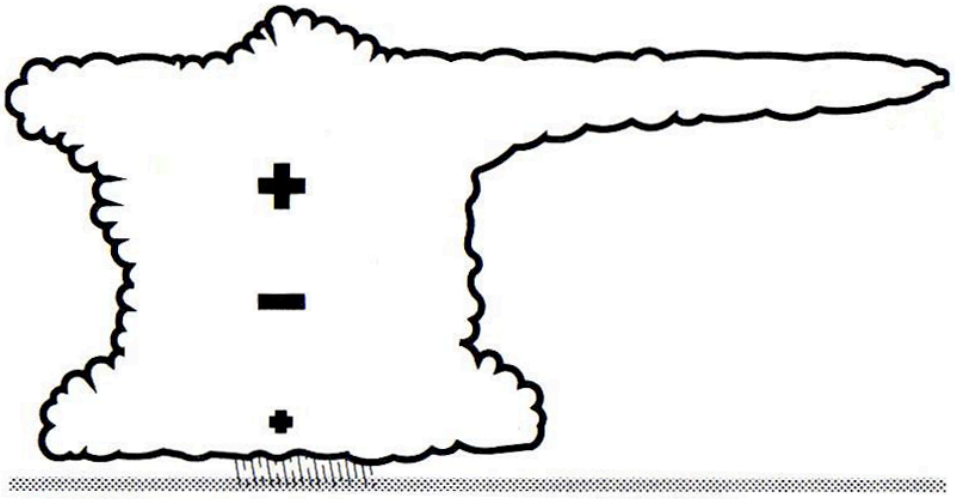

Fig. 5. Tripole structure of a thunderstorm with upper and lower positive (+) charge regions and main negative (-) charge region (from MacGorman and Rust 1998).

composed of ice rather than liquid water (Williams 1989b). In addition, the charge produced by drop breakage is too low to account for the large amount of charge found in this region. The lack of sufficient charge generation for this region is also observed for the positive corona discharge theory. The idea that the lower positive charge region is produced from lightning discharging positive charge on precipitation may not be widely accepted, but it is not completely ruled out. The problems with this theory are that cloud particles are more likely to intercept field-driven ions than precipitation particles and that the lower positive charge region has been observed in electrified clouds before the first lightning flash occurs (Williams 1989b).

Despite the questions associated with the development of a lower positive charge region, it is understood that more complex vertical charge structures can exist within convection, with more than 5 layers of charge possible (Stolzenburg et al. 1998) (Fig. 6). Some of these additional charge structures can be attributed to screening layers that develop as a result of discontinuities in conductivity at the boundary of clouds (MacGorman and Rust 1998). Typically, the layers of charge within the updraft that are associated with screening layers are very thin and the charge gradients due to screening layers are likely to small to generate lightning. Thus, unlike the main charge regions, the locations of screening layers are difficult to assess with VHF lightning observations. Therefore, our emphasis will focus on the development of the gross charge structure of the convectional tripole model.

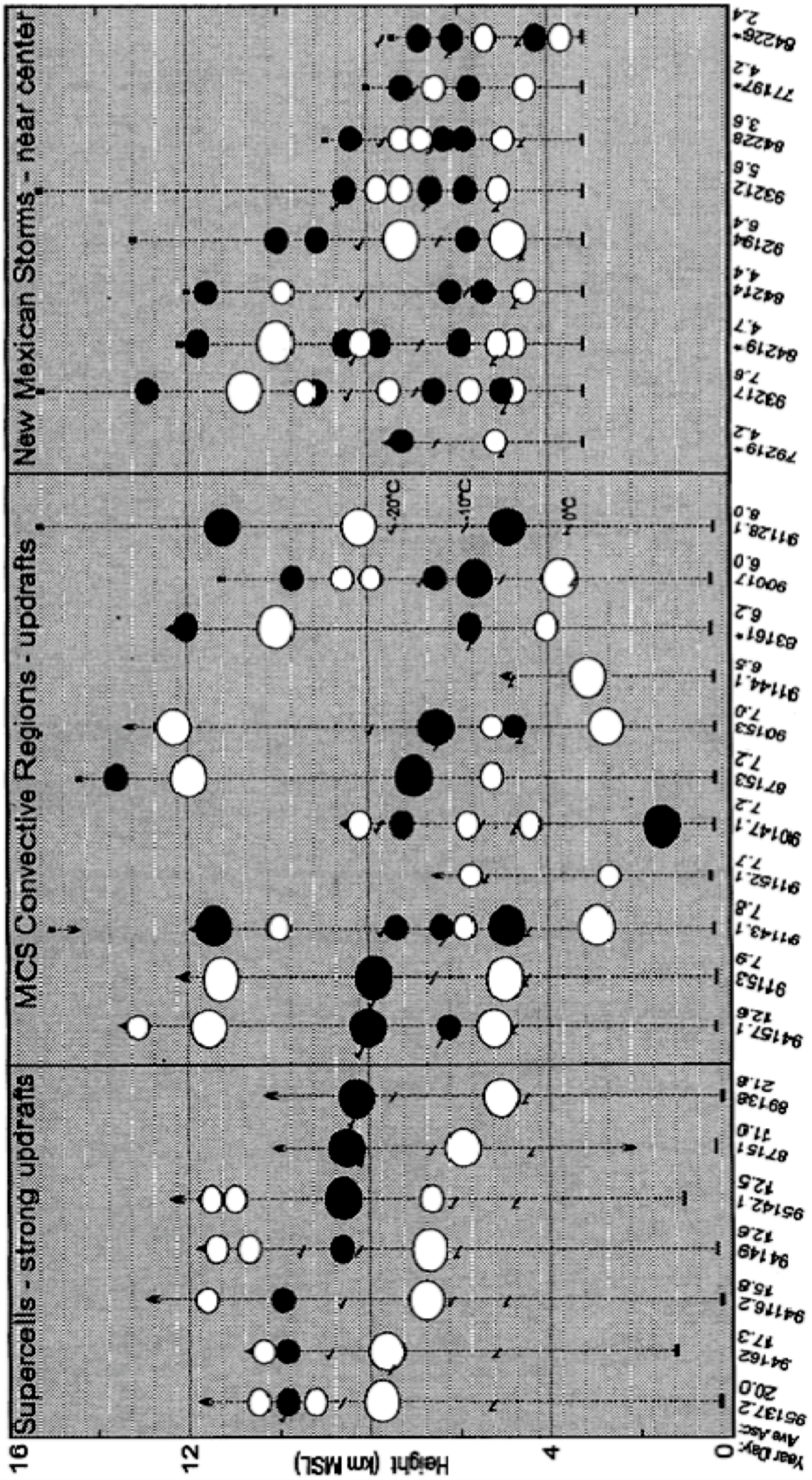

Fig. 6. Charge distributions from electric field (E) soundings showing multiple charge regions within the convective updrafts of three types of thunderstorms. Vertical dashed lines represent an electric field sounding (labeled with year and Julian day –yyddd- along horizontal axis). Values to the right of the date information show balloon ascent rate between surface and 12 km in ms^{-1} (or top of sounding, if below 12 km). Negative (positive) charge layers are represented by solid (open) ellipses, with larger ellipses for layers deeper than 1 km. Surface heights are indicated by horizontal bars. Short slanted lines indicate heights of 0°, -10°, and -20°C in each sounding. (From Stolzenburg et al. 1998).

1.4.1 Lightning Development and Propagation

Lightning is categorized into two main types: cloud-to-ground (CG) and in-cloud (IC) lightning. CG flashes effectively transport cloud charge to the ground with the four types of CG in Fig. 7 showing (a) downward negative lightning, (b) upward negative lightning, (c) downward positive lightning, and (d) upward positive lightning. Research from Orville and Huffines (2001) suggests that most (~90%) of CG flashes from ordinary thunderstorms are downward negative flashes, type (a) in Fig 7, which serve to lower negative charge to the ground. Positive CG lighting in ordinary thunderstorms, although rare, serves to lower positive charge to the ground (type (c) and Fig. 7). Types (b) and (d) are thought to occur only from tall objects (~100 m or greater) (Rakov and Uman 2003, p. 4).

Currently, the processes responsible for lightning initiation remain unclear. Although, Crabb and Latham (1974) show production of point discharge occurring by colliding raindrops in electric fields typical of thunderstorms, uncertainty still exists as to whether this is the driving force behind lightning initiation. Marshal et al. (1995) suggested that lightning may be initiated as energetic electrons are accelerated by thunderstorm electric fields to velocities sufficient to produce new energetic electrons during ionizing collisions with nitrogen or oxygen molecules (i.e. runaway electrons). Marshal et al. claim that this electric filed may be substantially less than the electric fields assumed for dielectric breakdown. They came to this conclusion by comparing the vertical profile of the electric field to the breakeven threshold field and found that lightning typically occurred within a few seconds after the electrical field surpassed the

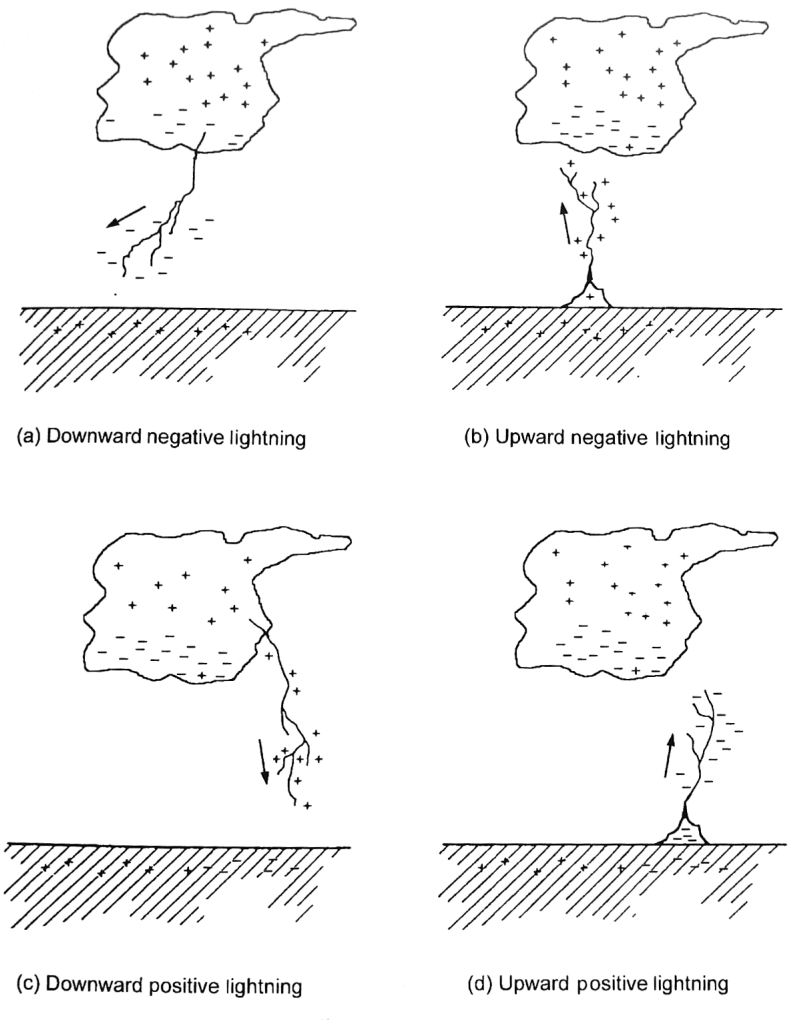

Fig. 7. Four types of lightning effectively transferring cloud charge to ground. Only the initial leader is shown for each of the four types with the direction of leader propagation and polarity of cloud charge effectively lowered to the ground shown (From Rakov and Uman 2003).

breakeven filed. Similar results documented by Marshal et al. (2005) suggesting that runaway electrons may be responsible for the initiation of lightning.

Aside from the uncertainties in lightning initiation, the processes driving the onset of a lightning flash are a result of sufficient build up of opposing charges that ultimately lead to the breakdown or breakeven process. The first lightning flashes within a thunderstorm are typically IC flashes, which connect between two charge regions of opposite sign (Krehbiel 1986). Generally, IC lightning dominates over CG lightning in ordinary thunderstorms (Krehbiel 1986), though the variability in the IC to CG ratio seems to be at least partially related to the intensity of the convection (Chéze and Sauvageot 1997). Assuming a positive dipole structure, intracloud flashes tend to originate between the upper positive and main negative charge regions and tend to move negative charge upward or positive charge downward (Shao and Krehbiel 1996; Rakov and Uman 2003). Since precipitation particles, especially positively charged ice crystals, should be lofted higher as the updraft intensifies (Saunders 1993), the locations of the charge regions, and thus IC flash heights, should increase. Steiger et al. (2005) examined this possibility within a supercell thunderstorm to show strong positive correlations exist between storm intensity (radar top, VIL, SHI) and lightning heights.

CG lightning flashes are composed of many processes with the following discussion of those processes adapted from Uman (1987) and illustrated in Fig. 8. The process begins when a charge separation produces a potential difference between charge regions, which exceeds the electrical breakdown field strength. If this field strength is reached, a preliminary breakdown occurs which initiates a highly branched “stepped leader” of negative charge from the main negative charge layer of the cloud. The stepped

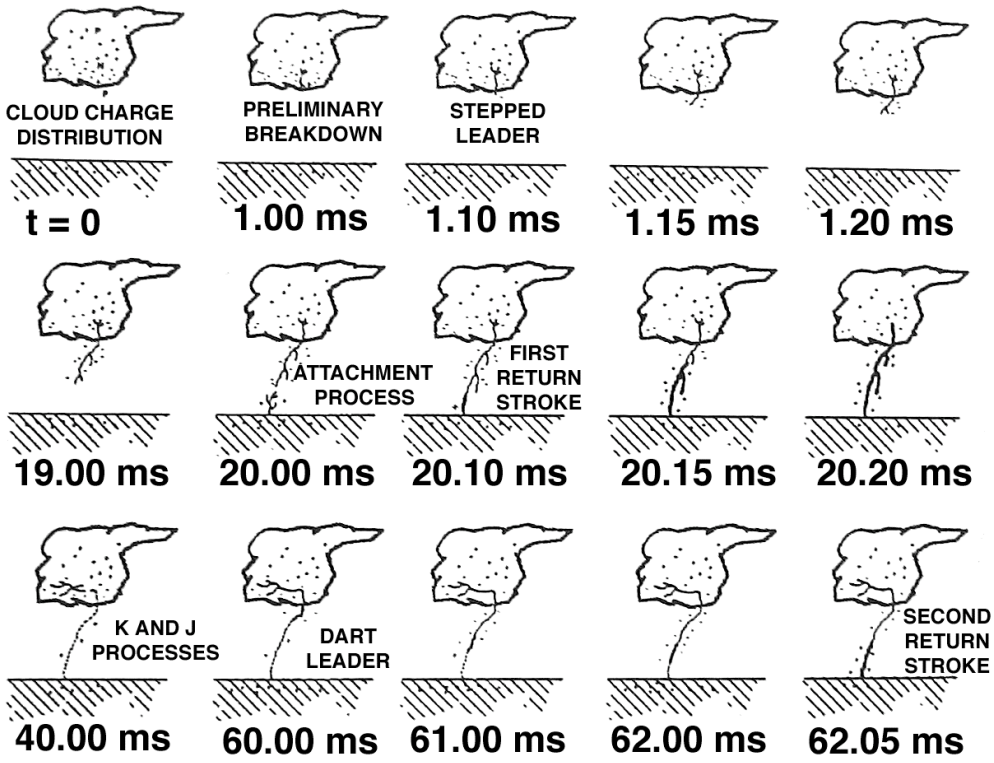

Fig. 8. Illustration showing the cloud-to-ground lightning flash process (from Uman 1987).

leader advances in a series of discrete steps towards the ground, each of which has lengths in the 10's of meters and occurs in 20-100 μs intervals. As the stepped leader propagates toward the ground, it branches out in a downward fashion while seeking the path of least resistance toward the ground. Once the leader is within approximately 50 m of the ground, the electric field at the surface will become large enough to cause the air to fail as an insulator and will ultimately result in electrical breakdown. This results in one or more upward moving discharges of opposite polarity to seek a connection to the downward moving stepped leader. When the connection is made, the stepped leader becomes electrically grounded causing the leader channel to rapidly discharge and marking the first "return stroke." The peak currents from the return strokes typically average around 30 kA, with the flash acting to lower the charge present in both the leader channel and the at the top of the channel. If additional charge becomes available at the top of the lightning channel, subsequent return strokes within the same lightning channel may occur. "Dart" leaders initiate the subsequent strokes that follow previously formed channels. Once charge becomes available, a dart leader is initiated, which deposits charge along its rapid descent down the former return stroke channel with a typical velocity of $3x10^6$ ms^{-1}. The new return stroke is initiated upon the arrival of the dart leader to the ground, which can continue in succession until charge at the top of the lightning channel becomes unavailable (Fig. 8).

1.5 Hypothesis and Related Questions

Based on the results of past studies, we hypothesize that the evolution of lightning activity is attributed to microphysical and kinematic processes within convective storms.

This study will examine a statistically significant quantity of ordinary thunderstorms, which are the most ubiquitous and fundamental of all thunderstorm types. This will allow for a fundamental approach to address several ongoing questions within the lightning community such as whether total lightning characteristics within ordinary thunderstorms tend to follow the conventional model proposed by Williams et al. (1989a). This includes general observational questions such as: Does IC lightning tend to dominate in the early stages of thunderstorm development? Do peaks in CG lightning flash rates lag peaks in IC lightning flash rates? Does CG lightning tend to follow the descent of the main precipitation core as evident from radar reflectivity? Following in the lines of past research examining flash characteristics of more complex modes of convection (e.g. Ray et al. 1987; Coleman et al. 2003; Lang et al. 2004a,b; Carey et al. 2005; Wiens et al. 2005; Steiger et al. 2005) we will test whether significant correlations exist between lightning flash characteristics and radar inferred convective intensity. This includes questions regarding the correlation between lightning flash rates and total ice mass as well as several other radar intensity parameters. We will also examine the evolution of lightning flash heights to test whether fluctuations in flash heights are correlated to storm intensity or if changes in lightning heights are related to lightning type (i.e. IC vs. CG). From an applied perspective, we will address the implications of this study toward improvements of short-term operational lightning forecasts. This includes addressing questions such as: are lightning flash heights correlated to storm intensity? Can one infer lightning flash characteristics based on radar inferred microphysical and/or kinematic information? Does a correlation exist between the location of the VHF inferred positive charge regions and the onset of IC or CG lightning? Within these questions we hope to

show potential benefits that total lightning data provide over CG lightning data alone.

2. DATA AND METHODOLOGY

2.1 Lightning Detection and Ranging Network

Time and location data of VHF radiation sources were obtained from two three-dimensional (3-D) lightning mapping networks: 1) Vaisala's Dallas-Fort Worth Lightning Detection and Ranging (LDAR) network located in Dallas-Fort Worth, Texas (Fig. 9), and 2) The Texas A&M University LDAR (TAMU LDAR) located in Houston Texas (Fig. 10). The Dallas LDAR network is comprised of 7 VHF sensors with 20-30 km baselines centered on the Dallas-Fort Worth International Airport and a center frequency of 63 MHz (e.g. Carey et al. 2005). For this study, the Houston network was comprised of 10 sensors with an average baseline of 25 kilometers centered slightly northeast of downtown Houston at 29.79º N and 95.31º W. Two additional VHF sensors will be installed and incorporated into the Houston network during summer 2006. The sensors have a 5 MHz bandwidth with a center frequency that varies between 69.0 and 71.0 MHz (Ely et al. 2006). Since different sites may have higher background noise at a particular frequency, variations in the center frequency allow for reductions in the effects of the RF noise conditions.

Each sensor within a network monitors the VHF radiation produced by both intracloud (IC) flashes and portions of cloud-to-ground (CG) flashes produced during the breakdown process (McGorman and Rust, 1998). If a sensor receives a pulse of VHF radiation that surpasses a specified threshold, then the time of the strongest VHF pulse is recorded and compared with the times that the other sensors within the network recorded a pulse. Accurate distance calculations require precise time synchronization between

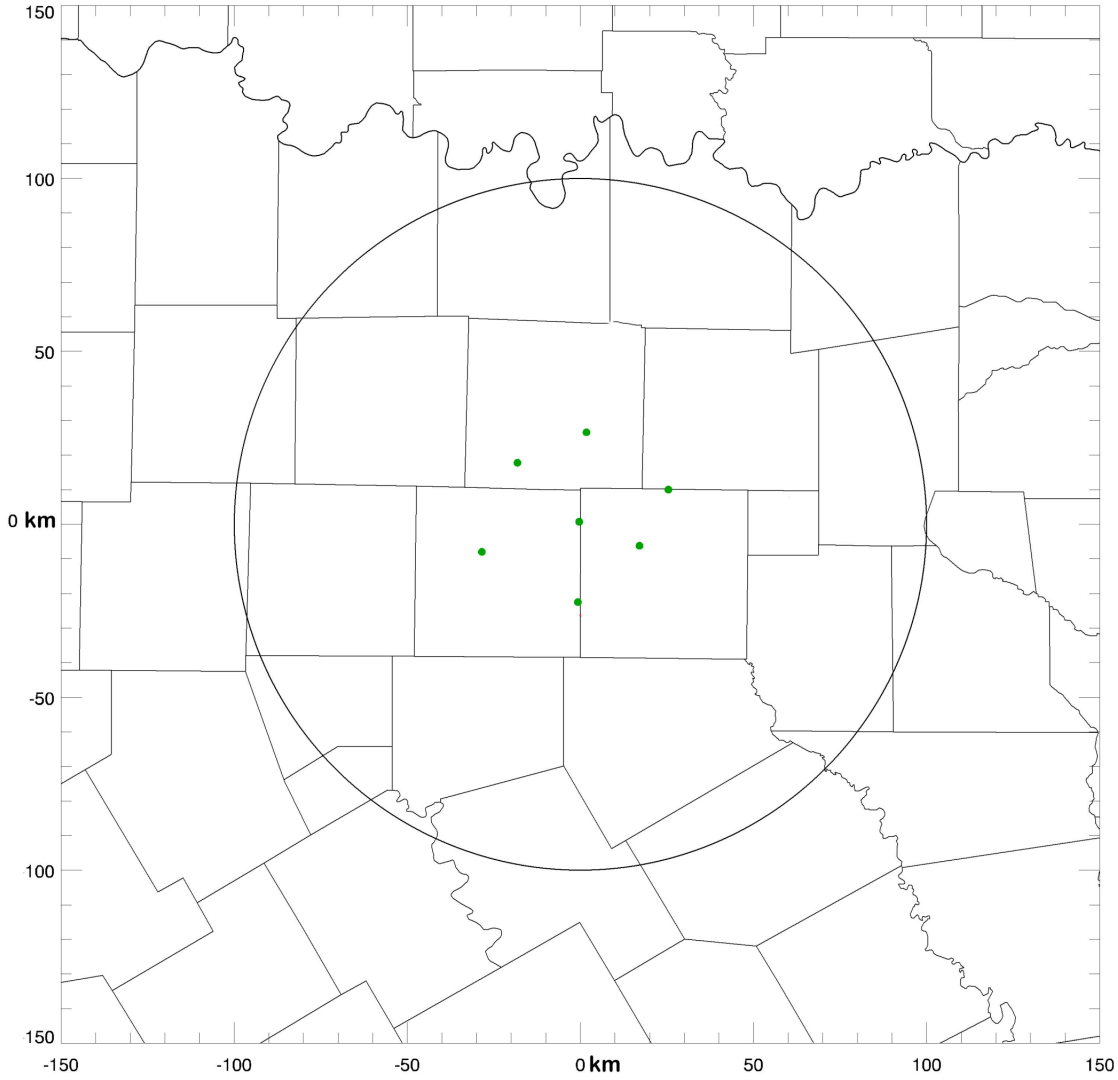

Fig. 9. Map depicting the locations of the seven Dallas LDAR sensors (green circles). Large black ring surrounding the network depicts a 100 km range from the center of the network.

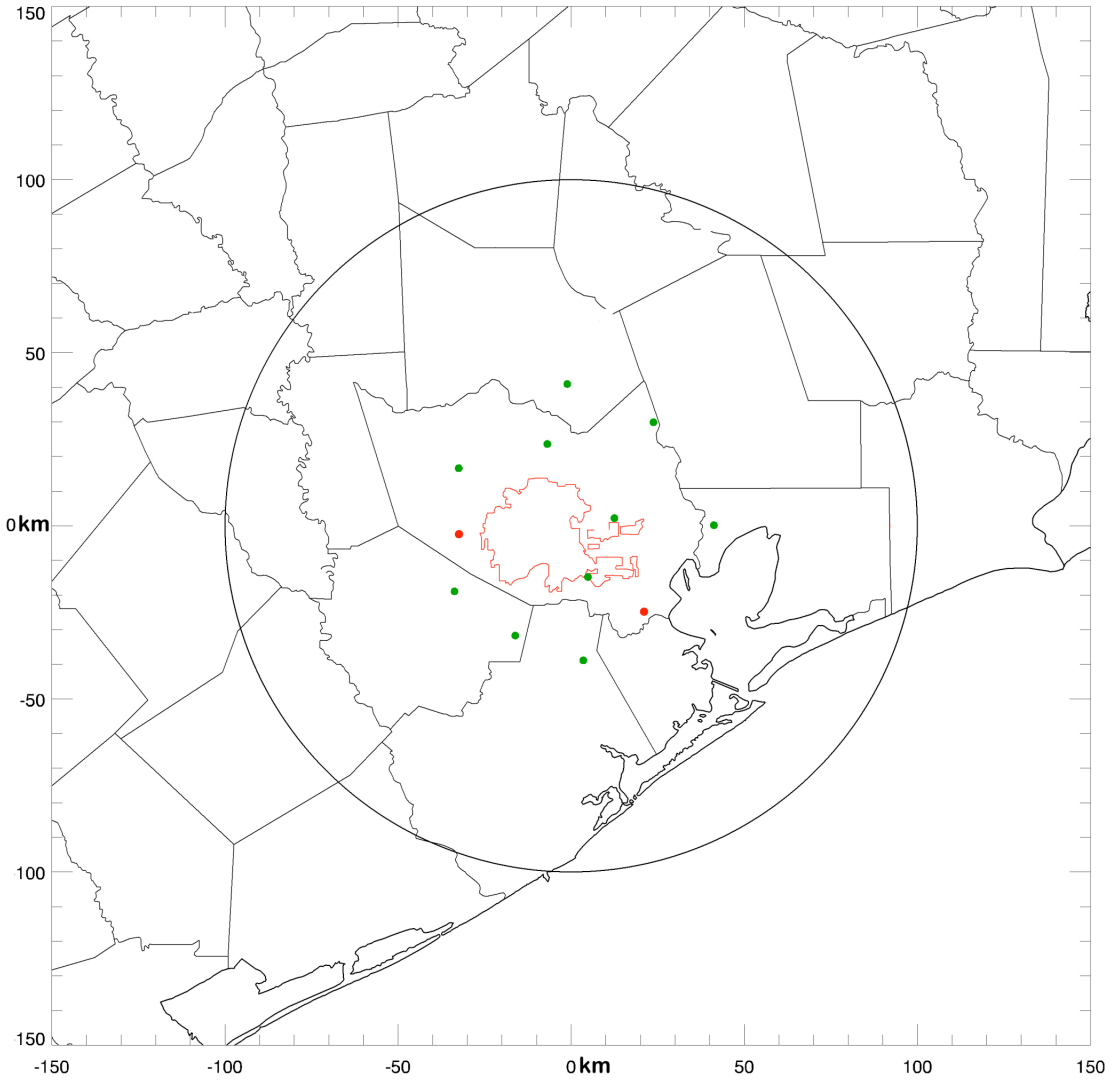

Fig. 10. Map depicting the locations of the twelve Houston LDAR sensors (colored circles). The green circles represent sensors that were in operation during the time of this study, while the red circled are sensors that were inoperable and/or partially installed. The large black ring surrounding the network depicts a 100 km range from the center of the network. The red outline shows the Houston Urban area and industrial suburbs.

sensors, which has been accomplished by incorporating Global Positioning Satellite (GPS) technology into each sensor. This technology allows synchronization of the clocks within each sensor such that the peak VHF signal times and amplitudes are recorded within 100 μs time intervals (Rison et. al, 1999; Carey et al. 2005; Ely et al. 2006). The times at which the VHF signals arrive at each sensor are either transmitted in real-time (at time resolutions of 200 μs) to a central workstation via internet connections or uploaded onto the work station (at time resolutions of 100 μs) via removable hard drives after the thunderstorm event. Due to the lower temporal resolution of real-time data, which is necessitated by the limited data transfer rates of the LDAR sensors, it is not typically incorporated into research analysis. The work station computer then uses a time-of-arrival technique to calculate the location of each VHF source using the arrival times of the radiation from at least 5 sensors (Ely et. al, 2006).

The time of arrival technique operates on the fact that a VHF source will reach each sensor at a specific time based on its distance from a given sensor, assuming some signal propagation speed. The following discussion is an adaptation of TOA systems by MacGorman and Rust (1998, p.161). For a given VHF source, the difference in the times at which the signal arrives at a pair of stations defines a locus of constant time difference, which forms a hyperbola that passes through the VHF source location. A third station provides a second hyperbola of constant time differences that intersects the first hyperbola at the point the VHF source occurred (Fig. 11). Depending on the source's location relative to the position of the sensors, it is possible to have two intersections of the hyperboles, therefore a fourth station is required to eliminate this possibility (Fig. 11). Both networks require that a minimum of 5 stations record the arrival time of a specific

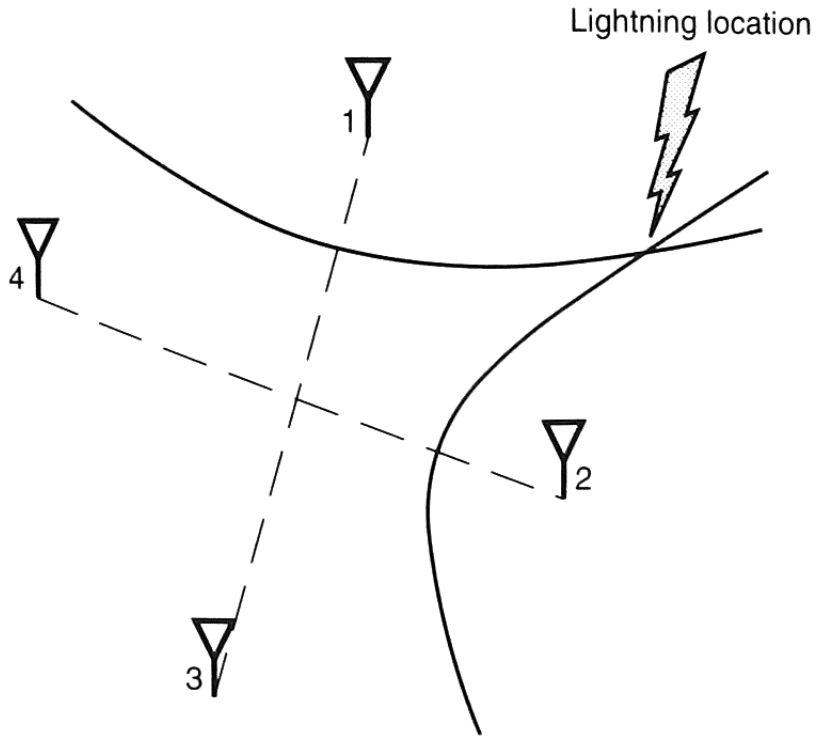

Fig. 11. Time-of-arrival system showing location of ground strike. The hyperbola on which a lightning flash is located is defined by the time at which the signal arrives at two or more stations. The intersection of hyperbolas from two different stations define the location of the strike (from MacGorman and Rust, 1998).

VHF source before a solution on the source's location can be made. Incorporating location data from five stations to solve for an equation with 4 unknowns (x, y, z, and t) allows for a redundant solution, which serves to improve the accuracy of the final solution. Additional sites observing the same VHF source can enhance this accuracy by adding additional redundancy to the solution.

Restricting valid solutions to 5 sensors does not minimize all errors, however, and the location accuracy of VHF sources decreases as the range between the source, and the center of the LDAR network increases. Therefore, effort was taken to ensure that the errors associated with range effects would not be a significant source of error in our final results. Results from Thomas et al. (2001) suggest that the source powers radiated by negative polarity breakdown radiate isotropically between 30 W and 1 kW in the 60-66 MHz band. By performing a source power distribution, Thomas et al. found a -0.1 dB per kilometer slope for powers above 100 W. Since the lower end of the power distribution is lost as distance from the center of the network increases, the source power distribution can provide a rough estimate of the relative detection efficiency of the network. Carey et al. (2005) incorporated this idea to examine the detection efficiency of the Dallas LDAR network to find that the source detection efficiency for a case occurring on 16 June 2001 was approximately 10% of its maximum value at a range of 50 km. The source detection efficiency was reduced to approximately 4% of its maximum value at a range of 100 km with the expected flash detection efficiency of 90% out to a range of 100 km. The expected 3-dimensional location accuracy for individual radiation sources is between 100 and 200m within the network interior (range approximately 30 km from center) and better than 2 km out to a range of 150 km (Demetriades et al. 2001; Carey et al. 2005).

Similar results were noted for the Houston LDAR network as an intense squall line passed through the network, which extended well beyond the network's anticipated 100 km range as shown in Fig. 12. As described by Ely et al. (2006) the convective line served as an effective means to test the network's detectable range of sources since the line passed over the network with a constant radar inferred convective intensity. Therefore, the assumption could be made that the electrical activity was similar along the entire line. Observations of the sources associated with the main convective line show a dramatic drop off in the number of sources beyond 135 km (Fig. 13), which did not appear to be associated with a change in convective intensity. Given that the flash detection efficacy tends to drop off rather dramatically beyond 100 km for both LDAR locations, limitations were made such that only convective cells that fell within 100 km from the center of each network were used for this study.

Although VHF source densities can provide a great deal of information on the gross charge structure of convective cells, many past studies have focused on correlations between various thunderstorm characteristics and flash counts, rather than source counts, as the measure of lightning activity. Lightning flash rate has been hypothesized to be directly proportional to the thunderstorm electrical generator power (Vonnegut 1963; Boccippio 2002), whereas VHF source rate has no such apparent relationship with electrical power. Moreover, the decrease in flash detection efficiency is less abrupt than the decrease in source detection efficiency as range increases from the network. In order to obtain information regarding the flash characteristics of each case, we employed a modified version of a NASA flash algorithm, which groups individual VHF sources into flashes based on spatial and temporal constraints. The constraints are based on

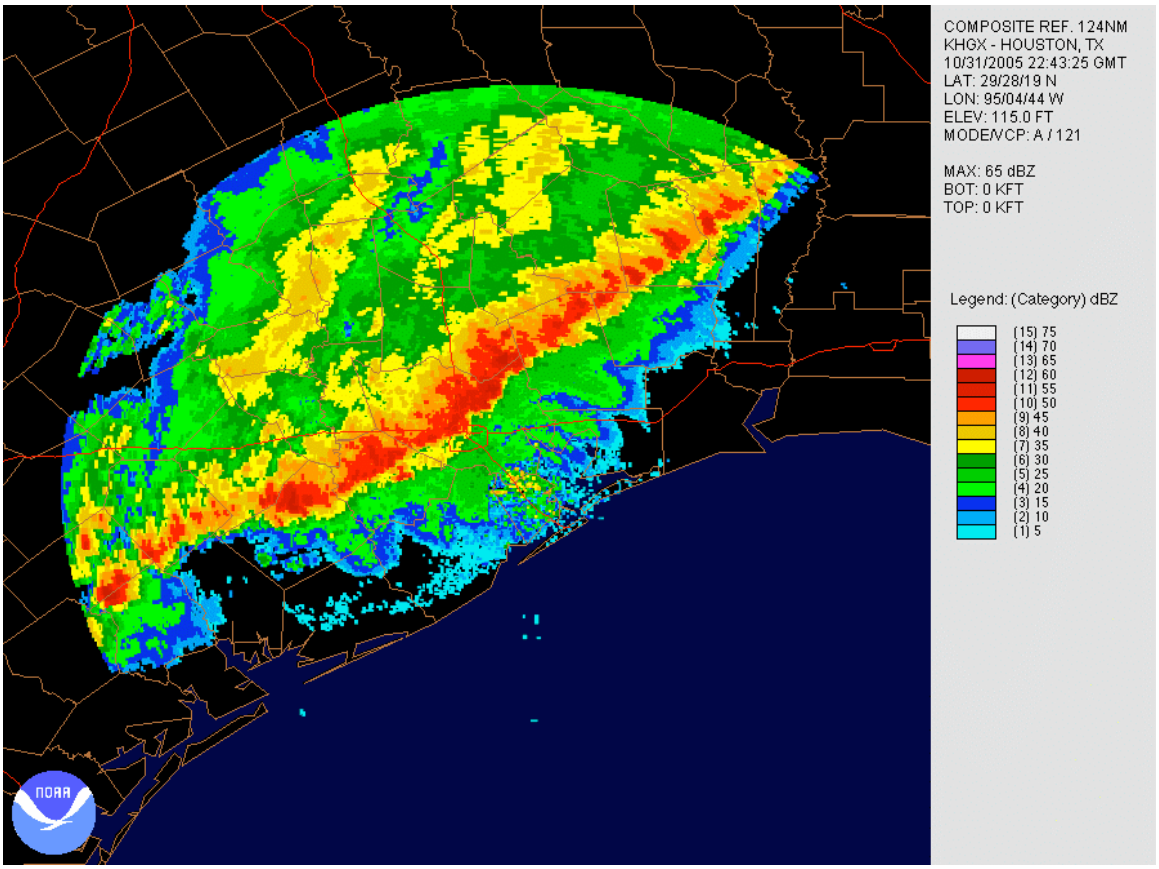

Fig. 12. Composite reflectivity scan from the WSR-88D KHGX radar on October 31, 2005 at 22:43 UTC *(Source: NOAA NCDC)*.

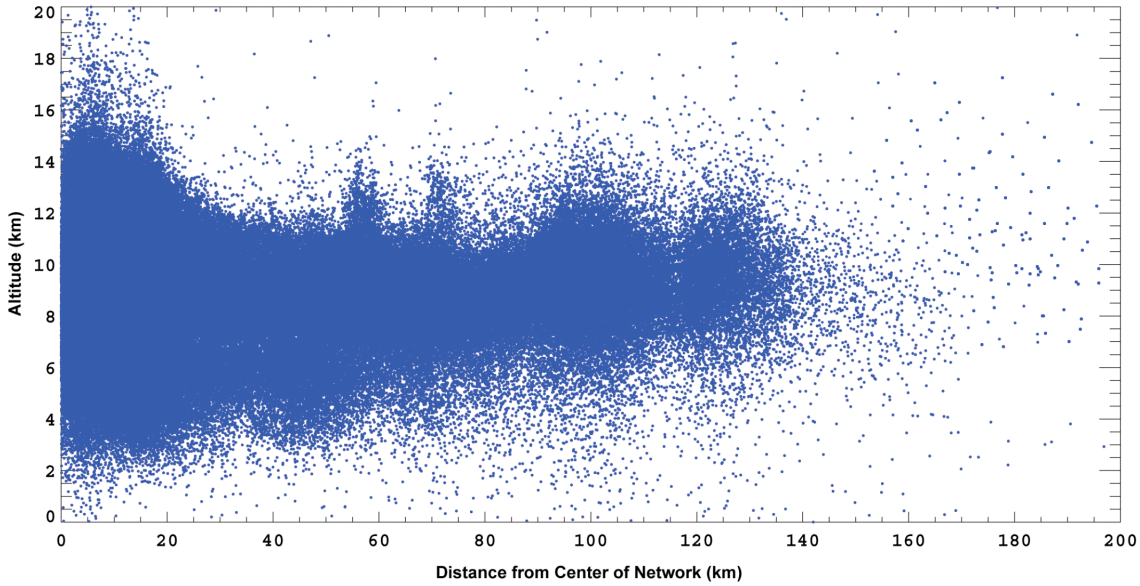

Fig. 13. Altitude (km) versus radial distance from center of the Houston LDAR network of VHF sources detected in a 1 km thick slice for the time period of 19Z on 10/31/05 to 03Z on 11/01/05. Slice oriented parallel to the convective line from the center of the network as shown in fig 2.8. Notice the dramatic drop off of sources at approximately 135 km. *Source: Ely et al. (2006)*

measurements of typical flash length and propagation speed (MacGorman and Rust 1998, Ch. 5). The algorithm, which is based on the flash algorithm used for NASA's Kennedy Space Center LDAR and recently translated to Interactive Data Language (IDL) by Lee Nelson (personal communication, 2006), determines if a source was a part of a flash based on the following criteria: the maximum duration of a flash cannot exceed 3 seconds, the analyzed source is within 5 km of a source already associated with the flash, the time lag between the analyzed source and sources in the analyzed flash within 5 km is not greater than 0.5 seconds, and the maximum time delay between points in a branch cannot exceed 0.03 seconds. A source initiates a new branch when the analyzed source is greater than 0.03 seconds from the last source observed or the source is greater than 5 km from the last source observed, but still within 5 km of another source in the flash. In this case a new branch occurs to the closest source that occurred within 0.5 seconds of the analyzed source and is within 5 km of the analyzed source. If either of these conditions fail, then a new flash, rather than a new branch, is created.

In addition to the temporal and spatial constraints, a valid flash was required to consist of at least 3 sources. According to Thomas et al. (2003), some flashes may only register as a single VHF source by the LDAR system. However, most of these are typically poorly located events that belong to a larger flash and are usually found close in both space and time to the larger flash. Moreover, with an observed average of 34.4 sources per flash for all cases combined in this study, it seemed reasonable to assume that most flashes consisting of less than 3 sources were either a part of a larger flash or background noise. This assumption, however, may not be valid for distances beyond 100 km, as the number of sources per flash decreases nearly linearly as distance from the

network center increases (Fig. 14). This idea was tested for a cell located 111 km from the center of the network, which, when run through the flash algorithm, resulted in 29% of detected flashes occurring with less than 3 sources. Therefore, in an effort to follow the convention of past studies (e.g. McCormick et al. 2003, Carey et al. 2005), in addition to observations of our own cases, we accepted the criteria that 3 sources are required for a flash to be considered valid.

Tests of the accuracy and robustness of the flash algorithm were made by making minor adjustments to each constraint. We conducted various sensitivity tests in a manner similar to McCormick (2003) and Steiger (2005). Eight adjustments to the aforementioned default constraints (3s, 5.0 km, 0.5 s, 0.03 s) were made for three cells, which were chosen as representative cases based on their average flash rates of 2 flashes per minute and maximum flash rates not exceeding 8 flashes per minute. Since the number of sources per flash decreases with increasing range from the LDAR network (Fig. 14), two Houston cases, which occurred at spatial extremes from the network (97 km and 8 km), were chosen. In Dallas-Fort Worth, the cell examined fell at a distance of 59 km from the center of the network. The eight adjustments to the aforementioned default constraints (3s, 5.0 km, 0.5 s, 0.03 s) are listed below:

1) 3 s, 3.0 km, 0.50 s, 0.03 s
2) 3 s, 7.0 km, 0.50 s, 0.03 s
3) 3 s, 5.0 km, 0.15 s, 0.03 s
4) 3 s, 5.0 km, 0.85 s, 0.03 s
5) 2 s, 5.0 km, 0.50 s, 0.03 s
6) 4 s, 5.0 km, 0.50 s, 0.03 s
7) 3 s, 5.0 km, 0.50 s, 0.01 s
8) 3 s, 5.0 km, 0.50 s, 0.05 s

Increasing (decreasing) spatial and time constraints should lead to lower (higher) flash counts since more (less) sources would be assigned to a particular flash. With more

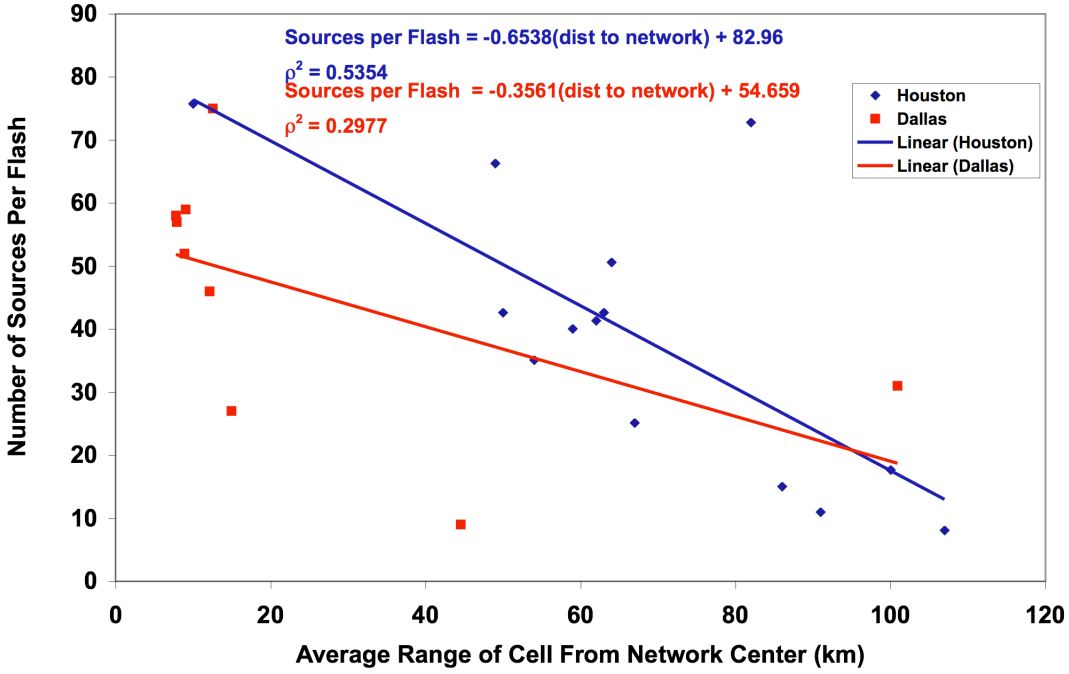

Fig. 14. Scatter plot (Red points = Dallas; Blue points = Houston) showing correlations between the number of sources per flash and the distance of a cell from the center of the network for Houston and Dallas network.

sources assigned to a flash, it becomes less likely that one flash will be broken up into multiple flashes and it also becomes more likely that multiple flashes could be combined as one. However, the total flash counts for each cell did not experience any changes except for adjustment (3) in which the time lag between source points within 5 km was reduced to 0.15s. This increased the flash count by only one flash for both the Dallas case and the 8 km Houston case. This does not seem unreasonable, however, since the flash rates with the cells examined are fairly low (average maximum flash rate of 7 flashes min^{-1}), thus limiting the potential for multiple flashes to be grouped together, or single flashes to be broken apart. In higher flash rate storms, adjustments to the flash algorithm result in significant changes to the total flash rates (e.g. Steiger 2005 and McCormick 2003). However, the flash algorithm seems extremely robust for low flash rate storms as examined in this study.

2.1.1 VHF Flash Data

Once VHF sources are grouped into flashes, it becomes possible to test the results of past studies reviewed earlier in section 1.1.2.1, which have focused on flashes rather than individual VHF sources. Therefore, with VHF sources grouped into individual flashes, in combination with NLDN data, it was possible to determine IC and CG 3-D flash locations, IC and CG flash rates, as well as differentiate IC from CG flashes.

This information was obtained by feeding the data output by the flash algorithm, through various IDL programs. The flash algorithm outputs data for each source in the American Standard Code for Information Interchange (ASCII) format. Each source point

has information regarding the time (day, month, year, hour, minute, second, microsecond), location (latitude, longitude, height), and location within the flash it is assigned to (flash number, position in flash, position in branch). For our study, the programs extracted information regarding the 3-D origin location of each flash, average height of the VHF sources that make up each flash (hereafter referred to as "flash height"), and the total flash rate. Since the microphysical and kinematic properties of each cell were obtained by radar, which records cell information in approximately five-minute intervals, we also grouped flash information into five-minute intervals such that the temporal scales would reflect both data sets. During each interval, the IDL program produced statistics on the 95^{th} percentile, 75^{th} percentile, mean, and median flash heights, as well as five-minute running averages of the total, IC, and CG flash rates.

IC flash rates were calculated by subtracting the number of National Lightning Detection Network (NLDN) detected (see Sec 2.2) CG flashes during a given one minute time span from the number of LDAR detected total flashes during that same one minute time span. In rare cases in which the CG flash rates were higher than the total flash rates, the IC flash rate was given a value of zero.

In addition to the programs responsible for outputting flash statistics, a program was created to produce time height cross sections of VHF source density (VHF sources min^{-1} km^{-3}) overlaid on radar reflectivity data. VHF sources were placed into vertically distributed 1 km bins with horizontal radii based on the distance from the cell center to the furthest 20 dBZ contour. Since the 20 dBZ contour of some cells displayed an elliptical rather than perfectly circular signature, the volume of some bins may include regions of radar reflectivity values below 20 dBZ. This would present a serious problem

if direct comparisons between the magnitude of VHF source densities were compared between cells. However, since we were only concerned with the location of the maxima in VHF source densities, rather than the actual magnitude, these errors did not affect our final conclusions.

Once the data for a time period were collected, calculations were made to determine the VHF source density and the flash origin density for each bin. The origin of each flash, as determined by the flash algorithm, and the time of each CG were both plotted on the graph to examine trends between CG and IC flashes. Isotherms were also overlaid on the plot to examine the results of previous studies, which have shown that the main negative charge region typically resides around the -10º C isotherm (Krehbiel 1986). When combined with radar data, the information provided on the graphs provides a graphical representation of the electrical and kinematic evolution of each convective cell (e.g., see Fig. 20).

2.2 National Lightning Detection Network

The two-dimensional National Lightning Detection Network (NLDN) data provide the latitude, longitude, time, polarity, and stroke multiplicity of detected cloud-to-ground (CG) flashes. These data were obtained from Vaisala, Inc., in Tucson, AZ, which has established a network consisting of 106 sensors nationwide as of 2001 (Orville and Huffines 1999). In 2002, the NLDN network underwent an upgrade to enhance the sensitivity and accuracy of the sensors. This upgrade increased the detection of lower amplitude sources, which leads to an increased possibility of identifying IC flashes as CG flashes. Although Cummins et al. (2006) points out that additional work is required to

understand the extent of these errors, past research indicates that CG flashes with peak currents < 10 kA are typically CG flashes in the geographical location of this study (Texas). The upgrade was performed by incorporating both Time of Arrival (TOA) location information with a magnetic direction finder system (MDF) as well as the installation of additional sensors (Cummins et al. 2006).

The MDF uses two vertically looped antennas mounted perpendicular to each other to measure the magnetic field produced from vertical lightning channels. For a given lightning current, the signal on each loop is maximized when the loop points in the direction of the lightning channel. A direction finder system can then calculate a ratio of the signal measured on each loop to obtain a bearing of the lightning channel. The distance of the flash from the sensors is obtained using TOA techniques. With both the TOA and MDF data, and using a least squares technique, the optimal location of the flash can be determined (Cummins et al. 1998; MacGorman and Rust 1998). The median accuracy of the ground flash locations is less than 500 m and the expected flash detection efficiency between 90-95% (Cummins et al. 1998; Cummins et al. 2006). The time resolution of the data is 0.1 seconds.

For our analysis, the NLDN data were post-processed by Vaisala Inc. such that individually recorded strokes were grouped into flashes. In addition, we removed positive flashes characterized by peak currents less than 10 kA since these flashes are likely associated with misidentified IC lightning (Cummins et al. 1998; Wacker and Orville 1999a,b). The data were then used to observe the characteristics of CG lightning associated with each convective cell. These characteristics include the time between the first VHF source and the first CG, the time between storm initiation as observed by radar

and the first CG, and the CG flash rate. The times at which each CG flash occurred were also incorporated into the time height cross section plots of VHF source densities for each cell (e.g., see Fig. 20).

2.3 Radar Data

The location, convective state (e.g. developing, mature, dissipating), kinematic and microphysical properties of each convective cell were inferred from the Dallas-Fort Worth (KFWS) and Houston (KHGX) Weather Surveillance Radar 1988 Doppler (WSR-88D) data. These data were acquired from the Nation Climate Data Center (NCDC). Analysis of the radar data was performed using WDSS-II (Warning Decision Support System-Integrated Information) software (Hondl 2003) provided by the Nation Severe Storms Laboratory (NSSL). This software contains several algorithms that allow for quantitative analysis of the intensity of individual convective cells (e.g. Severe Hail Index (SHI) algorithm (Witt et al. 1998) and Vertically Integrated Liquid (VIL)).

2.3.1 Weather Surveillance Radar – 1988 Doppler (WSR-88D)

The WSR-88D uses reflectivity, mean radial velocity, and the variability of radial velocities in a sample volume (spectral width) to produce a suite of meteorological analysis products. These radar data are collected at an azimuthal increment of 1º and at a range increment of 1 km for reflectivity and 250 m for velocity and spectral width (Witt et al. 1998). The number of scans per volume often change depending on the meteorological conditions and the type of information the radar operator deems most valuable at the time of the scan. Figs. 15 and 16 display the two most commonly used

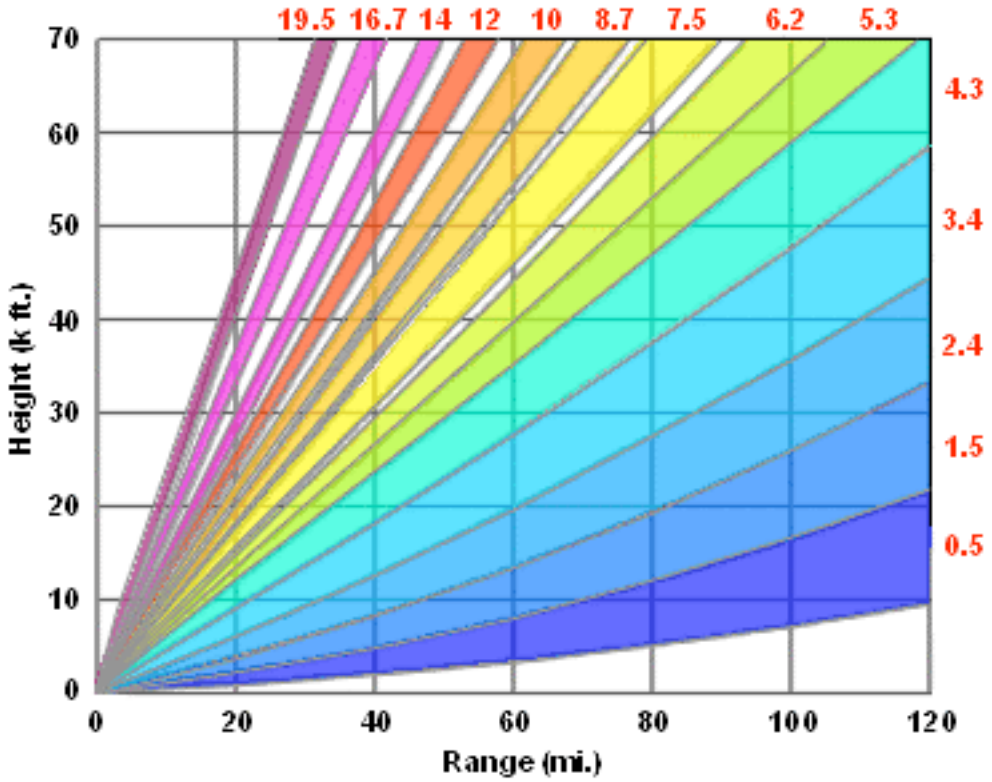

Fig. 15. WSR-88D Volume Coverage Pattern 11 (VCP-11). Scanning strategy consists of 14 elevation scans in approximately 5 minutes (from http://www.srh.noaa.gov/radar/radinfo/)

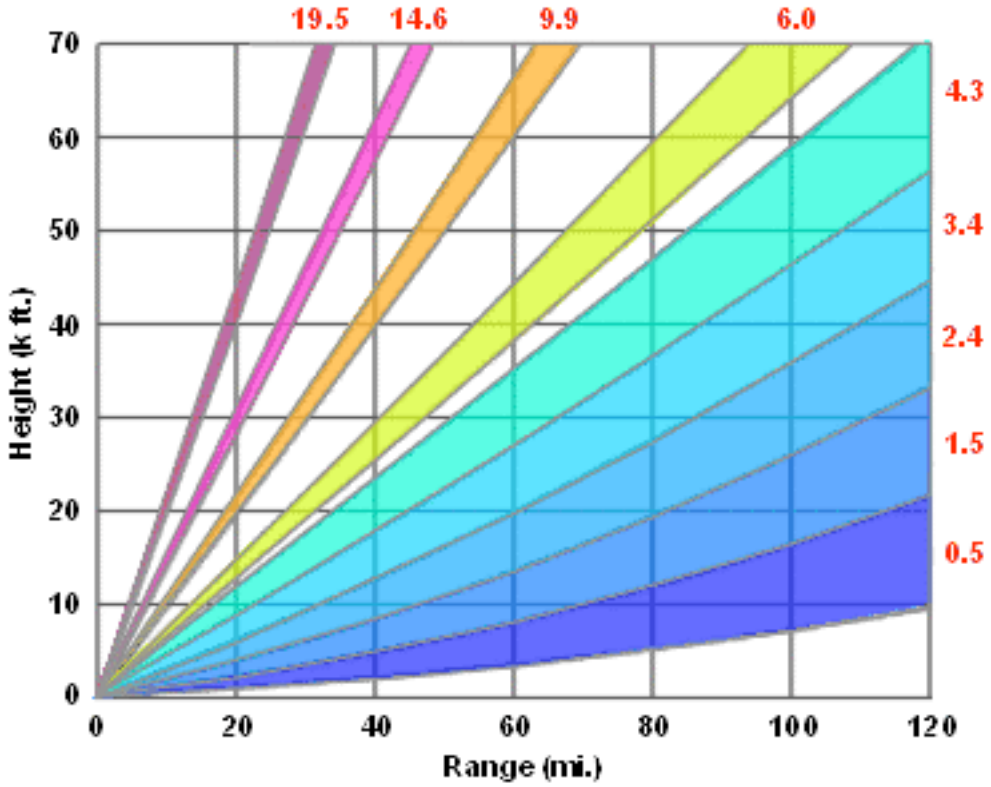

Fig. 16. WSR-88D Volume Coverage Pattern 21 (VCP-21). This scanning strategy consists of 9 scans in 6 minutes (from http://www.srh.noaa.gov/radar/radinfo/).

scanning strategies by the National Weather Service (NWS) forecast offices, Volume Control Pattern 11 (VCP-11) and Volume Control Pattern 21 (VCP-21). VCP-11 consists of 14 unique elevation scans (0.5° - 19.5°) in 5 min and VCP-21 consists of 9 unique scans (also 0.5° - 19.5°) in 6 minutes (Brown et al. 2000a). For storms that extend above the 5° elevation angle, VCP-11 provides much higher vertical resolution in the upper portion of storms as shown in Fig. 15. The coarser vertical and temporal resolution of VCP-21 has raised questions about its ability to adequately sample storms which display the 30 dBZ echo above the 5° tilt. Brown et al. (2000a) examined differences in several radar parameters between the two tilts finding only minor differences between the SCIT information and ±10% difference in the probability for hail (POH) algorithm. However, when the 30 dBZ echo tops exceeded the 5° tilt, differences were noted in the Vertically Integrated Liquid (VIL) 70-80% of the time. Brown et al. (2000b) noted overestimations in VIL of 10-20 km m^{-2} for VCP 21. KHGX operated in VCP 11 for each day examined, while KFWS operated in VCP 11 for two of the four Dallas-Ft Worth cases and VCP 21 for the other two cases. Since the 30 dBZ contours of the cells that occurred on this day extended just beyond the 5° tilt, it is possible that errors in the VIL may have occurred. This may be evident in case 1, which shows high values of VIL that typically correspond to much higher flash rates in other cases (e.g. Fig. 20). This case also occurred 81 km away from the KFWS radar, which could result in the overestimation errors discussed by Brown et al. (2000b). However, in comparison to more complex modes of convection occurring in warm airmasses (Amburn and Wolf, 1997), our cases displayed relatively low values of VIL. Therefore, we do not suspect overestimations of VIL to be a major source of error.

Whether operating in VCP 11 or 21, both scanning strategies are unable to scan the tops of storms that occur within approximately 25 km from the radar due to the maximum elevation angle of 19.5°. This area is called the "cone of silence" where neither scanning strategy can detect portions of the storm above the 19.5° elevation. Therefore, only storms that fell outside the cone of silence, or 25 km range, were considered for this study.

2.3.2 Environmental Conditions Relating to Radar Reflectivity

Radar reflectivity is a measure of the efficiency of a radar target in intercepting and returning (i.e. backscattering) microwave energy. The amount of energy backscattered to the radar is heavily weighted on the size of the target (e.g. Rinehart, 2004). However, several other factors determine how much energy is returned including the number of hydrometeors per unit volume, the size, shape and physical state (ice or water) of the hydrometeor, as well as the aspect ratio of the hydrometeor. The algorithms included within WDSS-II incorporate information on the vertical temperature profile such that inferences on hydrometer types can be made. Vertical temperature profile data were obtained from archived Fort Worth (Lake Charles and Corpus Christi) rawinsonde data from the NCDC. The use of the 00Z versus the 12Z sounding for a particular day was determined by the time at which the majority of the convection occurred. If the majority of the convection occurred before (after) 18Z, the 12Z (00Z) sounding was used. Rarely, however, was a significant difference noted between the 00Z and 12Z sounding for a particular day. Since Houston is not a rawindsone site, the temperature profile over Houston was determined by constructing a linearly weighted average based on the spatial

distance between the Corpus Christi and Lake Charles soundings. WDSS-II ingested information regarding the height of the 0º C and -20º C isotherm for each day to generate its suite of radar parameters.

2.3.3 Radar Reflectivity and Parameters

The magnitude of the reflectivity depends on the number, size, aspect, and dielectric properties of the targets in the sample volume (e.g. Rinehart 2004). The radar reflectivity factor, *z*, which is often referred to as "radar reflectivity," is defined as:

$$z = c_3 p_r r^2 \tag{2}$$

where r is the range of the target from the radar, p_r is the power returned to the radar, c_3 is the "radar constant" which takes into account the scattering properties of the target along with the properties of the radar.

The vertically integrated liquid and vertically integrated ice are derived from the equivalent radar reflectivity factor (z_e), which is the radar reflectivity factor of a hypothetical target that would have the same backscatter properties as the target actually observed. For ice, the equivalent radar reflectivity factor equals the radar reflectivity factor (z) when the Rayleigh approximation is valid (i.e. hydrometeors are assumed to be spherical and smaller than one tenth of the radar wavelength) where z_e is related to z by:

$$z_e = \frac{|K|^2_{ice}}{|K|^2_{water}} z \tag{3}$$

where K_{water} is the dielectric factor for water (0.93) and K_{ice} is the dielectric factor for ice (0.197).

The vertically integrated water content (VIL) is a radar-derived estimate of liquid water above a given point. A fundamental component in the expression relating liquid water mass to radar reflectivity is the assumed raindrop size distribution (DSD). Marshal and Palmer (1948) discovered the dependence of exponentially decreasing drop concentration on increasing diameter, which is given by the following:

$$N(D) = N_o e^{-\lambda D} \tag{4}$$

where N_o = 8000 $m^{-3}mm^{-1}$, D is the droplet diameter (mm), and λ is given by:

$$\lambda = 4.1R^{-0.21} \tag{5}$$

where R is the rain rate in mm/h. Mathematically, the liquid water content, *M*, and radar reflectivity, *Z,* may then be defined as (e.g. Rinehart 2004):

$$M = \frac{\rho_w \pi}{6} \int_0^\infty N(D) D^3 dD \tag{6}$$

and

$$Z_e = \int_0^\infty N(D) D^6 dD \tag{7}$$

where ρ_ω is the density of water. Substituting eqn. (4) into eqns. (6) and (7) and integrating the result yields:

$$Z_e = \frac{N_o \Gamma(7)}{\lambda^7} \tag{8}$$

and

$$M = \frac{N_o \rho_w \pi \Gamma(4)}{6\lambda^4} \tag{9}$$

where $\int_0^\infty x^{\nu-1} e^{-\mu x} \partial x = \frac{\Gamma(\nu)}{\mu^\nu}$ and *Γ(n) = (n-1)!*. Combining eqns (8) and (9) yields:

$$M = \frac{N_o \pi \rho_w}{[720 \times 10^{18} N_o]^{4/7}} Z_e^{4/7} \tag{10}$$

The WSR-88D assumes $N_o = 8\ X\ 10^6\ m^{-4}$ and $\rho_\omega = 10^6\ g\ m^{-3}$ to give:

$$M = 3.44 \times 10^{-3} Z_e^{4/7} \tag{11}$$

and when integrated from base of the radar reflectivity (h_{base}) to the top of the echo (h_{top}) we obtain the final form of VIL:

$$VIL = 3.44 \times 10^{-6} \int_{h_{base}}^{h_{top}} Z_e^{4/7} dh \tag{12}$$

Based on the equations above, higher VIL values require higher reflectivity values, which, due to D^6 in Eqn (7) suggests the presence of larger hydrometeors such as large drops or hail will yield larger values of VIL. In addition the magnitude and spatial distribution of liquid water within a storm indicates the degree of development that has taken place (Greene and Clark, 1972), with increasing values of VIL suggesting a stronger updraft exists within the storm. A measure of the integral of ice water content (M_{ice}) was preformed in addition to the parameters output by WDSS-II where M_{ice} is estimated assuming the Rayleigh approximation (Carey and Rutledge 2000):

$$M_{ice} = 1000 \pi \rho_i N_o^{3/7} \left(\frac{5.28 \times 10^{-18} Z_e^{ice}}{720} \right)^{4/7} \tag{13}$$

and Vertically Integrated Ice (VII) is given by:

$$VII = 1000 \pi \rho_i N_o^{3/7} \left(\frac{5.28 \times 10^{-18}}{720} \right)^{4/7} \int_{-10^\circ}^{h_{top}} (Z_e^{ice})^{4/7} dh \tag{14}$$

where Z_e^{ice} is the equivalent radar reflectivity factor, N_o is the intercept parameter for an assumed inverse exponential distribution for ice (4.0×10^6; Carey and Rutledge 2000),

and ρ_i is the assumed solid ice density (0.917 X 10^6 g m^{-3}). Due to potential radar calibration biases that influence values of Z_e and the natural variability of ice properties that influence the values of N_o, and ρ_i, our assumed values of Z_e, N_o, and ρ_i may not adequately represent the actual conditions at each radar site (KHGX and KFWS). Therefore, sensitivity tests were preformed to test the robustness of each variable, which are explained in further detail within Appendix A.

The VII was calculated using a FORTRAN program that first transforms the radar reflectivity from its logarithmic form:

$$Z = 10\log_{10}\left(\frac{z}{1mm^6m^{-3}}\right) \tag{15}$$

to its linear form:

$$z = 10^{\frac{Z}{10}} \tag{16}$$

and then takes the average reflectivity value within the specified bounds of the cell in 1 km elevation bins. If the reflectivity values are located above the -10º C isotherm, then the associated ice mass for that particular level is calculated giving a value in g m^{-3}, which is converted to kg by multiplying through by the following conversion factor: ((1000 m km^{-1})^3 * 1000 g kg^{-1}). Once the ice mass values are calculated for each bin, they are added together to represent the total ice mass for the storm during that time. The final value for the total ice mass during a particular radar volume scan is reported at the time at which the volume scan started. Since an entire volume scan takes approximately 5 minutes to complete it did not seem appropriate to associate the start time with any real time lightning activity reported by either lightning networks. Therefore, the start times of the VII were shifted forward by two minutes to better represent the lightning activity

which could be occurring at that time. A three minute shift was also used to test any potential differences in the time lags.

In addition to VII, the Severe Hail Index (SHI), which was developed as a severe hail predictor, was also examined as a potential proxy for the amount of ice available for non-inductive charging. The SHI as calculated by WDSS-II is given by:

$$SHI = 0.1 \int_{H_o}^{H_T} W_T(H) \dot{E} dH \qquad (17)$$

where W_T is a temperature based weighting function, H_0 is the height ARL (above radar level) of the environmental melting level, H_T is the top of the storm cell, and $\dot{E}$ is the Hail Kinetic Energy Flux (Witt et al. 1998). W_T is given a value of zero if the height ARL is below the 0° C isotherm, and a value of 1 if the height ARL is above the -20° C isotherm. If the height ARL is between the 0° and -20° C isotherms then W_T is given by $W_T = \frac{H - H_o}{H_{m20} - H_0}$ where H_{m20} is the height of the -20° C isotherm. Therefore, higher SHI values will result as both the height above the melting level and radar reflectivity values increase.

2.3.4 Individual Cell Tracking Via Radar

Identification and tracking of each convective cell was performed with the WDSS-II Storm Cell Identification and Tracking (SCIT) algorithm (Johnson et al. 1998). In an effort to obtain cells that were representative of airmass thunderstorms as described by Byers and Braham (1949), we employed certain criteria that were used to assess whether a cell could be a part of our sample. These criteria included:

1) Radar must capture the entire life span of the cell.

2) Distance from cell to center of the LDAR network could not exceed 100 km during cell's life span.

3) Cell must remain isolated from other convective cells such that VHF sources from one cell could not enter another (tests were made for each cell in order to ensure this did not occur).

4) Cell did not undergo a merge or split during its lifetime.

5) Cell must be identified by WDSS-II algorithms for 30 minutes or greater.

6) 30 dBZ contour observed at or above -10º C level for at least one scan in effort to focus on electrified storms (e.g. Vincent et al. 2003).

7) Cell has no appreciable tilt.

8) Network was fully operational with at least 5 sensors recording data.

Despite the criteria listed above, the process of identifying a convective cell that consisted of a single main updraft remained somewhat arbitrary. This is because we relied on radar reflectivity data, rather than vertical wind velocity data, to determine if a cell appeared to have a single updraft. Due to this somewhat grey area, we put most of the emphasis on the "single cell" classification towards the appearance of the radar reflectivity associated with the individual cell. Only those cells that displayed a single core of enhanced radar reflectivity at the -10º C isotherm, and remained isolated from other cells, were accepted as valid cells. However, even though the reflectivity signature during a single volume scan may suggest a single updraft, several cases appear to have consisted of multiple updrafts that "pulsed" during the lifetime of the storm. This may help explain why a few cells we chose to accept as valid had lifespans well beyond the conventional Byers and Braham (1949) single cell conventional model of approximately 55 to 75 minutes. Nevertheless, these cells did not experience significant dynamical (e.g.

merging updrafts), electrical (e.g. multiple storms in close proximity resulting in a local dipole) or microphysical (e.g. merging microphysics from cloud seeding) effects that could come from a merge, split or more complex convective modes and it seems reasonable to assume these cells followed the general convective processes of ordinary convection. A possible caveat to accepting cases that displayed multiple pulses in the updraft, however, could come from inferences made between the timing of the first VHF sources or first NLDN detected CGs. This problem could occur if a first minor pulse caused a few VHF sources with the next pulse taking several tens of minutes to generate any IC or CG activity. This will be discussed further in subsequent sections, but the main idea remains that these cases still provided valuable information regarding the general convective processes of airmass thunderstorms, thus they were considered valid cases.

2.4 Convective Cell Bounds

Since most convectively active days had several cells occurring at the same time, the LDAR data for a given day usually contained VHF source point information for a number of cells. Thus, if a cell met the required criteria, it was necessary to separate the VHF sources associated with the cell of interest from the plethora of VHF sources that occurred from all cells within range of the LDAR network. This was performed by constructing a cylinder around each cell such that VHF sources that fell outside the bounds of the cylinder would not be associated with the cell of interest (Fig. 17). The center and radius of each cylinder were constructed based on the ice-ice collisional (or non-inductive) charging mechanism (Takahashi, 1978). The presence of a sufficient quantity of graupel or hail, with ice crystals and supercooled water for charging, is

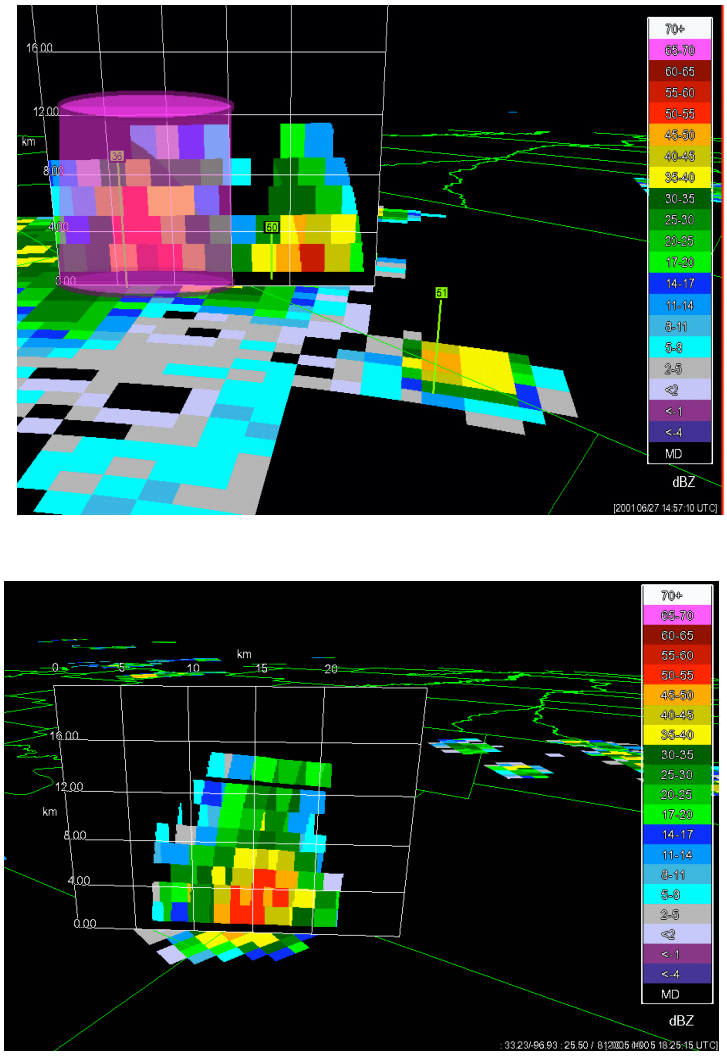

Fig. 17. 3-D depiction of radar reflectivity, dBZ shown. a) Vertical cross section taken through a cell occurring on 27 June 2001 during peak intensity at 1457 UTC (t = 35 minutes). Shaded cylinder constructed around cell shows bounds of the cell. Cross-section grid box spacing is 4km in the vertical plane and 5km in the horizontal plane. (b) Same as (a), but for cell 1 with vertical cross section taken during peak intensity at 1825 UTC (t = 40) minutes).

typically associated with radar echoes approaching 30-40 dBZ between the -10º C and -20º C isotherm level (e.g. Dye et al. 1986). Previous studies have also shown that the main negative charge region typically resides around the level of the -10º C isotherm (e.g. Krehbiel 1986).

Therefore, the center and radius of each cylinder were based on reflectivity values at the height of the -10º C isotherm with the center of the cylinder being placed at an approximate center point of the cell. The radius of each cylinder extended out to the furthest 20 dBZ contour from the cell's center in effort to capture the most electrically active portion of each cell. Fig. 17a shows one of the few cases in which the bounds of the cell came in close proximity to another cell. However, measures were taken to reduce the likelihood of VHF sources from neighboring cells from entering the bounds of another. One such measure incorporated flash origin information from the flash algorithm to exclude any VHF sources of a flash that did not originate within the specified bounds of the cell. In addition, the main negative charge regions of both cells (as inferred by the 20 dBZ echo above the -10° C isotherm) remained at distances greater than 10 km from one another. Thus, given that flash origins typically occur in close proximity to the main negative charge region (Proctor 1991), it is unlikely that flashes from one cell could be associated as a flash from another. However, cells that came within close proximity of another did so during at least one cell's dissipating stage, when no VHF sources were being recorded for the dissipating cell.

Latitude and longitude information for the center of each cylinder were recorded using the active readout display from WDSS-II, which allows for a mouse-over latitude/longitude readout. This information was then combined with the flash output

from the NASA flash algorithm such that only those flashes that had origins within the bounds of the cell were associated with the cell. Since it is possible that some flashes could originate outside the bounds of each cell, we selected three cases, all of which were isolated from other convective cells, and performed sensitivity tests with the cell bounds. In each case, the cell radii were expanded by 100% to test the possibility of flashes occurring outside the range of the former bounds. All cases maintained the same number of flashes with the newly expanded radii suggesting the radii for all cells examined captured all the detected lightning activity associated with each cell.

Comparisons were made between radar reflectivity values and total lightning data (i.e. LDAR source points and CG data) by converting radar data from a polar to a Cartesian grid space using REORDER software (Oye and Case 1995) and overlaying both data sets. Horizontal and vertical grid spacing for the reflectivity data were set at 2.0 km and 1.0 km, respectively. The x, y, and z radii of influence were set to 2.0, 2.0, and 1.1 km respectively, and a three-dimensional Cressman weighting scheme (Cressman, 1959) was used to derive Cartesian grid points from polar radar data.

The Cressman weighting scheme is a function of the grid spacing and the radii of influence. The radius of influence, R, is defined as:

$$R = dX^2 + dY^2 + dZ^2 \tag{18}$$

The weighting function, W, for a given gate is value is defined as:

$$W = \frac{R^2 - r^2}{R^2 + r^2} \tag{19}$$

Where r^2 is the square of the distance between the gate and the grid point such that grid points located closer to a particular gate with have more weight than grid points further away.

The reflectivity data associated with each cell were interpolated over 1 km altitude bins. Despite coarse vertical interpolation and occasional gaps in the radar data, the smoothing performed creates a general idea of the vertical distribution of reflectivity values such that the two datasets (total lightning activity and radar reflectivity) can be overlaid.

Once the reflectivity, VII, and flash rates were obtained, several datasets were created to provide a general sense of the correlations between total flash rates and the kinematic and microphysics of each cell. The parameters examined include the 95th and 75th percentile of flash heights, the median and mean of flash heights, and the total and CG flash rates. We then used this lightning information to conduct regression analysis between LDAR total (or NLDN CG) and radar derived VII using the r^2 value as a measure of the goodness of fit.

2.5 Statistics Performed

Several IDL programs were employed to compare various radar parameters against the cell total and vertical profile of flash density, flash origin density, and flash source density for several air mass thunderstorm cases. All data sets were placed on the same temporal scale such that accurate comparisons between data sets could be made. VHF source densities were normalized over a 5-minute period while CG and IC flash

rates were smoothed using a 5-minute running average. The VHF source density was girded at 1 km resolution in the vertical for time-height cross-sections.

Due to the coarse temporal resolution of the WSR-88D data, various time lags were implemented such that the reported time of each radar scan would correspond to the time of VHF derived flash statistics. For example, the first radar volume scan of each cell occurs at time t=0 with the next radar scan occurring approximately 5 minutes later at time t=5 min. Total and CG flash counts, which are tallied every minute, are placed into a 5 minute running averages. Therefore, the flash rate at time t=2 min is a 5-minute running average of flash rate from times t=0 min, t=1 min, t=2 min, t=3 min, and t=4 min. Since time t=2 min occurs approximately half way between the start and stop time of the radar volume scan, it is assumed that this time is most representative of the information compiled by the WRS-88D during the volume scan. Therefore, the time of the first radar volume scan (reported as time t=0 min) is adjusted 2 minutes forward and compared against the five minute running average of flash data at time t=2. To test the robustness of the time lag, a lag of t=3 minutes was also examined.

Trends in flash heights were also monitored. The average height of VHF sources for each flash provide the height information for a given flash. Once the heights of each flash for a 5-minute period were obtained, the mean, median, 95^{th} percentile, and 75^{th} percentile of the flash heights for each 5-minute period were calculated through IDL programs. This data was then compared to both the radar inferred intensity parameters and total and CG flash rates to examine possible correlations between the two data sets.

2.6 Environmental Conditions

Rawindsonde data from each location also provided information on various synoptic conditions including wind shear and instability. Past research has shown that the amount of vertical wind shear and convective available potential energy (CAPE) play a critical role in the mode of convection (e.g. ordinary cell, multicell, supercell) observed (Weisman and Klemp, 1982). Higher shear values coupled with higher buoyancy tend to lead to more complex modes of convection (e.g. supercells, organized multicell convection). The 0-6 km wind shear is the magnitude of the velocity vector difference over a specified vertical depth (surface to 6 km in this case). The values are typically reported in m s^{-1} or knots.

Although convective mode is highly dependant on the amount of vertical wind shear, the amount of instability, or energy, available to an ascending air parcel can also control the convective mode by influencing the strength of the updraft. The Convective Available Potential Energy (CAPE) is a measure of atmospheric instability and is given by:

$$CAPE = \int_{p_n}^{p_f} (\alpha_\rho - \alpha_e) dp$$

where α_e is the environmental specific volume, α_p is the specific volume of a parcel moving upward moist-adiabatically from the level of free convection, p_f is the pressure at the level of free convection, and p_n is the pressure at the level of neutral buoyancy. CAPE and 0-6 km shear values were obtained from the same three sounding networks that provided the -10° C and -20° C isotherm data. Again, since no sounding data were

available for Houston, the values for Houston were obtained by the aforementioned weighting method between the Lake Charles and Corpus Christi soundings.

3. RESULTS

3.1 Cell Locations

Twenty-two ordinary convective cells, (i.e. airmass thunderstorms), were selected for this study. Thirteen of these cells occurred over the TAMU LDAR network, while the other 9 cases occurred over the Dallas LDAR network. Each cell displayed minimal tilt with height, did not undergo a merge or split, and remained well isolated from other convection. Tables 2 and 3 show information regarding the location, maximum total lightning flash rates, and various other parameters for all 22 cells. Although the average maximum flash rate for all 22 cases is 7.0 flashes min^{-1}, Dallas cases tended to have higher total flash rates with an average maximum flash rate of 10.9 flashes min^{-1} compared to 4.3 flashes min^{-1} for Houston cases. The highest total flash rate of all 22 storms occurred in Dallas with case 7, in which a maximum flash rate of 36.2 flashes min^{-1} was observed. Despite the high flash rate, case 7 still displayed the characteristics associated with ordinary convective cells. The lowest flash rate of 1.2 flashes min^{-1} occurred with case 21, but low flash rates of 1.8 were observed in three cases: 4, 15, and 18. These results are very similar to past results examining ordinary non-severe storms as reviewed in Williams 2001 (Table 4). His table comprises several previous studies, which show maximum total flash rates ranging from 1 flash per minute to about 60 flashes per minute, with three flashes per minute being a typical value according to Williams (2001). These low flash rate storms typically had very high CG to total flash rate ratios, which will be examined further in upcoming sections.

Table 2. The time span between cell initiation and the time at which the average 30 dBZ contour crosses the -10° C isotherm (INTN TO -10°C) for all 22 cases.

CASE #	INTN TO -10°C
1	0:27
2	0:11
3	0:09
4	0:05
5	0:11
6	0:02
7	0:07
8	0:00
9	0:14
10	0:34
11	0:14
12	0:00
13	0:47
14	0:06
15	0:00
16	0:14
17	0:30
18	0:10
19	0:02
20	0:35
21	0:22
22	0:13
AVE	0:14:14
STDEV	0:13:00

Table 3. Columns from left to right: The cell identification number of all 22 cells; month, day, and year cell developed; LDAR location cell occurred; maximum LDAR estimated total lightning flash rate (Max FR); average distance (Ave Dist) from center of respective LDAR network.

Cell #	mm/dd/yy	Location	Max FR	Ave Dist
1	6/27/01	DFW	9.0	75
2	6/27/01	DFW	2.6	31
3	7/22/05	DFW	20.4	58
4	8/5/05	DFW	1.8	27
5	8/5/05	DFW	12.2	57
6	8/5/05	DFW	2.4	52
7	8/5/05	DFW	36.2	46
8	8/6/05	DFW	6.0	9
9	8/6/05	DFW	7.6	59
DFW AVERAGE			**10.9**	**46**
10	8/20/05	HOU	2.8	64
11	8/20/05	HOU	9.2	91
12	8/20/05	HOU	4.0	59
13	8/20/05	HOU	2.8	54
14	8/20/05	HOU	6.4	67
15	8/25/05	HOU	1.8	62
16	8/25/05	HOU	8.2	85
17	8/25/05	HOU	5.6	97
18	9/13/05	HOU	1.8	42
19	9/13/05	HOU	4.6	8
20	9/13/05	HOU	2.8	74
21	9/13/05	HOU	1.2	47
22	9/13/05	HOU	4.6	53
HOU AVERAGE			**4.3**	**61.77**
HOU AND DFW AVERAGE			**7.0**	**55.32**

Table 4. The maximum flash rates observed from several studies examining ordinary non-severe thunderstorms (From Williams 2001).

Investigators: Location	Maximum Flash Rates (Flashes min^{-1})
Lhermitte and Krehbiel (1979): Florida	60
Lhermitte and Williams (1985): Florida	4
Dye et al. (1986): Montana	1
Krehbiel (1986): Floriday	<1
Nisbet (1990): Floriday	16
Goodman et al. (1988): Alabama	22
Williams et al. (1989):	6
Buechler and Goodman (1990): Alabama	15
Williams (1991): Australia	40-60
Malherbe et al. (1992): Florida	14
Carey and Rutledge (1996): Colorado	10
Rison et al. (1996): Florida	3
Stanley et al. (1996): Florida	4

The average distance of all 22 cells from the center of their respective LDAR networks is 55.32 km, with two cases (cases 8 and 19) falling within 10 km of the LDAR networks and one case (case 17) falling at an average distance of 97 km. As will be shown, the vertical distribution of VHF sources associated with various cases appears to be partially dependant on the cells distance to the center of the LDAR network.

Figs. 18 and 19 show the location of each cell (red diamonds numbered 1-9 for Dallas cases and 10-22 for Houston cases, respectively) and LDAR sensor locations (green circles) with the grid centered on the center of each LDAR network. The black circle depicts a 100 km range from the central location of the LDAR network. The maximum distance of each cell from the center of its respective LDAR network ranged from 10 km (cell 19) to 100 km (cell 17) with an average maximum distance of 61 km. Only cells that remained within the 100 km range ring during their entire lifespan were used.

3.1.1 Synoptic Setup

Past research has shown a strong relationship between CAPE, vertical air motions, the microphysical and vertical extent of ice particles, and the resulting electrical activity (Williams 2001). Variations in the amount of CAPE lead to variations in the size and vertical distribution of hydrometeors that contribute to charge separation. The atmospheric conditions conducive toward ordinary convection consisted of a moderately unstable airmass with low vertical wind shear. Similar to the results discussed in Weisman and Klemp (1982), wind shear values appeared to be the main control over convective mode. Higher vertical wind shear resulted in cells favoring a muticellular

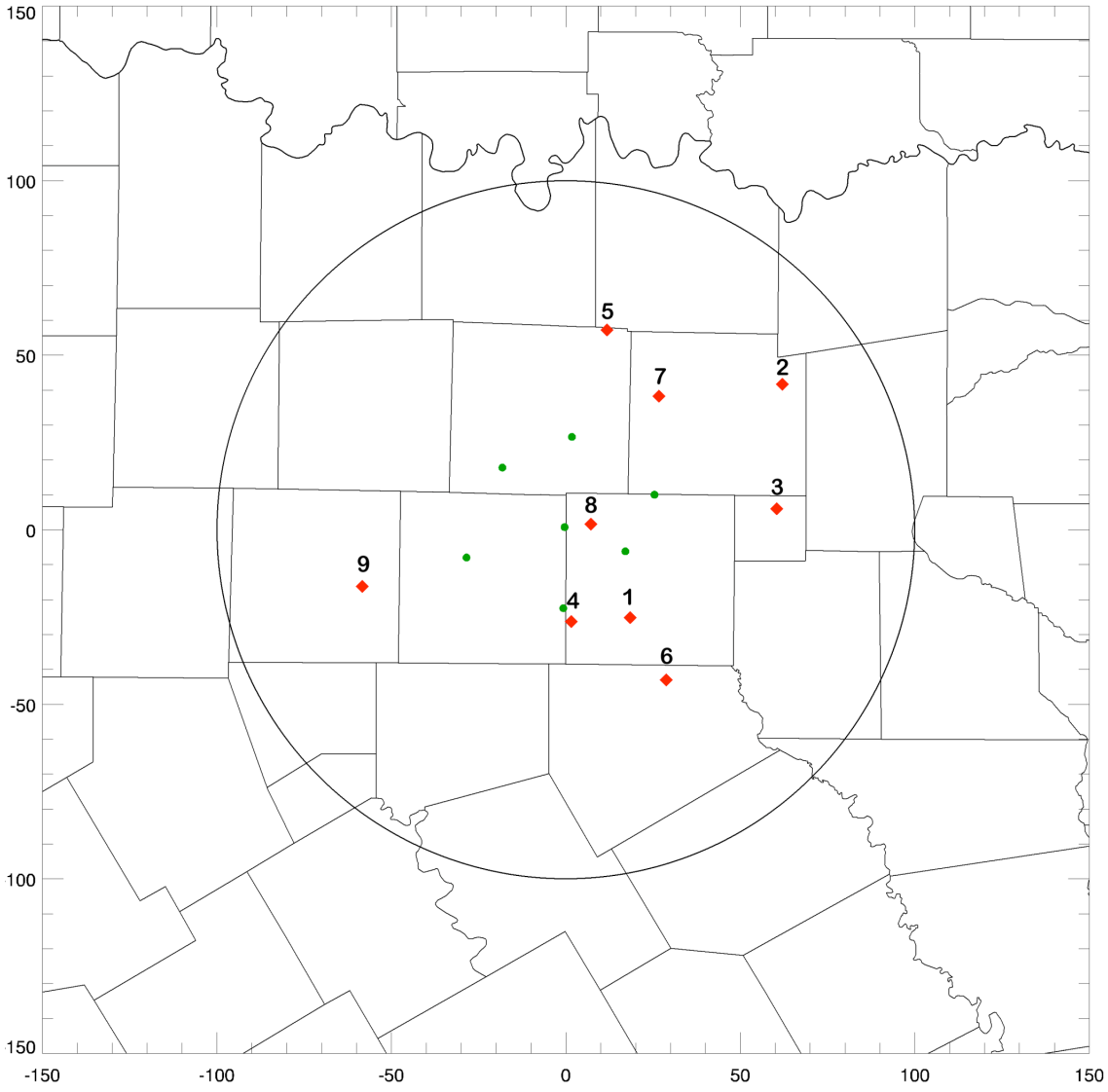

Fig. 18. Location (red diamonds) and cell identification numbers from Table 2 for the nine cases examined in Dallas. Green circles represent location of LDAR sensors. Black ring represents 100 km range from center of the LDAR network.

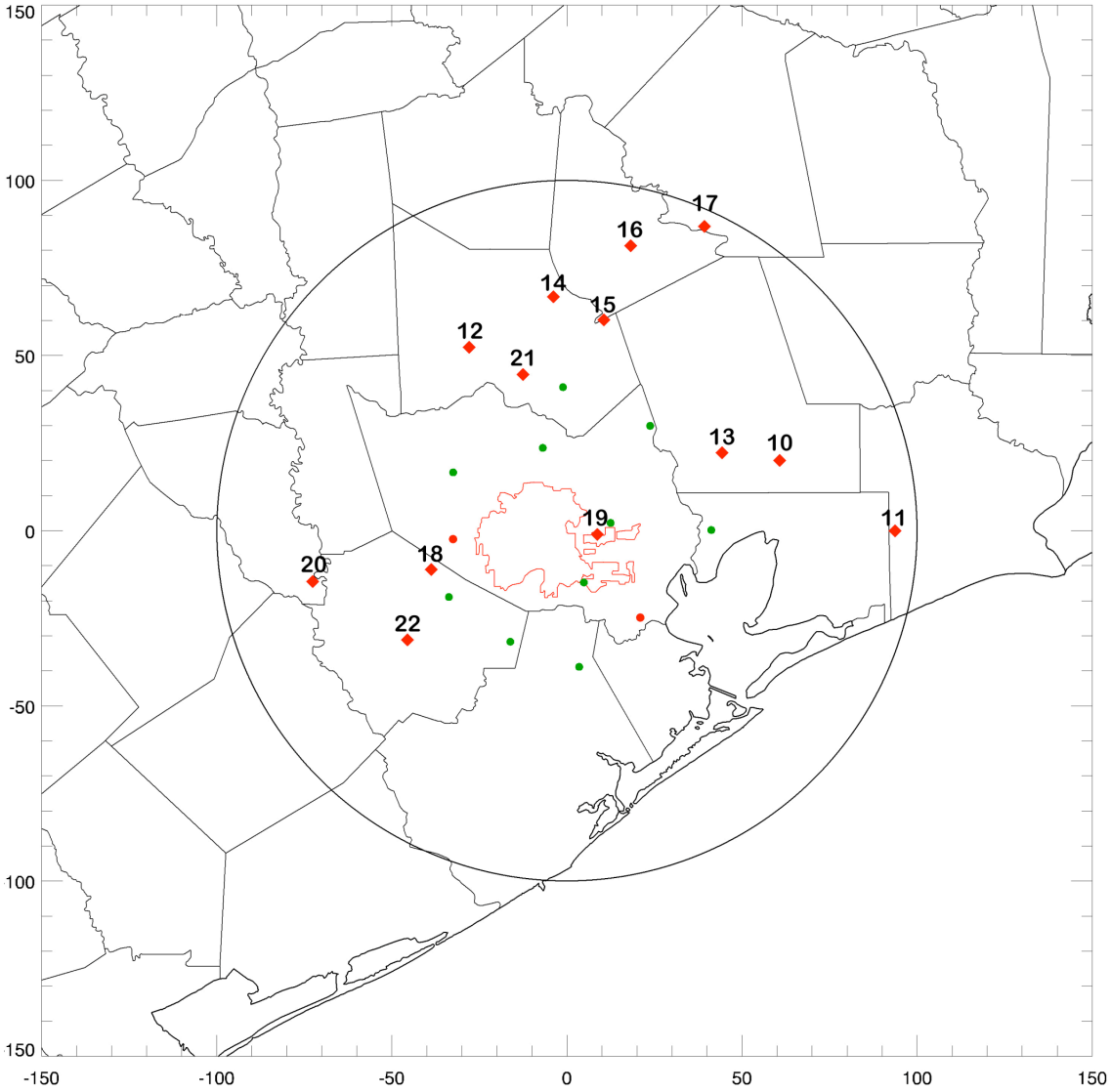

Fig. 19. Same as Figure 18, but for all 13 Houston cases. Note: the two red circles represent inoperable sensors during period of study.

convective mode, and low vertical wind shear promoted isolated ordinary convective modes. Table 5 displays instability, isotherm heights, and shear parameters for each of the seven case days. The average CAPE value of 1166 J kg^{-1} suggests a moderately unstable atmosphere was required to generate enough buoyancy for convective updrafts.

The 0-6 km wind shear remained very low for each case, with an average value of 5.7 m s^{-1}. According to Weisman and Klemp (1982), the bulk Richardson number typically exceeds 30 on days in which ordinary convection is the main convective mode, which generally follows the results of our study. Given the weakly sheared and low to moderately unstable environments, several of the isolated convective cells occurring on these days did not have any VHF sources associated with them. In addition, base (0.5°) velocity and reflectivity scans show that the majority of the convective cells, upon the decaying stage, generated a cold pool associated with downdraft modified air, which often initiated new convection along the cold pool boundary. This typically resulted in a merger of the old and new cell making it difficult to distinguish between the two original cells, thus violating the criteria set for an isolated convective cell. Therefore, capturing purely isolated convective cells during their entire lifespan became slightly more difficult that originally anticipated. Although we did not examine the cases that had lightning flash rates lower than 1 flash per minute, future work may consider examining some of these null cases, since some of these cases displayed radar inferred intensities similar to our lower flash rate storms.

Table 5. Upper air conditions for each day examined showing values for Convective Available Potential Energy (CAPE); Convective Inhibition (CIN); 0-6 km shear, the height of the -10°C and -20°C isotherms, and the Bulk Richardson Number (R).

dd/mm/yy	CAPE ($J\ kg^{-1}$)	CIN ($J\ kg^{-1}$)	0-6 km Shear (ms^{-1})	-10° C Height (km)	-20°C Height (km)	R
06/27/01	1678	118	8.83	5.9	7.3	43.0
07/22/05	503	172	11.31	6.4	8.2	7.9
08/05/05	163	206	1.54	6.4	7.9	137.5
08/06/05	1267	138	5.66	6.4	7.9	79.1
08/20/05	1150	108	3.6	6.8	8.5	177.5
08/25/05	2098	61	2.06	6.8	8.8	988.8
09/13/05	1305	22	7.72	6.7	8.1	43.8
Average	**1166**	**118**	**5.73**	**6.5**	**8.1**	**212.0**

3.2 Evolution of Lightning, Kinematics and Microphysics in Ordinary Convective Cells

Time height cross-sections, total and CG flash rates, and the radar inferred kinematic and microphysics of each cell are compared in Figs. 20 through 41. The results from each case will now be presented.

3.2.1 Dallas Fort-Worth Cases

3.2.1.1 27 June 2001

Two ordinary thunderstorms, which fell within 100 km of the Dallas Fort Worth LDAR network, were examined on 27 June 2001. Fig. 20 shows case number 1, which lasted for approximately 80 minutes and produced a total of 30 flashes, each flash depicted by the x's in Fig. 20a, with the first flash occurring 31 minutes (t = 31 min) after cell initiation. Interestingly, the first flash also coincided with a brief peak in the VII as shown in Fig. 20c with the next flash occurring only after a subsequent peak in the VII approximately 14 minutes later. The peak value in VIL occurs at t = 34 min, which coincides with an increase in cell intensity as inferred by an increase in the height of the average 25 dBZ contour into the mixed phase zone (T<-10° C) where significant charge generation typically occurs (Dye et al. 1988). The VIL then begins to descend with the maximum flash rate of 2.6 flashes min^{-1} occurring 20 minutes after the peak in VIL and 8 minutes after the peak in VII suggesting VII follows trends in total flash rates as demonstrated in past research (e.g. Carey and Rutledge 2000). During this time (t = 54 min), the height of the maximum in VHF source densities remains fairly constant at approximately 8 km, with a fairly wide scatter of flash origins. This is noticeably

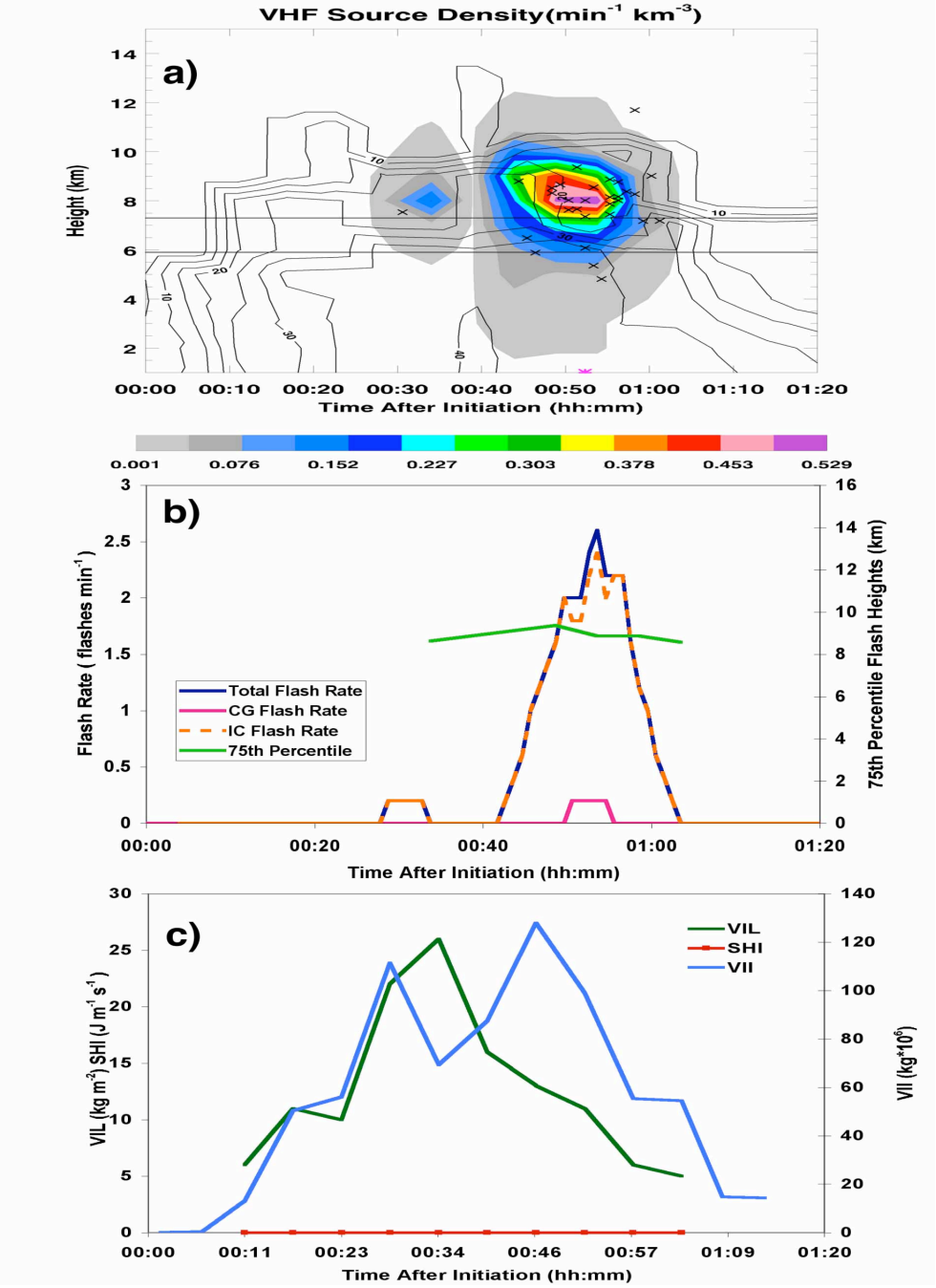

Fig. 20. Three panel plots (labeled a, b, and c) for case 1 where: a) Time (after cell initiation) height (km) cross sections of VHF source density (colored shading), flash origin locations (x), CG times (*) and radar reflectivity (dBZ, contoured starting at 5 dBZ every 5 dBZ). b) 5-minute running average of lightning flash rate for total lightning data (blue line), CG flash rate (red line), and the 75th percentile (green line) and median (orange line) of flash heights. c) Vertically Integrated Liquid (VIL, kg m^{-2}; green line), Severe Hail Index (SHI, J m^{-1} s^{-1}; red line), and Vertically Integrated Ice (VII) mass (kg*10^{6}; Blue line) integrated from the height of the -10° C isotherm to echo top multiplied through by cell area and 10^{-6}.

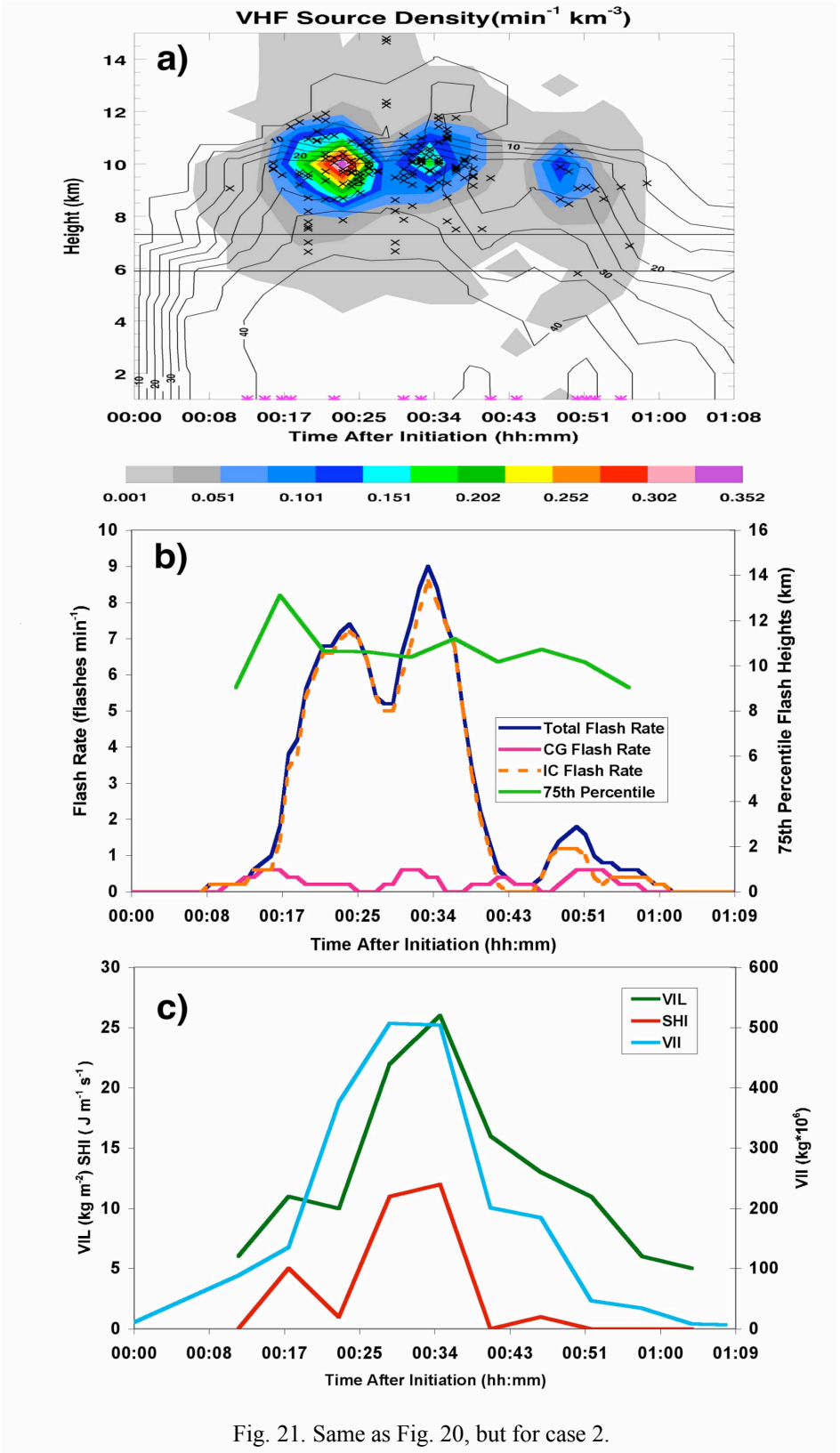

Fig. 21. Same as Fig. 20, but for case 2.

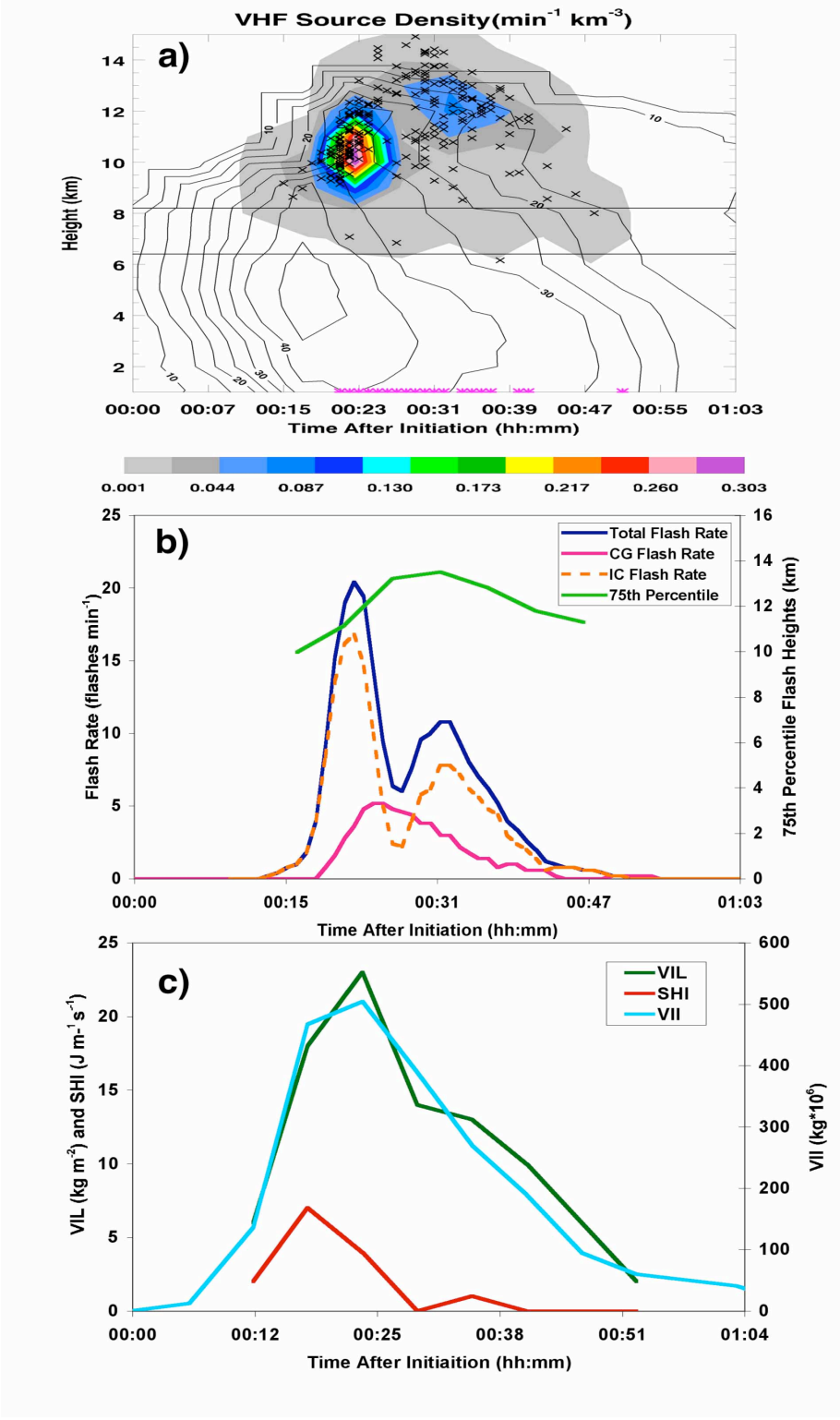

Fig. 22. Same as Fig. 20, but for case 3.

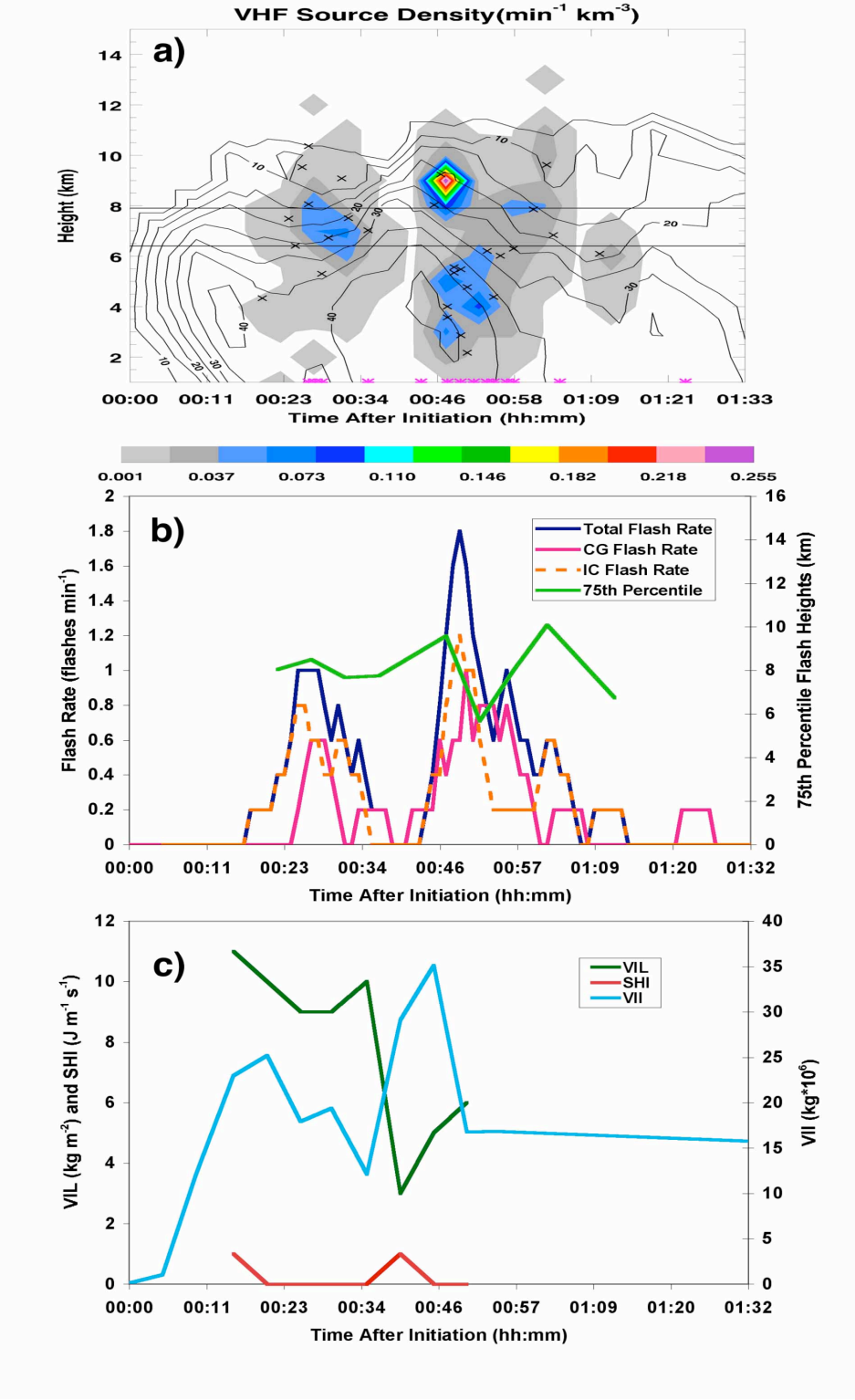

Fig. 23. Same as Fig. 20, but for case 4.

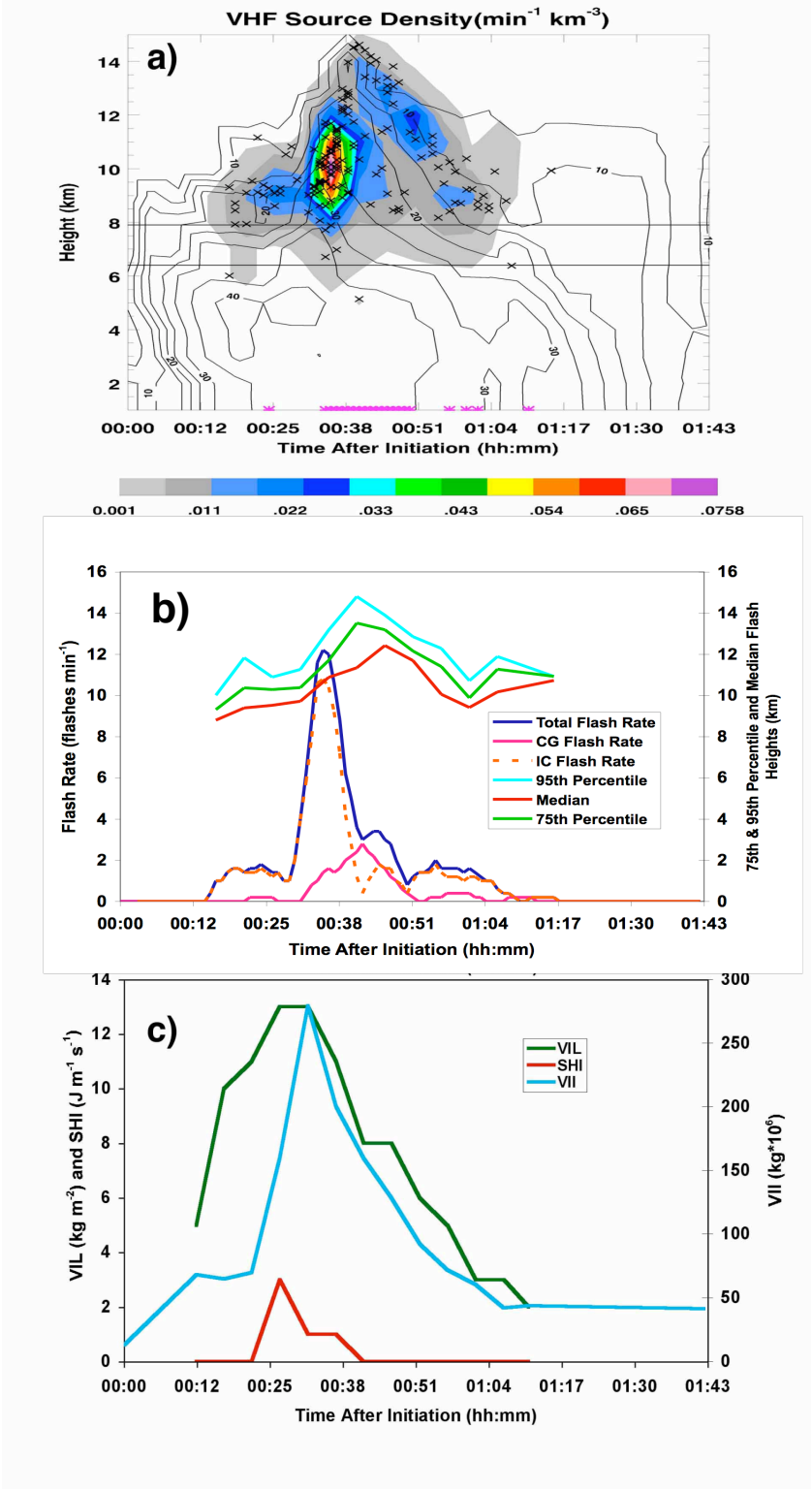

Fig. 24. Case 5, which is the same as Fig. 20 except for the addition of the 95th (light blue line) and median (dark red line) flash heights in frame b.

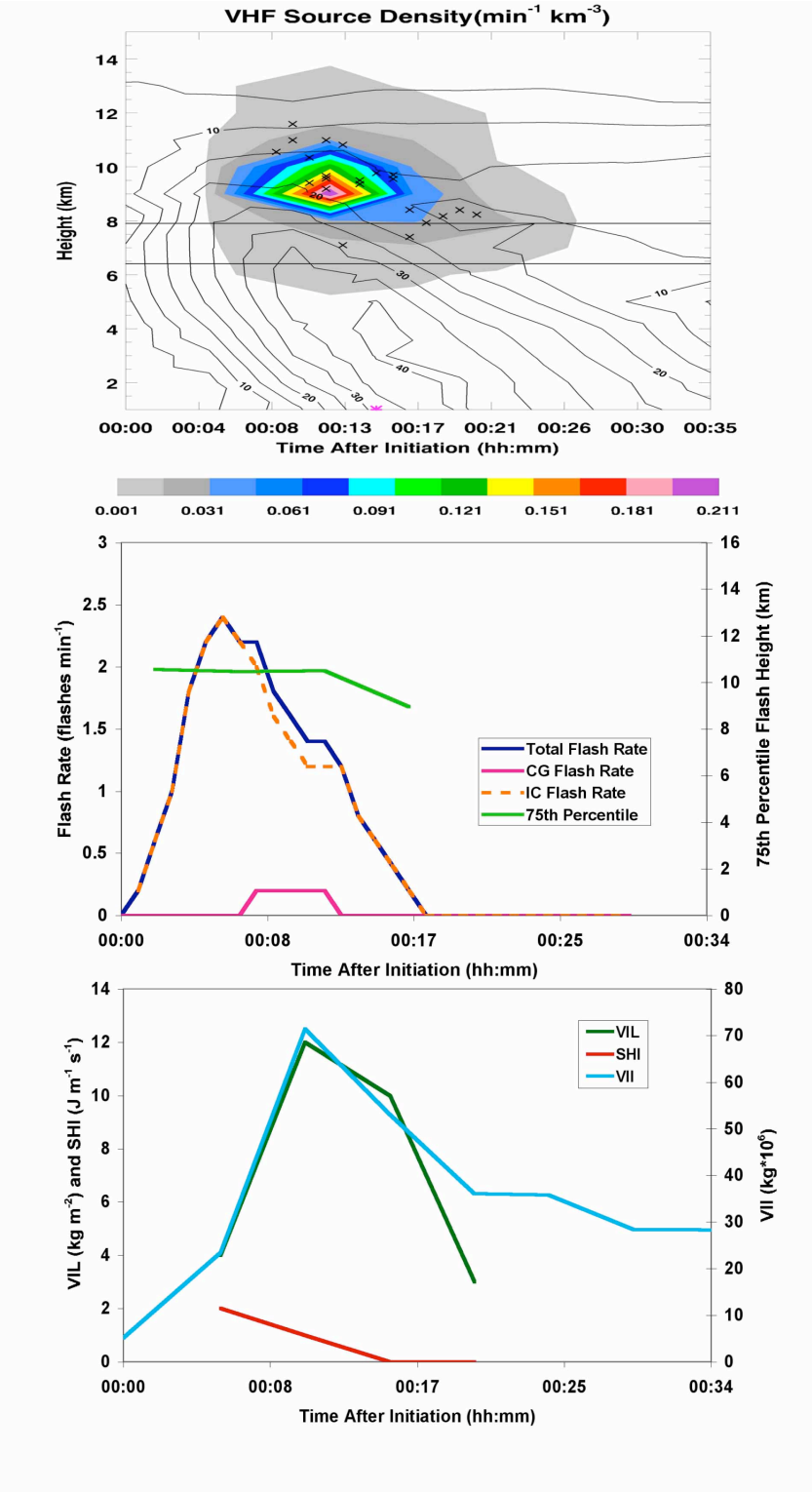

Fig. 25. Same as Fig. 20, but for case 6.

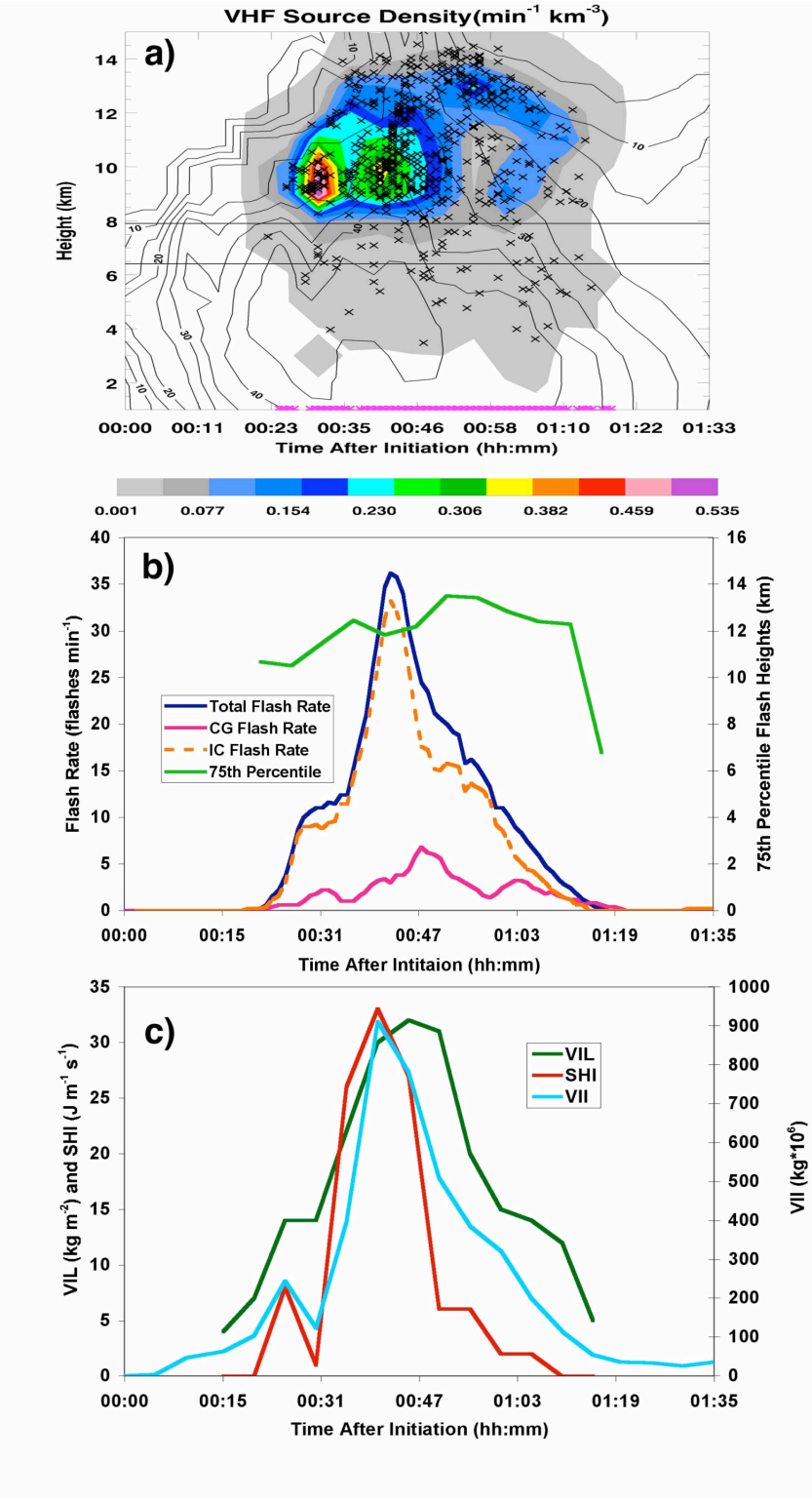

Fig. 26. Same as Fig. 20, but for case 7.

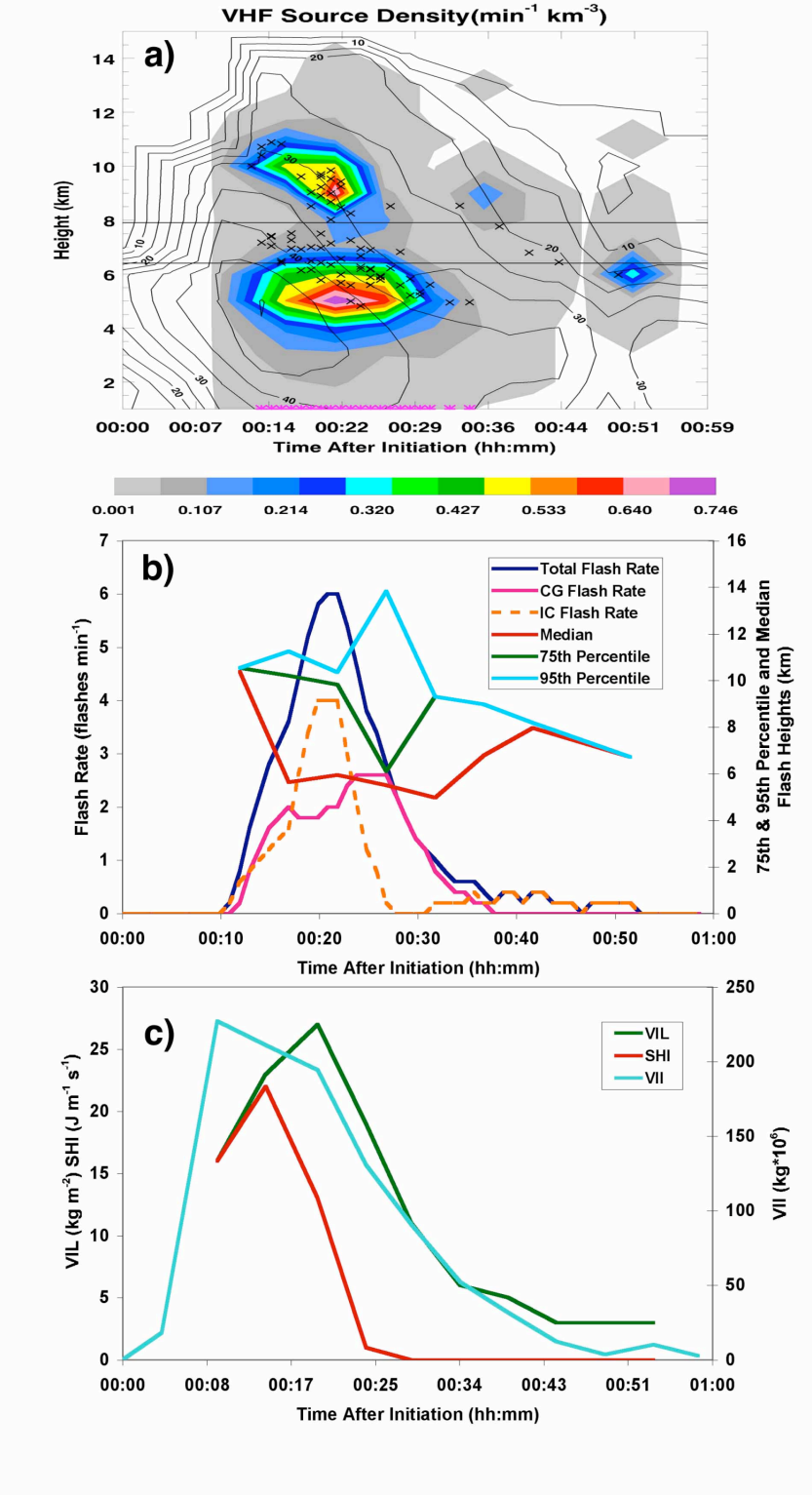

Fig. 27. Case 8, which is the same as Fig. 20 except for the addition of the 95th (light blue line) and median (dark red line) flash heights in frame b.

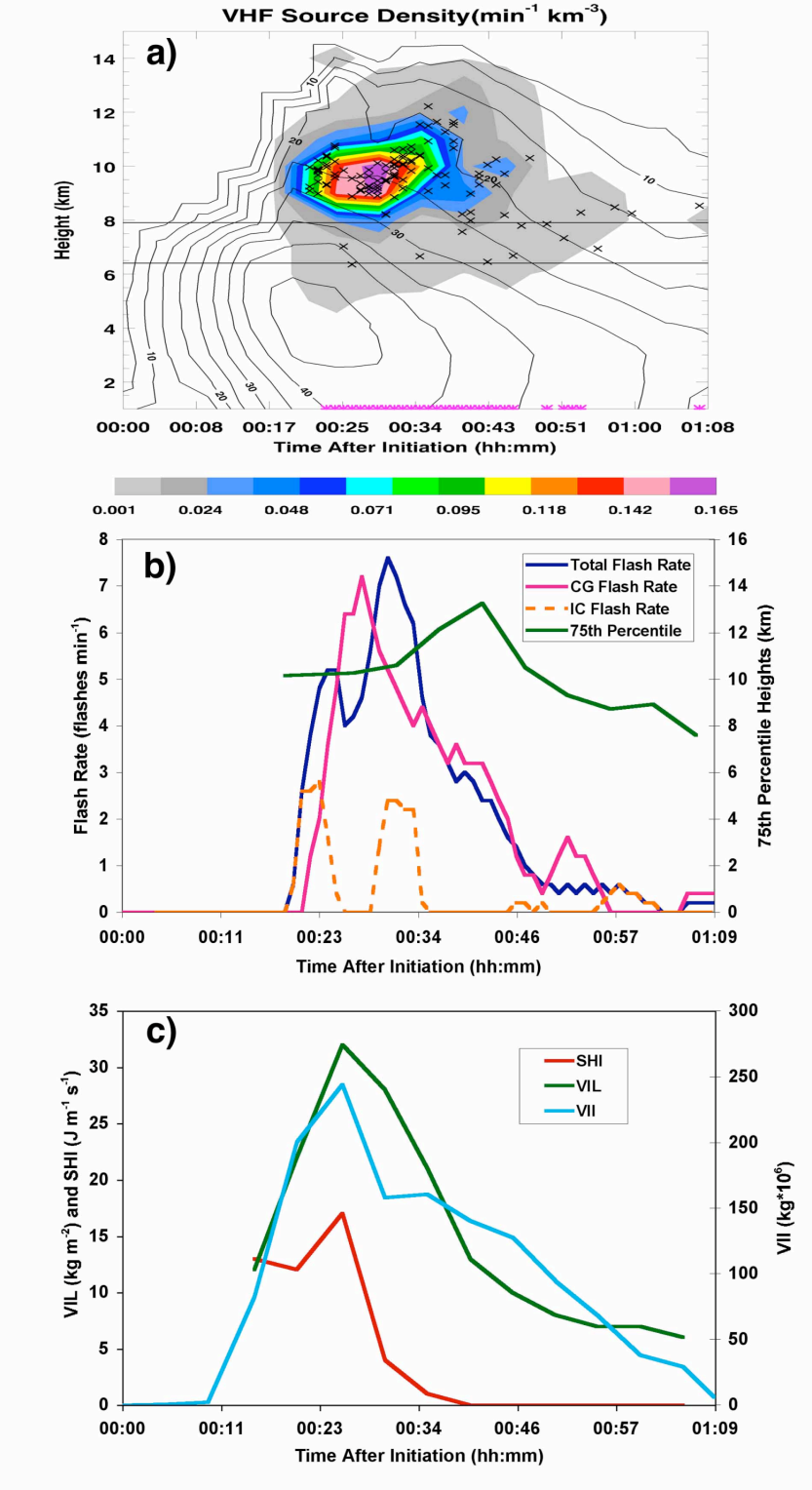

Fig. 28. Same as Fig. 20, but for case 9.

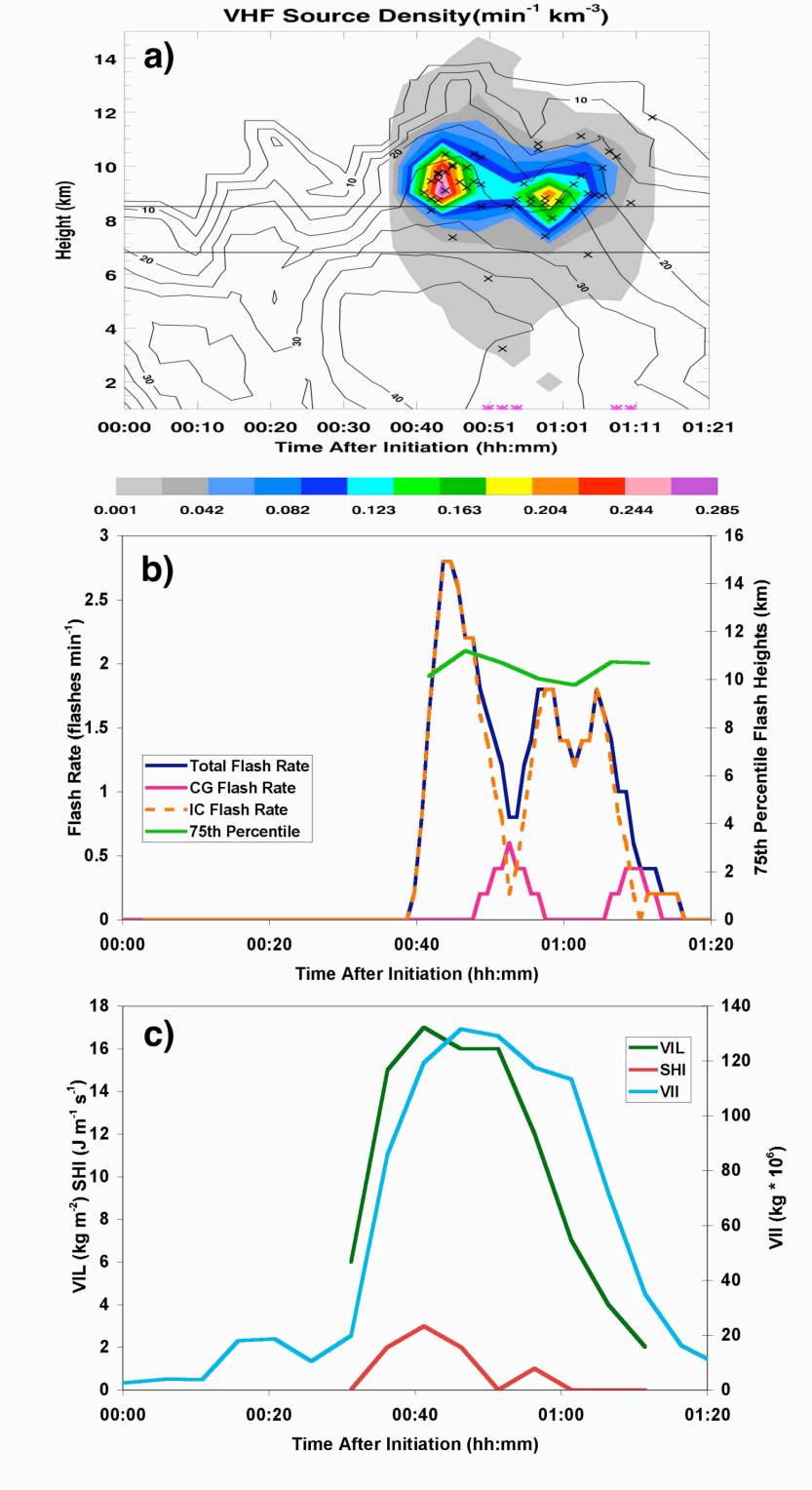

Fig. 29. Same as Fig. 20, but for case 10.

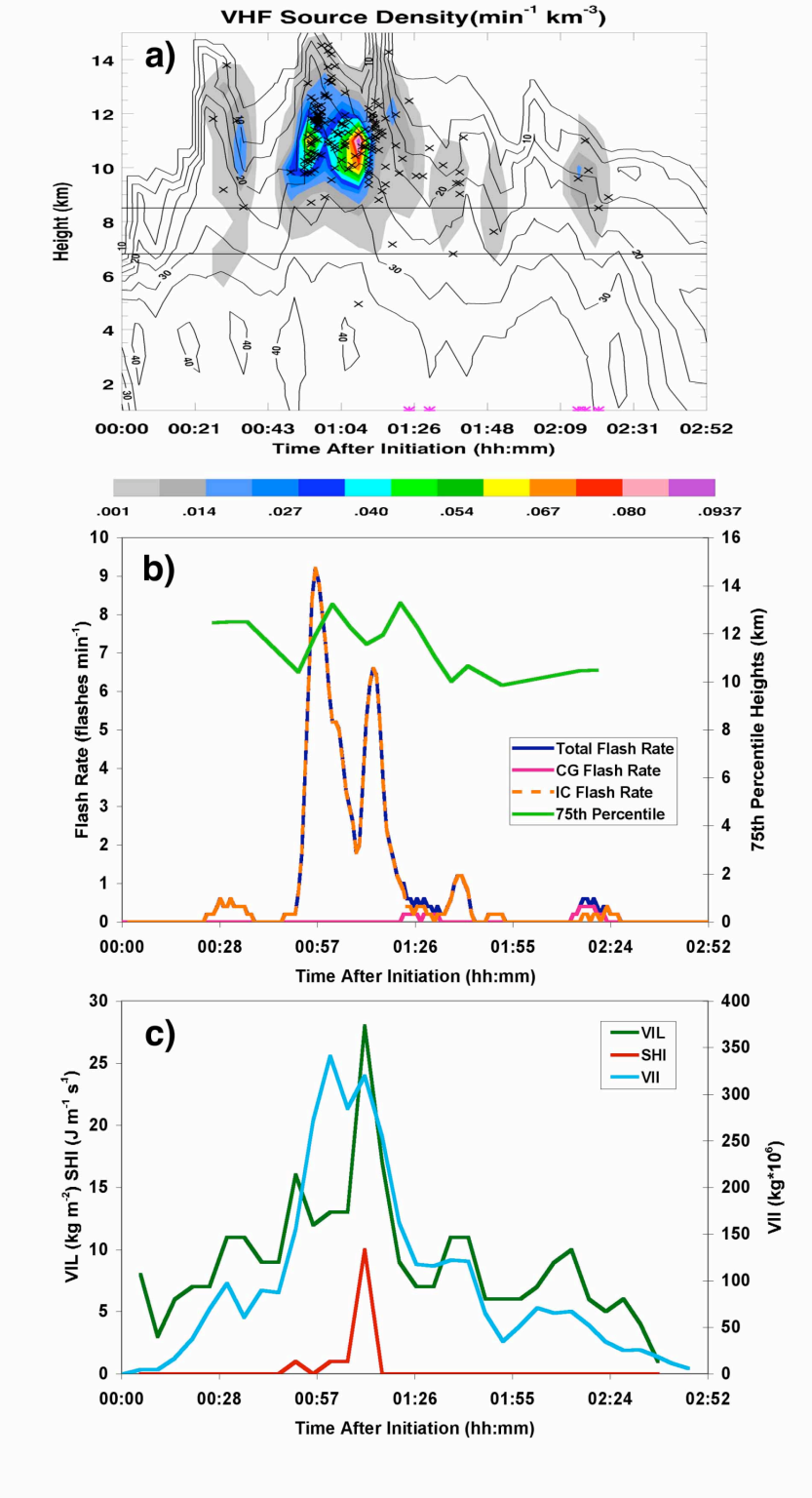

Fig. 30. Same as Fig. 20, but for case 11.

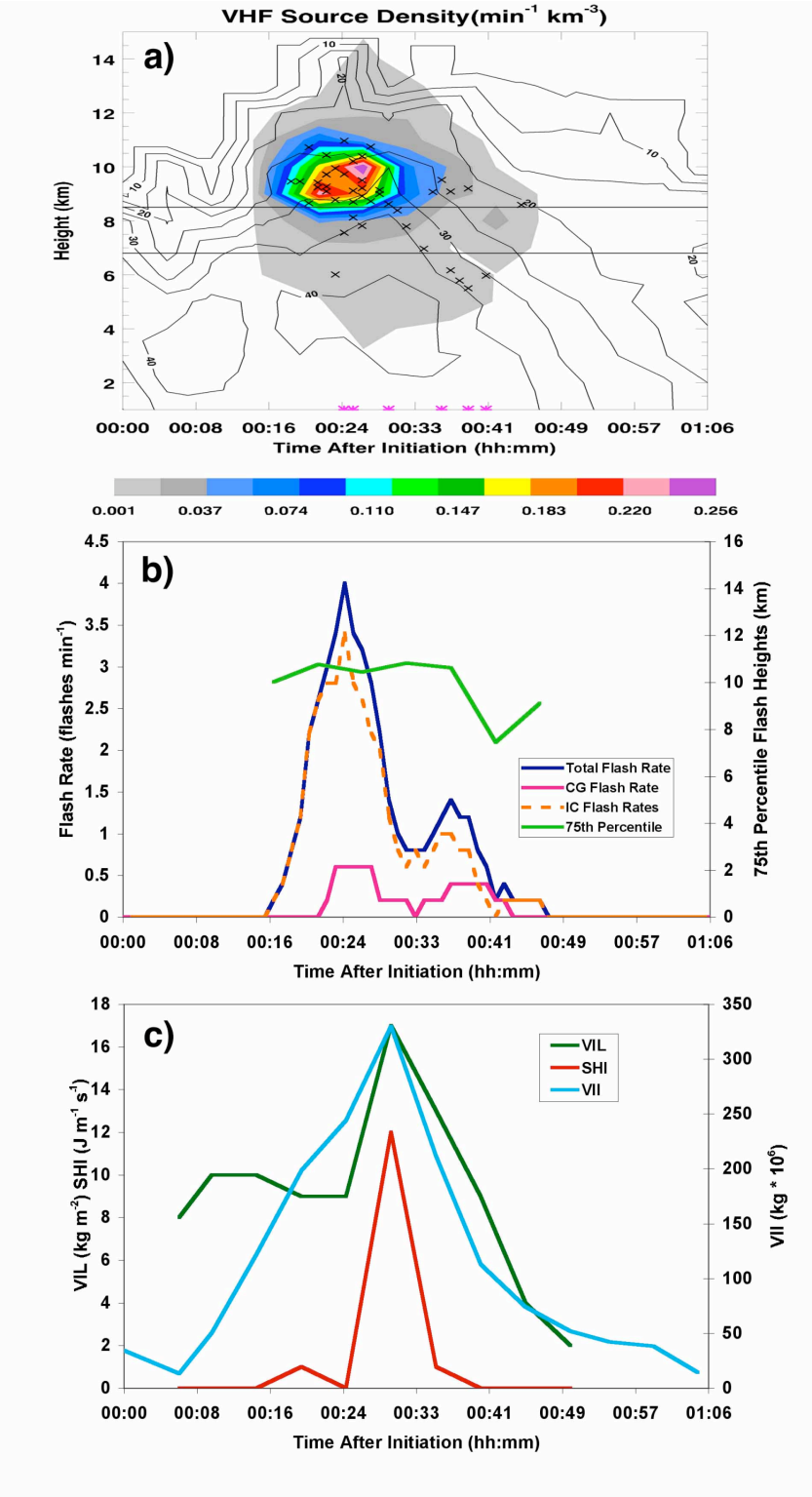

Fig. 31. Same as Fig. 20, but for case 12.

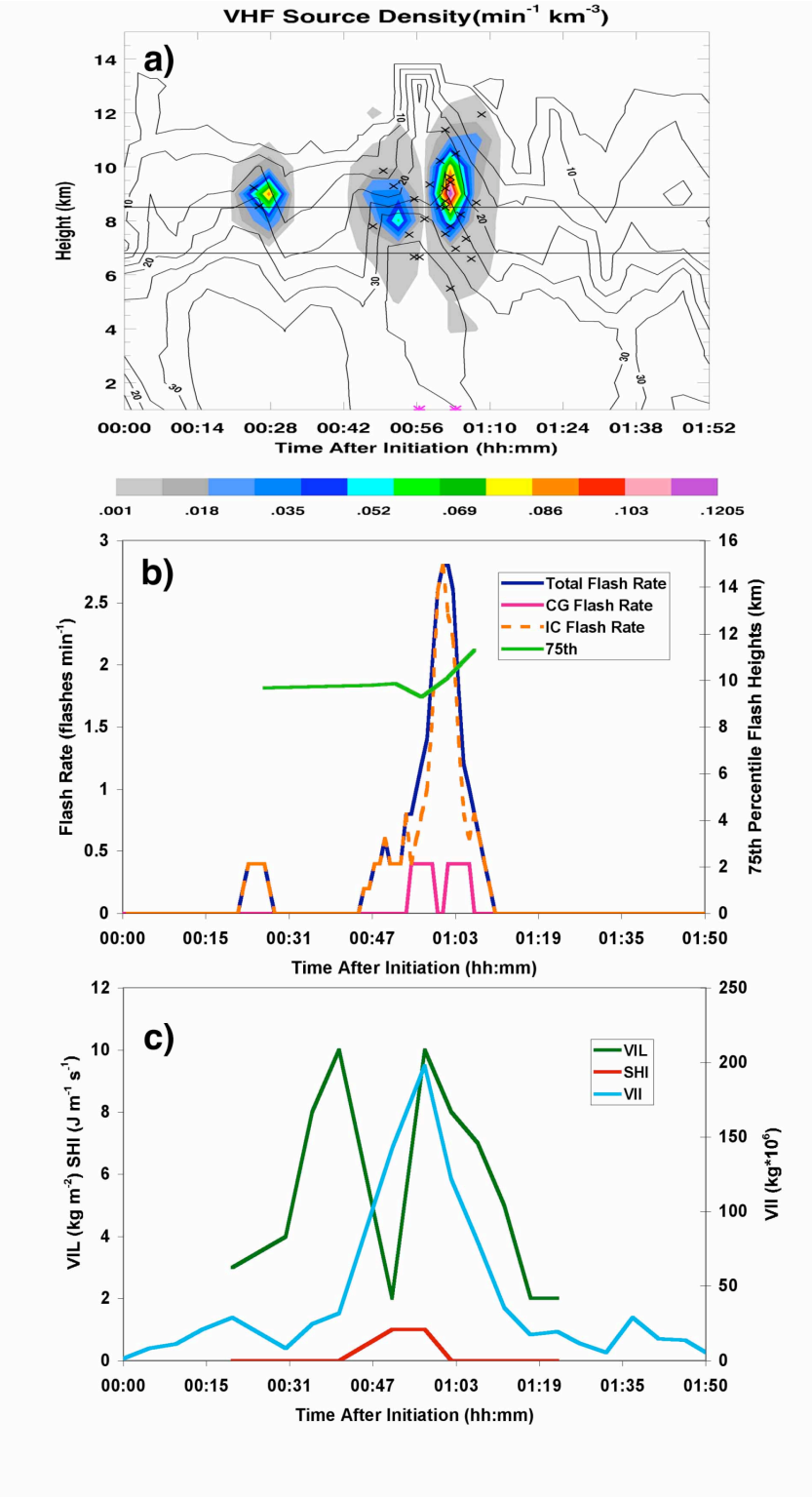

Fig. 32. Same as Fig. 20, but for case 13.

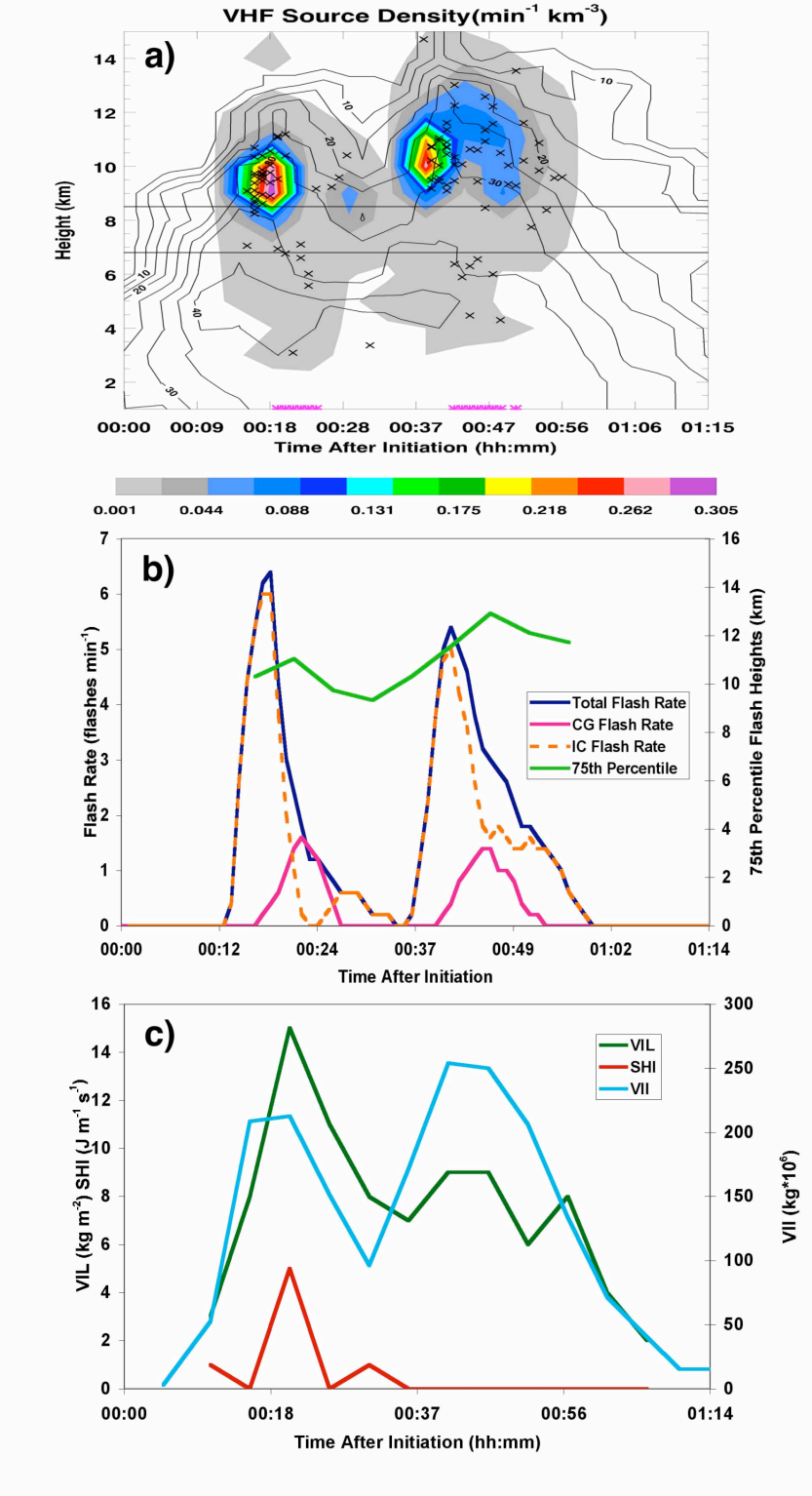

Fig. 33. Same as Fig. 20, but for case 14.

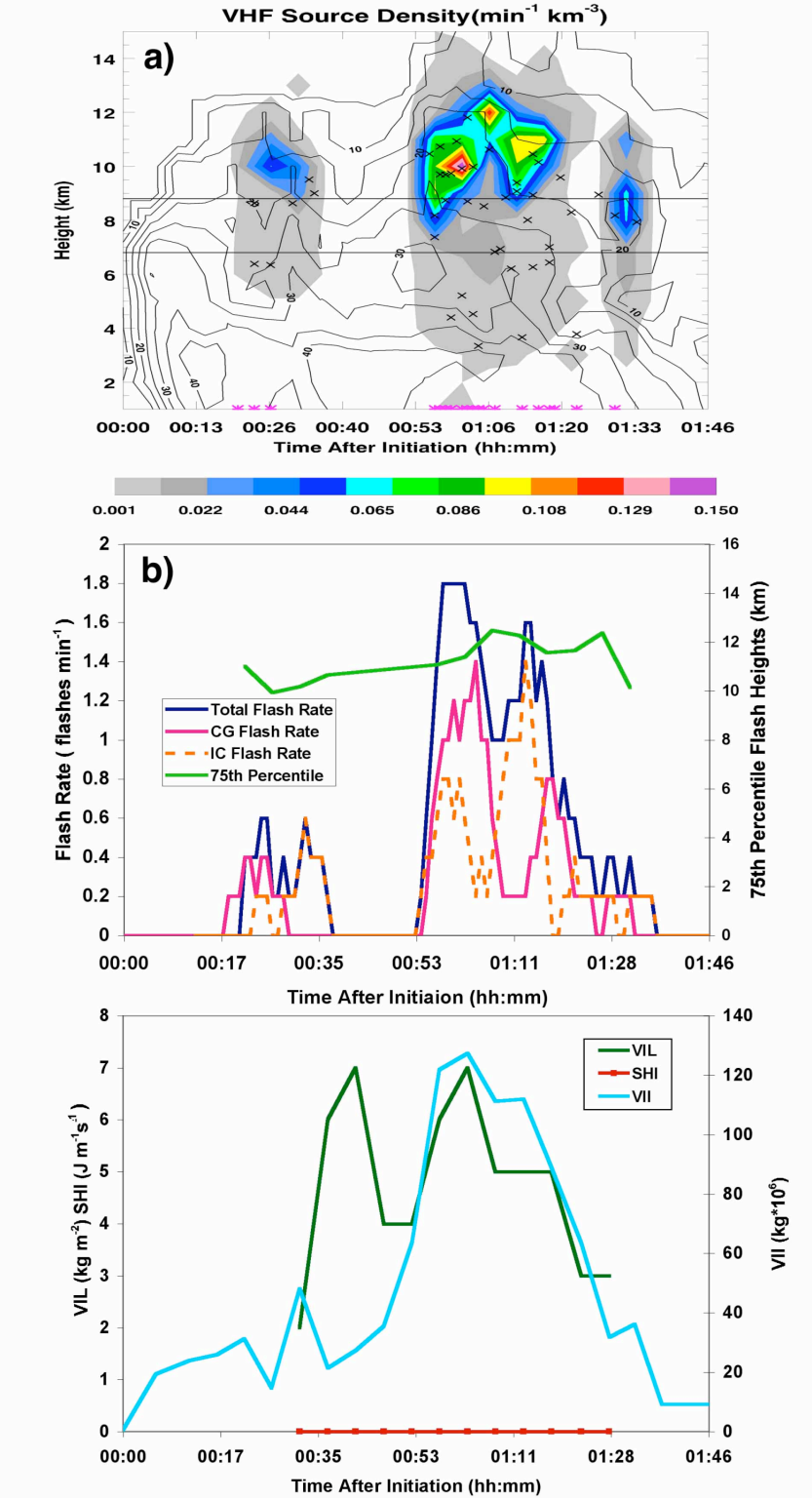

Fig. 34. Same as Fig. 20, but for case 15.

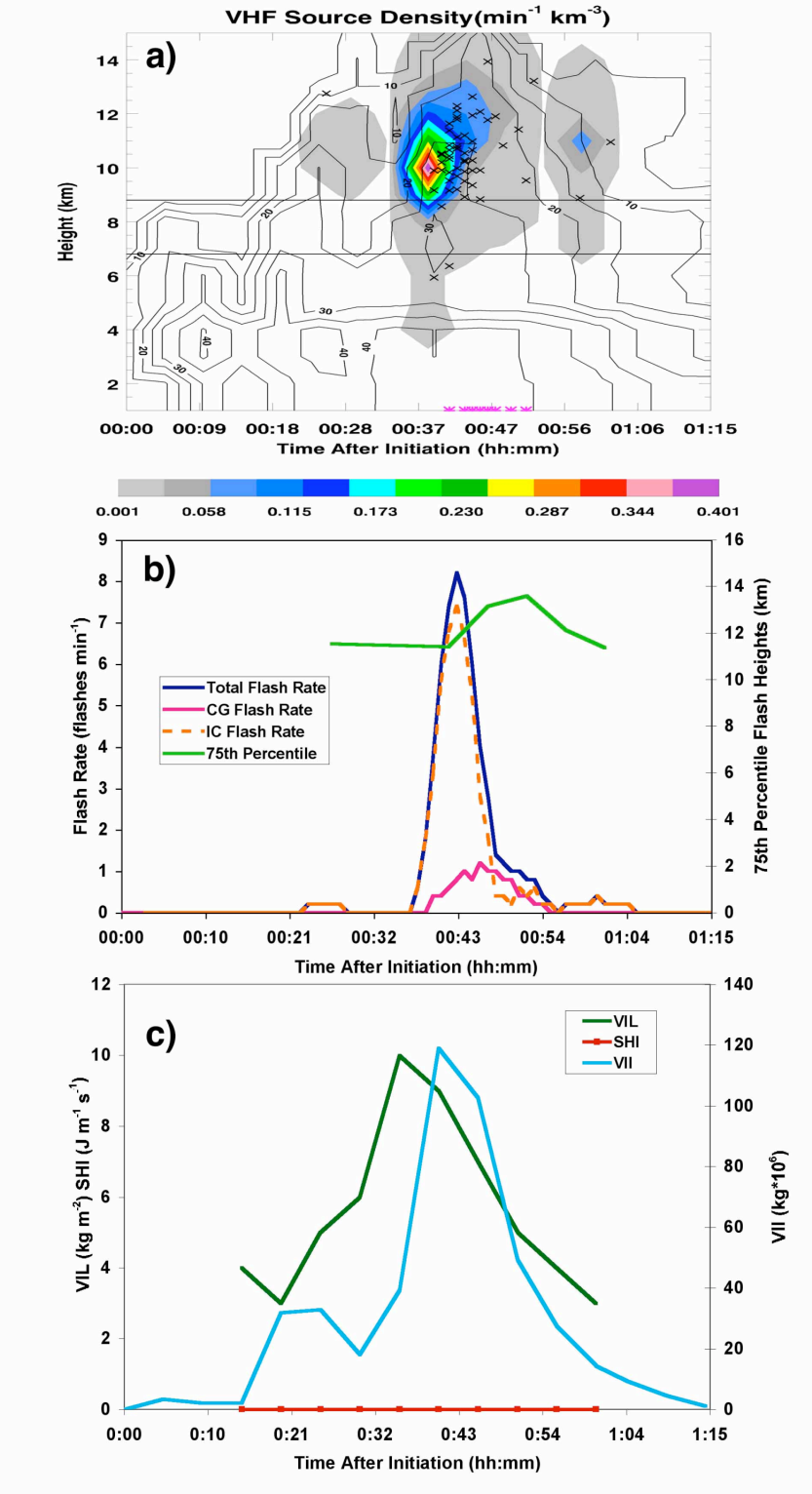

Fig. 35. Same as Fig. 20, but for case 16.

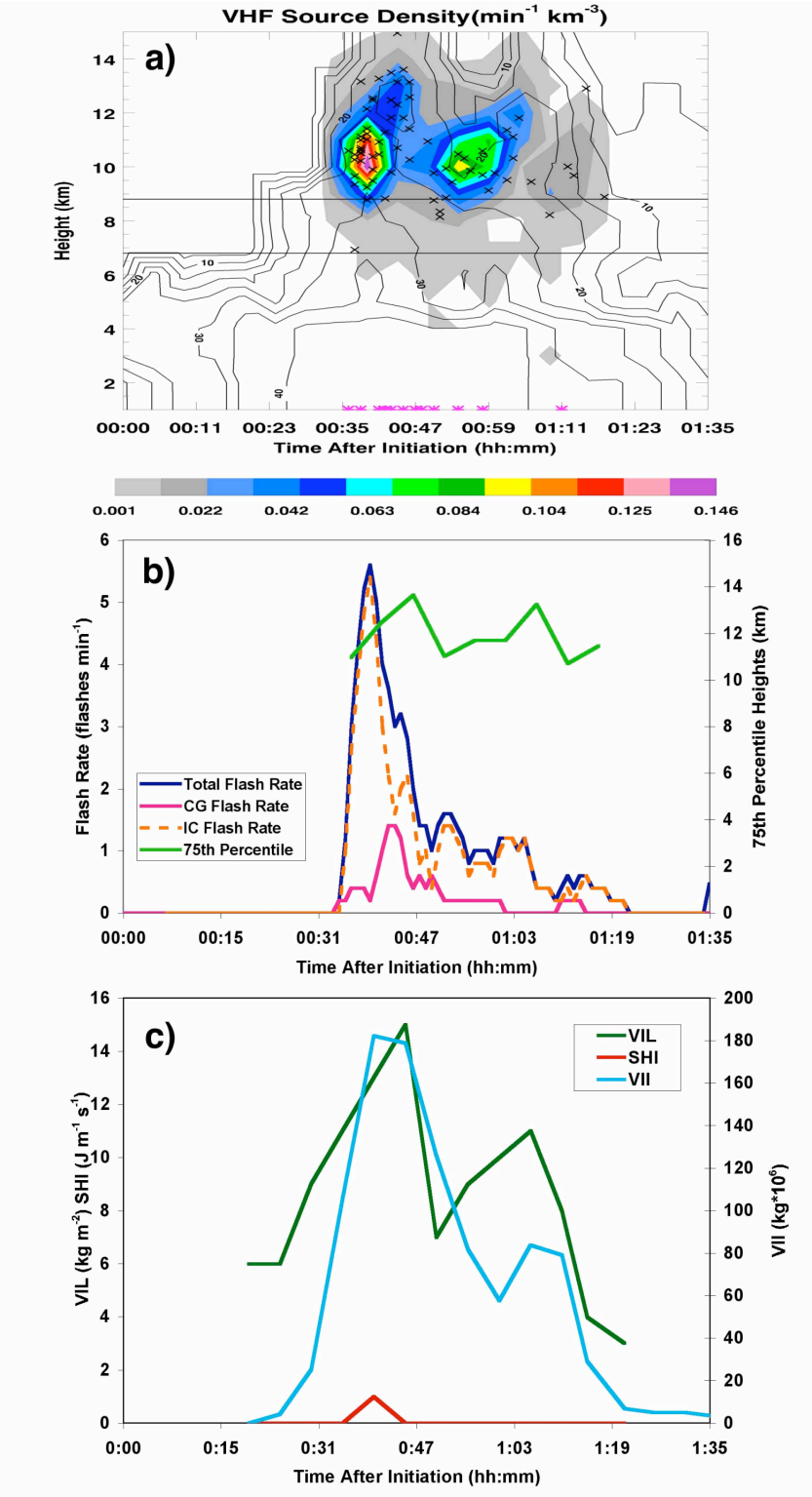

Fig. 36. Same as Fig. 20, but for case 17.

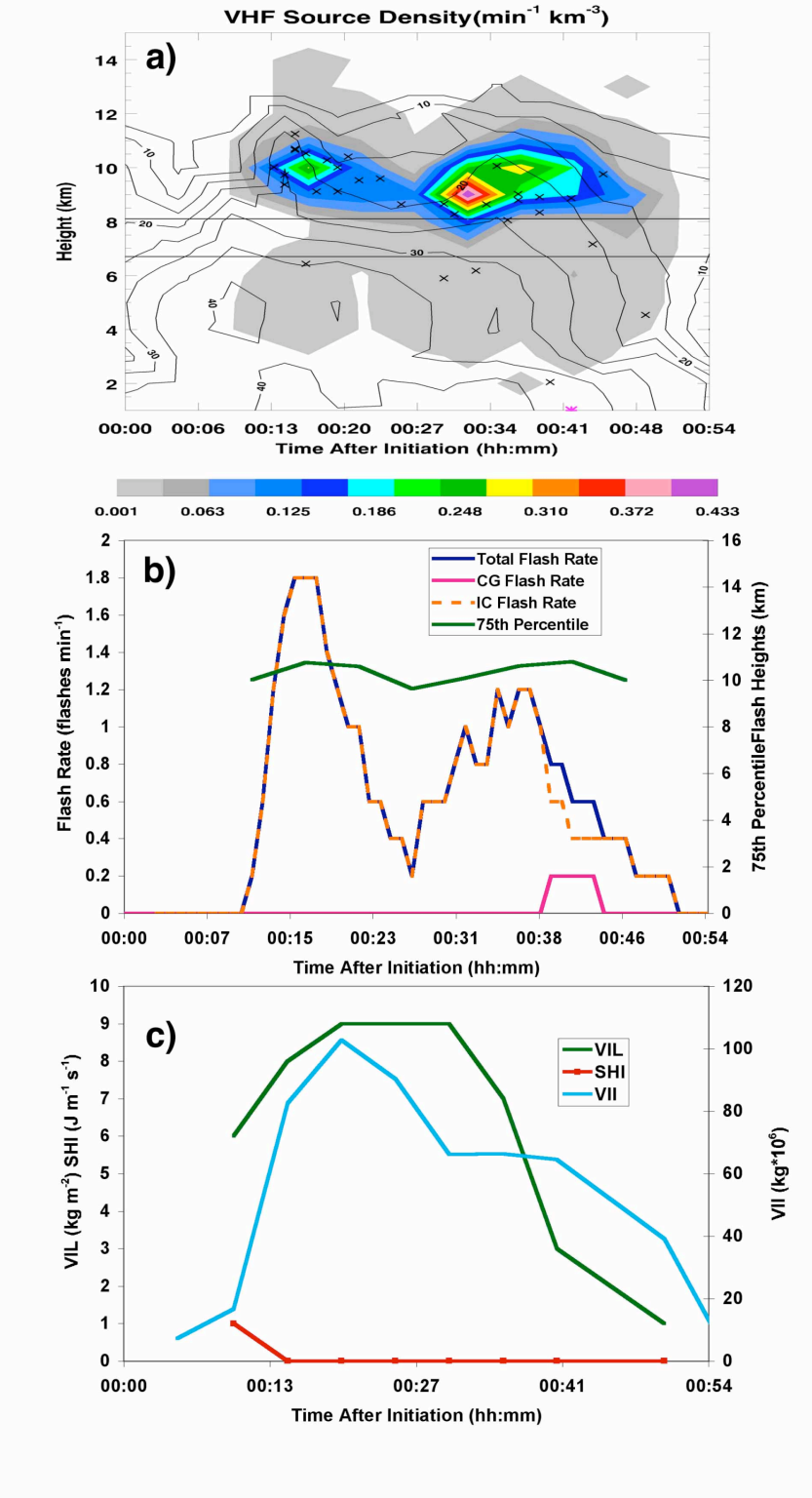

Fig. 37. Same as Fig. 20, but for case 18.

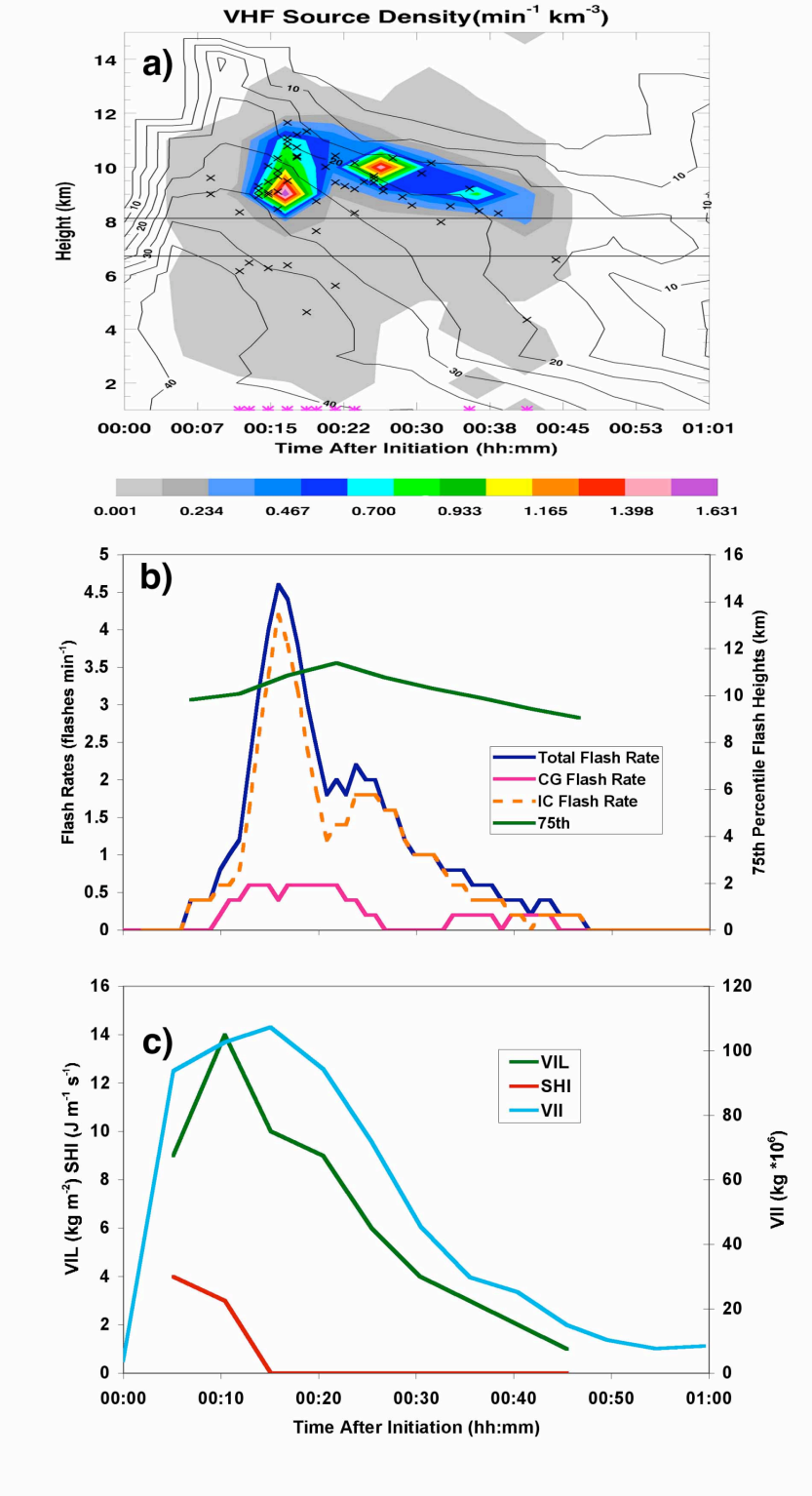

Fig. 38. Same as Fig. 20, but for case 19.

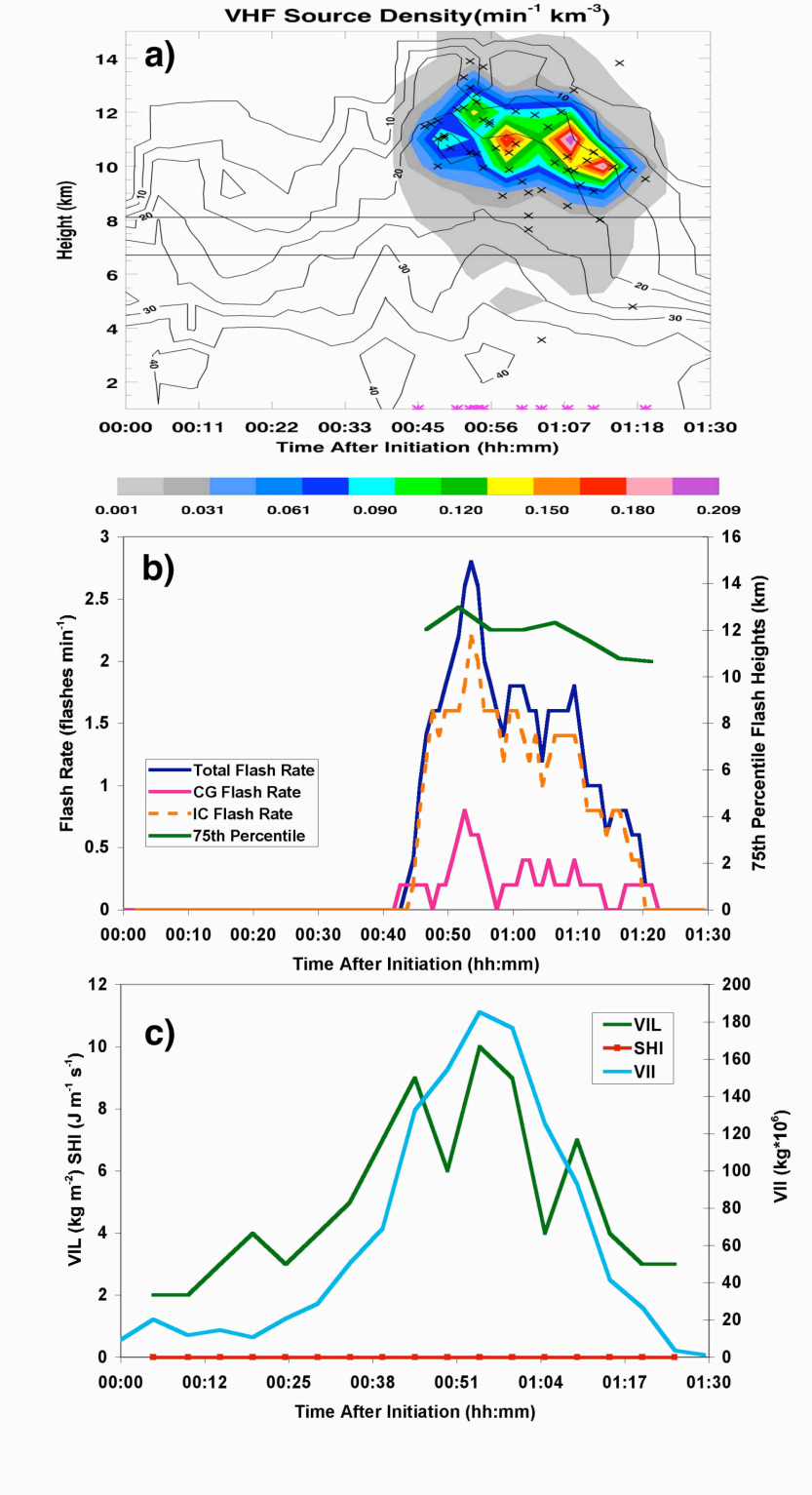

Figure 39. Same as Fig. 20, but for case 20.

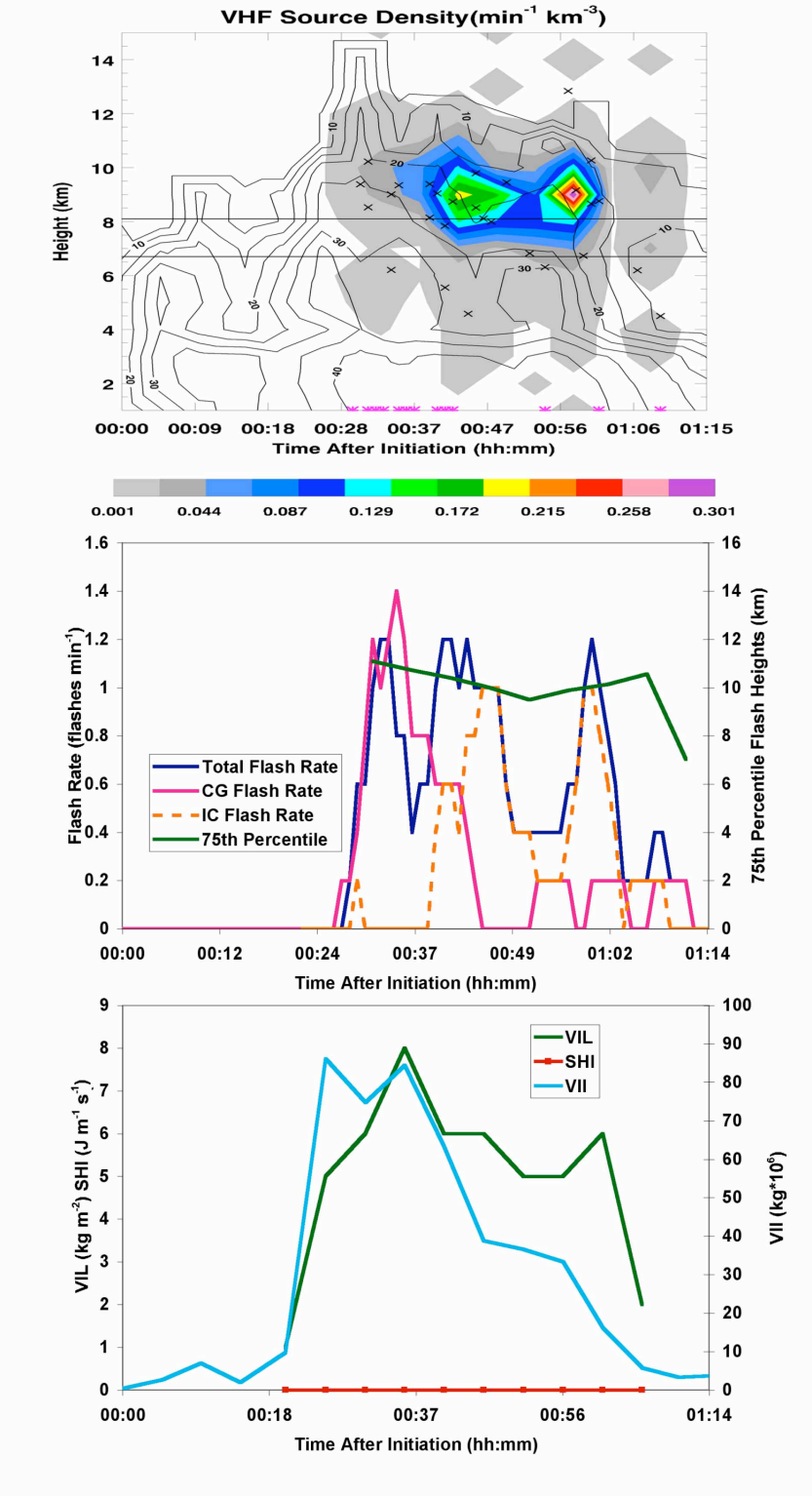

Figure 40. Same as Fig. 20, but for case 21.

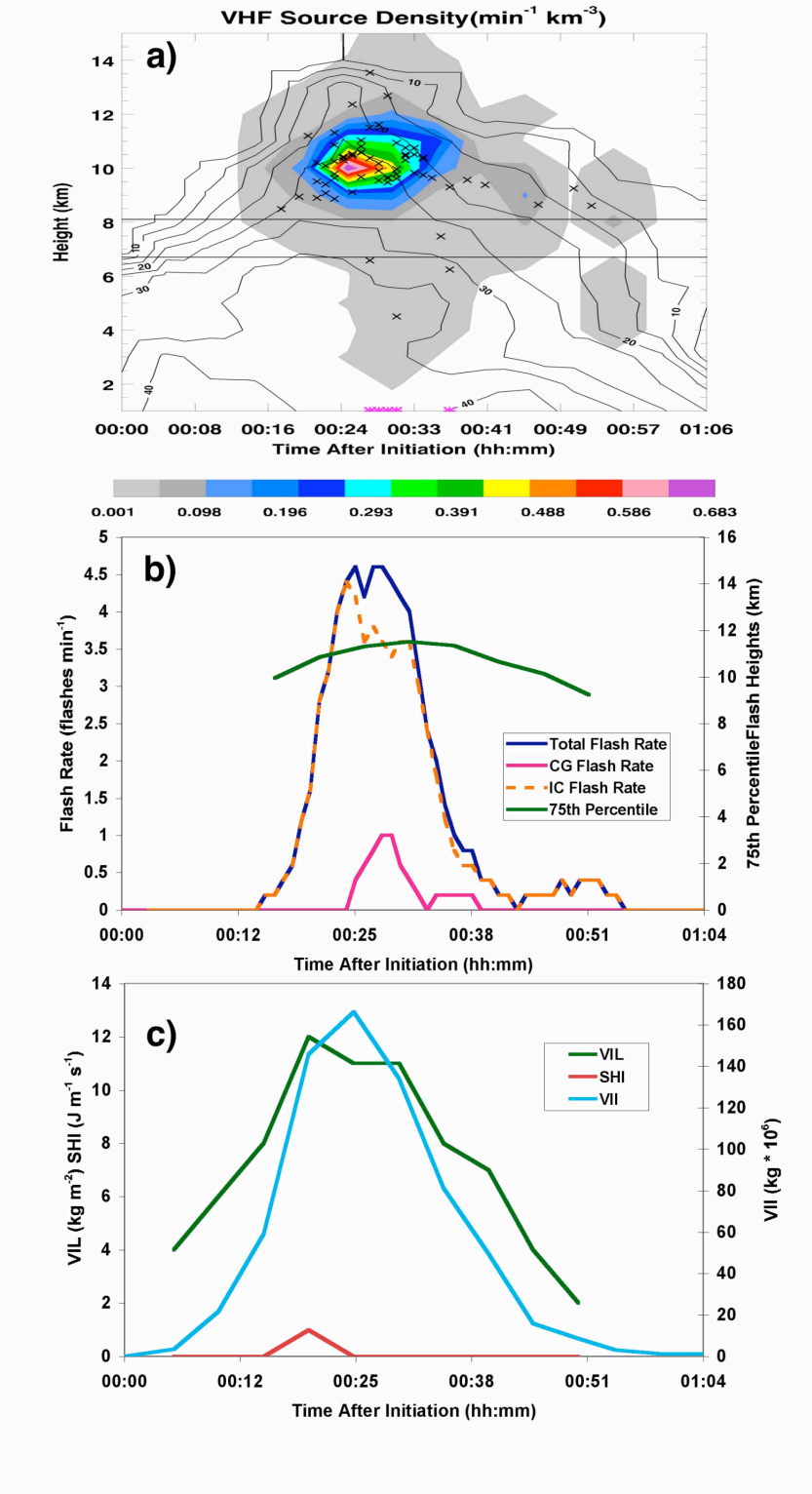

Figure 41. Same as Fig. 20, but for case 22.

different from the results of Steiger et al. (2005), which shows a much larger dynamic range in the flash heights with increased flash heights corresponding to increased cell intensity. The 75th percentile and median of flash heights displayed a slow rise to the maximum height during radar inferred peak intensity with a slow descent during the peak flash rate through the end of the cell's lifetime. The first and only CG with this cell occurred 22 minutes after the first IC flash at t = 53 min, which occurred during the descent of the height of the average 30 dBZ contour. This falls in line with the results from previous studies, which have also documented the descent of the main precipitation core prior to the onset of CG lightning activity (e.g. Goodman et al. 1988; Williams et al. 1989a; Carey and Rutledge 1996).

The second case occurring on this day displayed much higher flash rates with a maximum flash rate of 9 flashes min^{-1} occurring at t = 34 min. Fig. 21 shows the first flash occurring after a rapid increase in radar inferred cell intensity within the mixed phase zone (T< -10° C). The total flash rate increases dramatically after the average 30 dBZ contour rises above the -20° C isotherm with the first CG occurring only 2 minutes after the first VHF source is recorded. The IC flash rate during first 7 minutes of lightning activity (t=9 – t=16 min) remains below 1 flash min^{-1}, which is lower than expected when compared to past results (e.g. Williams et al. 1989a). The CG flash rate remains relatively constant during electrically active portion of the cell's lifetime with no significant relation between the radar inferred kinematics or microphysics noted. The total flash rate, on the other hand, experiences multiple peaks occurring at time t = 25, 34, and 51 min, which seem to slightly lag or coincide with peaks in SHI and VIL. The maximum flash rate of 9 flashes min^{-1} occurs during a period at which values of VIL, VII

and SHI are also at their maximum values. However, fewer VHF sources per flash seem to occur during this period as the first peak in flash rate (at t = 25) contains fewer flashes, but a higher VHF source density. The heights of the flashes do not appear to correspond well to the total or CG flash rates, however a slight lowering of heights is noted after the maximum total flash rate at t = 34 and a subsequent increase in heights at the time of the next peak in total flash rate at t = 51 min.

3.2.1.2 22 July 2005

Only one case was observed on this day. Case 3 contained the second highest flash rate and second highest VII value out of all the twenty-two storms examined (Fig. 22). Like case 2, this case displayed multiple peaks in the total flash rate with one occurring at t = 23 min and the other occurring at t = 33 min. The first flash occurred at t =16, just after significant intensification is noted with the average 30 dBZ contour rising well above the -20° C isotherm. The maximum flash rate occurred only eight minutes later with maximum values of SHI showing slight temporal lags in the maximum flash rates (similar to case 2) and maximum values of VIL and VII corresponding to the time of maximum flash rates as in past studies (e.g. Carey and Rutledge 2000; Watson et al. 2005). This case, unlike many others to be discussed, displays results similar to that of Steiger et al. (2005) with an obvious increase in both the flash heights (as shown in Fig. 22b) as well as the origin heights (depicted by the x's in 3.5a) just after the maximum flash rate of 20.4 flashes min^{-1} is reached. The maximum value of the 75^{th} percentile of flash heights occurs during a period of maximum storm height, as inferred by the height of the average 20 dBZ contour in Fig. 22a, with a decrease in the flash heights occurring

as the storm starts to weaken. The CG flash rate increases dramatically after the main precipitation core starts to descend with CG flash rates reaching 5.2 flashes min^{-1}. Although the average CG to total flash rate ratio for all 22 cases is 0.247, at time t = 28 min the IC/CG ratio decreases to 0.48 suggesting the majority of all flashes during this time period are occurring as CG flashes. This follows general model of lightning evolution seen in past studies with IC lightning dominating at the beginning stages of electrical development with a CG activity increasing after a descent in the main precipitation core is noted (Goodman et al. 1988; Williams et al. 1989a; Carey and Rutledge 1996). The total flash rate increases back to 10.8 flashes min^{-1} at t = 33 with a slight indication of an increase in cell intensity as shown by the increase in SHI and a plateau in VIL at this time. Flash heights, flash rates, and radar inferred cell intensity continue to decrease with the last flash occurring at t = 49 minutes.

3.2.1.3 5 August 2005

Four cases occurred on this day with the flash rates ranging from 1.8 flashes min^{-1} to the highest flash rate recorded from all 22 cases of 36.2 flashes min^{-1}.

Case 4 had the lowest flash rate of the Dallas group, with a maximum flash rate of 1.8 occurring at t = 49 min (Fig. 23). Interestingly, this is one of the few cases in which the VIL decreases during a time of increasing flash rates. However, the VII shows a relatively dramatic increase during this time from 12×10^6 kg to 35×10^6 kg. The first flash associated with case 4 occurred at t = 20 min with the first CG occurring seven minutes later. This case was one out of several cases that recorded CG to total flash rate ratios greater than 1.0. This means that the LDAR network recorded fewer than three

VHF source points with some of the CG flashes allowing for more CG than total flashes to be recorded. The implications and possible reasons for this occurrence will be discussed later. Despite potential errors in the LDAR network, this is one of the few cases in which several flashes originating below 6 km were observed. This might be due to the fact that this storm was relatively close to the LDAR network with an average distance of 27 km from the center of the network. This period of low level flashes also coincides with a period of high CG flash rates and, when combined with the observation of VHF source densities located below 2 km, suggests that many of the flashes originating at this level were CG flashes.

Case 5 (Fig. 24), like case 3, is one of the few cases that shows a large, steady increase in the flash heights. The flash origins appear to be increasing with height as the radar inferred cell intensity increases around time t = 38 min. This is also shown in the median, 75^{th} percentile, and 95^{th} percentile flash heights, which show an increase in heights of 3.1 km during the ten minute span from t = 32 min to t =42 min. The extra flash height information was placed on Fig. 24b to demonstrate the consistency in the variations of the various height parameters. For this reason the additional flash height information was not included on any other plots except for those demonstrating significant variation between the parameters (e.g. Fig 27). Since the VHF source density maximum tends to map out regions of positive charge, this case suggests that the main positive charge region increases in height from t=35 to t = 38 and then begins a slow descent. The point at which the positive charge region is at a maximum height corresponds to the maximum values in the 75^{th} percentile flash heights, which tends to lag the maximum total flash rate of 12.2 flashes min^{-1} at t = 36 min. During the time of

maximum flash rates, a rapid increase in the VIL, VII and, to a lesser extent, SHI is noted. These three parameters in Fig. 24c decrease as the flash rate begins to decrease at t = 38. As the cell continues to weaken just after t = 38 min, the flash origins begin to descend along the 10 dBZ average radar reflectivity contour. This close proximity of the flash origins to the 10 dBZ contour is noted in a few other cases, but not to the extent observed here. Also of interest is that the CG flash rate increases to a peak CG flash rate of 2.8 flashes min^{-1} with a total flash rate of 3.0 flashes min^{-1} at time t = 43. This gives an IC/CG flash ratio of 0.14 suggesting most flashes at this time were CG flashes. This is similar to case 3, in that the peak in the CG flash rate is followed by a sudden decrease in the CG flash rate followed by a minor increase in the IC rate. The decrease (increase) of the CG (IC) flash rate during this period also corresponds to a brief pause in the decrease of VII. This may suggest a brief increase in cell intensity occurred during this period.

Case 6 (Fig. 25) had the shortest lifespan out of all 22 cases. Nevertheless, it still managed to produce a total of 22 LDAR detected flashes with only one NLDN detected CG. This particular cell increased to it maximum intensity very quickly, therefore the maximum VII of 71.45×10^6 kg occurred during the first WSR-88D scan at t = 5 min. Like many other cases, the time of maximum VII corresponded to the time of the maximum flash rate. The one and only CG in this case occurred at time t = 6 min, which appears to occur just after the peak radar reflectivity core starts to descend. The flash origins seem to show a steady decrease in height from the first flash to the last, with flash heights and the average 20 dBZ contour decreasing as flash rates decrease.

The highest total flash rate observed in our 22 cases occurred in case 7 (Fig. 26). The first of the 613 flashes associated with case 7 occurred at t = 23 min. This was the

only flash that occurred before the first CG at t =25 min. Interestingly, 6 minutes before the first flash occurred, the storm had a VII value of 63.46 × 10^6 kg – a value that is associated with lightning in a few other cases (e.g. case 4 and 6 in Dallas) – yet no lightning was observed in this case until the VII surpassed 103.96 × 10^6 kg. However, a sudden increase in the SHI, VII, and VIL values at t = 25 min corresponds to an increase in the total flash rate from 2.2 flashes min^{-1} at t = 20 to 10.6 flashes min^{-1} at t = 25 min. The heights of the flash origins show very wide scatter, with the general trend in flash heights showing a slow ascent during the lifetime of the storm. Although the CG flash rate is great than other cases examined at the point, it does follow the trend of earlier cases mentioned with a peak in the CG flash rate occurring after a descent in the main precipitation core as seen in a lowering of the 30 dBZ contour. The maximum CG flash rate also lags just behind the time of the maximum IC flash rate with a time between the two maxima of 5 minutes.

3.2.1.4 6 August 2005

Two cases, cases 8 and 9 (Figs. 27 and 28, respectively), were observed on this day with case 8 developing within 9 km from the center of the LDAR network. This is a particularly interesting case since it, like case number 4, shows several flash origins below 6 km. The close proximity of this case to the LDAR network may explain the bimodal distribution of flash heights and VHF source densities, with the lower peak located around the 5.75 km level; a level at which most other cases display a lack of VHF sources. With the small distance between case 8 and the LDAR network, the ability for lower power source densities to reach the LDAR network increases (Steiger 2005).

Judging by the location of the flash origins in relation to the maxima in VHF source densities around the 5.5 km level suggests that the flashes started between the main negative and a lower positive charge region and propagated toward the lower positive charge region. This may imply that many of the flashes occurring in this region are CG flashes, especially when the total to IC/CG flash ratio becomes 0.0 after t = 28. A ratio of 0.0 is maintained until t = 35 at which point both flash rates fall below 1 flash min^{-1}. The bimodal distribution in heights appears to partially explain the decrease in 75^{th} percentile flash heights at t = 27, at which point flashes in the lower mode dominated and the CG flash rate peaked. The median flash heights show a significant decrease from 10.4 km at t= 12 minutes to 5.6 km at t =17 minutes. The 95^{th} percentile heights are included on this plot to show the contradiction between this case and the results of Steiger (2005), which shows significant correlations between flash heights and cell intensity. Given that the 95^{th} percentile heights increase during a time of decreasing cell intensity suggests that flash height information may become invalid for cases occurring within close proximity to the LDAR network. Also of interest is that only one IC flash occurred before the main precipitation core began to descend, which is shown by the decrease in height of the 30 dBZ contour at time t = 14 min. This was followed by the first CG at t=14 and an IC/GC ratio below 1.0 from t =14 to t=17 minutes.

The other case (case 9, Fig. 28) that developed on this day occurred an average of 59 km from the center of the network. Although the progression of the radar inferred cell intensity closely follows that of case 8 (with max values of VIL differing by 5 kg m^{-2}, max values of VII differing by 16×10^6 kg, and similar average radar reflectivity values), the bimodal distribution VHF source density is not as apparent in case 9. However, a

slight indication of a bimodal distribution in flash origin heights is evident from t = 23 min to t = 34 min with one mode clustered around the 10 km level and the other located at the 6.2 km level. Like case 8, this particular case shows the onset of all lightning activity occurring after a descent in the main precipitation core, which may help explain the high ratio of CG to IC flashes. In fact, the CG flash rate surpasses the total flash rate from t = 26 min to t = 30 min reaching the maximum CG flash rate of 7.2 at t = 28, which is the highest CG flash rate of all 22 cases. Peaks in VII, VIL and SHI all occur at the time of the maximum CG flash rate, rather than the time of the maximum total flash rate. A brief increase in the CG flash rate is also noted at t = 52 min during a period of descending flash heights.

3.2.2 Houston Cases

The remaining thirteen cases were observed in Houston with 5 cases occurring on 20 August 2005, 3 cases occurring on 25 August 2005, and 5 cases occurring on 13 September 2005.

3.2.2.1 20 August 2005

Case 10 was an interesting case in that no lightning activity was observed during a brief increase in cell intensity around t = 20 min (Fig. 29). This period shows the average 20 dBZ contour rising above the -20° C isotherm, however very low precipitation sized-ice concentrations appear to have been present for non-inductive charging, as values of VII and SHI remained close to zero during this period. As shown by the VII and SHI levels, once a sufficient amount of precipitation ice became available, the flash rate

increased to its maximum value of 2.8 flashes min^{-1} at t = 44 min. The first CG occurs 9 minutes after the first flash, with the CG flash rate reaching its maximum value as the precipitation core starts to descend and the flash heights begin to lower. However, at time t = 62 min, the flash heights reach their lowest value, but the CG flash rate falls to zero while the total flash rate increases from 0.8 flashes min^{-1} to 1.8 flashes min^{-1}. The magnitude of the change in flash heights, however, was relatively minor when compared with other cases.

Case 11 (Fig. 30), with a lifespan of 172 minutes, has a longer lifespan than any other case. Multiple fluctuations in the height of the average 20 dBZ contour, suggests this case experienced multiple mature stages as described by Byers and Braham (1949). For this reason, care must be taken when interpreting the time between the first flash and the first CG, which is 58 minutes. This issue will be dealt with in further detail within the discussion section. Out of the 157 IC flashes that occurred with case 11, only 5 CG flashes were recorded giving a storm total IC/CG flash ratio (i.e. the ratio of the total number of IC flashes to the total number of CG flashes) of 31.4. Table 6 shows this is the highest storm total IC/CG flash ratio out of all 22 storms examined. Peaks in all radar inferred intensity variables (SHI, VIL, VII, and the height of the average 25 dBZ contour) are highly correlated to peaks in the total flash rate. Local maxima in the flash heights appear to lag local maxima in total flash rates by approximately 6 minutes. From a radar perspective, case 11 is more intense than most cases examined with values of VIL exceeding 25 kg m^{-3}. However, as shown in previous cases maximum values in VIL did not correspond to maximum values in the total flash rate, while the maximum value of VII did. Comparisons between the flash heights and radar parameters suggest that

Table 6. The storm total IC/CG ratio (i.e. ratio between all IC flashes and all CG flashes for a given storm) for all 22 storms.

CASE #	IC/CG
1	29.0
2	10.8
3	2.7
4	1.3
5	3.7
6	21.0
7	3.7
8	0.9
9	0.1
DFW AVE	**8.1**
10	8.8
11	31.4
12	5.1
13	2.6
14	4.2
15	1.0
16	4.8
17	3.4
18	31.0
19	4.8
20	4.4
21	0.8
22	9.8
HOU Ave	**8.6**
ALL Ave	**8.4**

increased cell intensity leads to higher concentrations of precipitation ice available for charging at higher elevations within the storm. As with many other cases observed, the descent in the main precipitation core (as inferred by the descent of the average 30 dBZ contour) marks the onset of CG activity, with no CG activity occurring during times of ascending precipitation.

Case 12 (Fig. 31) is similar to the other cases already discussed as seen in the offset of the maximum total flash rate to the maximum radar inferred cell intensity. The flash heights remain nearly constant throughout much of the cell's lifetime with a descent as the cell weakens at t = 42 min. Again, the secondary peak in the total flash rate does not appear to be correlated to any changes in flash heights or radar inferred intensity variables.

Case 13 (Fig. 32), like case 11, appears to have undergone multiple mature phases (i.e. multiple cell lifecycles within WDSS-II identified reflectivity feature) with a cell lifespan of 112 minutes. Two IC flashes occurred after the first increase in cell intensity with the next IC flash occurring 22 minutes later as the cell reintensified. No CG flashes occurred with the first increase in cell intensity, leading to a large temporal gap of 32 minutes between the first flash and the first CG. The VIL increased to 10 kg m^{-3} twice during the life cycle of the storm, with the first occurrence corresponding to a flash rate of 0.5 flashes min^{-1} and the second occurrence corresponding to a flash rate of 2.8 flashes min^{-1}. Thus, rapid increases in radar inferred cell intensity do not necessarily correspond to increased flash rates unless the increase in cell intensity occurs within the mixed phase zone as represented by VII. The increase in VII corresponds to the increase in total flash

rate. The upper positive charge region, as inferred by maxima in VHF source densities, generally remains around 9 km.

Case 14 (Fig. 33) is interesting in that two distinct increases in cell intensity occur, which correspond to two distinct increases in the CG and total flash rates and VII. Also of interest is the fact that the second increase in cell intensity resulted in lower flash rates, but higher flash heights. This possibly suggests that ice generated from the first pulse in the storm was lofted to higher heights during the next pulse in the storm. This might have resulted in a larger amount of ice, which could explain the higher VII, but lower flash rates, during this time. The increase in flashes at higher altitudes could also be attributed to the weaker dielectric strength at higher altitudes (i.e. lower density) (MacGorman and Rust 1998). Also of interest is that the CG flashes only occur during times of descending precipitation cores as inferred by the average 30 dBZ reflectivity contour similar to earlier cases.

3.2.2.2 25 August 2005

Three cases (case 15, 16, and 17 found in Figs. 34, 35, and 36, respectively) occurred on this day, with each case falling in the same general area (Fig. 19). Case 15 developed at a distance of 62 km from the center of the LDAR network and displayed the first flash 3.5 minutes after the first NLDN detected CG. The next flash was also a CG, however both the LDAR network and NLDN recorded flashes during this time suggesting the LDAR recorded a portion of the flash. Although the first flash occurred as CG flashes, and occurred as the average 30 dBZ contour was descending, very little precipitation ice was present during this time as seen in the VII in Fig. 34c. Only 48×10^6

kg at t =32 during a period at which the flash rate was 0.4 flashes min^{-1}, similar to the low flash rates / low ice content observed in case 4. The VII drops during a period of no lightning activity, while the VIL increases, again suggesting VII out performs VIL as a proxy for total flash rate. As the VII increases, the total flash rate and CG flash rate increase, with a CG to total flash ratio between 0.66 and 1.0 from t = 77 minutes to t = 81 minutes. Given that the maximum flash rate of case 15 is 1.8 flashes min^{-1}, it becomes apparent that the lower flash rate storms often have a much higher CG to total flash ratios as documented in Rutledge et al. (1992).

Case 16 (Fig. 35) is similar to many of the previous cases discussed, though the maximum flash rate of 8.2 flashes per minute for this particular case is the highest out of all Houston cases. Like many of the higher flash rate cases previously mentioned, the flash heights of case 16 follow the trends of cases 3, 5, 9, and 14 showing minimal variation in the flash heights until just after a peak in the total flash rate occurs. This is evident in Fig. 35b for case 16 in which the 75^{th} percentile of flash heights show a minor descent from 11.5 km to 11.4 km from t = 27 min to t = 42 min followed by a rapid increase in flash heights to 13.2 km at t =47 min. This is also the time at which the CG flash rate increases to its maximum value of 1.2 flashes min^{-1}. Figure 35c again shows similar temporal evolution in both the magnitude and the total flash rate with the maximum value in VII of 119×10^6 kg occurring only three minutes prior to the maximum total flash rate.

Case 17 (Fig. 36) occurred at an average distance of 97 km from the center of the LDAR network, which is the furthest among all 22 cases. Although some cases did record CG flashes prior to LDAR detected flashes, this was the only case in which the

first LDAR detected flash was also the first NLDN detected CG. This was inferred by the fact that 3 VHF sources occur less than 0.1 second before the first NLDN detected CG, with no detectable lightning activity (from NLDN or LDAR) for 31 seconds after the initial activity. Also of interest is that the CGs that were registered during this time, occurred as the height of the main precipitation core was ascending. However, the CG flash rate does increase at t = 41 min as the main precipitation core starts to descend. Again, the temporal evolution in the magnitude of VII closely follows that of the total flash rate with the VIL also following a similar trend, but the increase in VIL at t = 65 min does not correspond to a significant increase in total flash rate as has been seen in several of the previous cases. The flash heights also show similar trends to those of previous cases with the maximum in flash heights occurring 7 minutes after the maximum total flash rate.

3.2.2.3 13 September 2005

A total of 5 cases occurred on this day. Case 18 (Fig. 37) produced low total flash rates with a maximum total flash rate of only 1.8 flashes min^{-1}. As previously mentioned, our data show similar results to past studies (Rutledge et al. 1992) suggesting that lower flash rate storms typically display a higher CG to IC flash ratio. However, in this particular case, the CG to IC flash ratio is very low despite the low total flash rates. The fact that only one CG was recorded in this case is a little suspicious considering the number of flash origins located below the 6.5 km level. Since IC flashes typically form between the upper positive and main negative charge regions (Shao and Krehbiel 1996; Rakov and Uman 2003), it seems as though these low level flash origins may actually be

CG flashes that were missed by the NLDN network. Despite the potential for missed flash information, this case follows the general trend of the 22 cases examined with the temporal evolution in the total flash rate is best represented by the VII rather than VIL. This can be seen in Fig. 37c, which shows the VIL increasing to its maximum value of 9 kg m^{-3} during a period at which the flash rate lowers to a relative minima of 0.2 flashes min^{-1} whereas the VII increases to its maximum value of 103 $\times$ 10^6 kg at the time of the maximum flash rate. The flash heights also follow the trends of the aforementioned cases.

Case 19 (Fig. 38) shows a rapid increase to radar inferred peak intensity at t = 10 min, as shown in the height and magnitude of the average radar reflectivity contours and VIL. The first IC flashes occur three minutes before the first CG flashes, which coincide with a very slight descent in the average 30 dBZ contour and a noticeable descent in the average 40 dBZ contour. As the peak flash rate of 4.6 flashes min^{-1} is reached at t = 16 min a bimodal distribution in flash origins is noted with the upper mode located around the 9 to 11 km level and the lower mode located around the 6 km level. Again, this may be due to the close proximity of case 19 to the center of the LDAR network, with an average distance of 8 km. Of particular interest in this case is the increase in the upper positive charge region as inferred by the ascent in the VHF source densities from t =14 to t=18, which slightly lags peaks in total flash rate, VIL and VII. This time lag could be due to the slight delay that occurs between the time at which large amounts of ice are lofted into upper portions of the storm and the onset of sufficient charging for electrical breakdown to occur. The initial peak in VHF source density is followed by an obvious descent of the upper positive charge region after t = 21 min as inferred by the descent in

the VHF source densities from t = 21 min to t = 42 min. This descent is also well depicted in Fig. 38b as the flash heights show a gradual descent during this period.

Case 20 (Fig. 39) was one of the three cases (15, 20, 21 represented by Figs. 34, 39, and 40, respectively) in which a CG was recorded prior to the first LDAR detected flash. Since this particular cell was located an average of 74 km away from the center of the LDAR network, it is possible that the large distance attributed to the lack of VHF sources associated with the first CG. Trends in the VII and VIL follow trends in the total flash rate with the max flash rate of 2.8 flashes min^{-1} occurring one minute prior to the maximum value in VII and VIL of 185.55 $\times 10^6$ kg and 10 kg m^{-3} respectively. As in case 19, case 20 also displays an obvious descent in the upper positive charge region as shown by the lowing of VHF source densities after t = 68 min. The flash heights also lower during this time period as shown in Fig. 39b, which may be associated with lowering charge layers.

Case 21 (Fig. 40) is yet another case in which the first CG occurs prior to the first LDAR detected flash, however this case is only falls at an average of 47 km away from the center of the LDAR network. Therefore, the lack of VHF sources with the first CG is not easily attributed to range effects as with the other two cases. Again, like many low flash rate cases, the CG to total flash rate ratio approaches or exceeds 1.0 throughout a portion of the cell's lifespan. Local increases to the maximum flash rate of 1.8 flashes min^{-1} occur at t = 34, 42 and 60 min. The VII also increase during t = 34 and 42 min to levels of 89 $\times 10^6$ kg and 84 $\times 10^6$ kg respectively, but drops to 16$\times 10^6$ kg at t = 61 during the last peak in total flash rate. This yet another case in which VII appears to perform slightly better than VIL in depicting peaks in total flash rate as two peaks in the

VII at t = 25 and t = 35 min slightly leading peaks in total flash rate whereas the VIL increases through this period. Based on previously discussed cases, the low correlation between VIL and total flash rate for this particular case is expected since VIL has been shown to perform very poorly as a proxy to total flash rate in low flash rate storms (e.g. cases 4, 13, and 15 represented by Figs. 23, 32, 34).

The last case, case 22, appears to be one of the best representative cases in the evolution of total lightning activity for ordinary convection as described by Williams et al. 1989a. This particular case produced a maximum flash rate of 4.6 flashes min^{-1}, with trends in the VII, VIL and SHI closely following the temporal evolution of the total flash rate. IC flashes dominate towards the beginning stages of electrical development with a noticeable increase in the CG flash rates occurring 10 minutes after the first IC flash and an IC/CG ratio dropping to 3.4 at time t = 30 min. Flash heights and the CG flash rate peak after the maximum value in total flash rate is reached, with the first CG flashes beginning only after the descent in the precipitation core is noted. The flash origins show a wide scatter during the maximum radar inferred cell intensity, with a gradual descent as the cell begins to weaken.

3.3 Integrated Results and Trends

Integrating the information from all 22 cases enables examination of trends that may not be exclusive to one particular event. For this reason, several of the aforementioned trends occurring within the individual cases listed above were examined for all twenty-two cases combined. For example, twenty-one out of the twenty two cases did not record a single VHF source prior to the average 30 dBZ contour reaching the

-10ºC isotherm. The one case that recorded VHF sources prior to the 30 dBZ contour passing the -10º C isotherm (cell 13) saw the 30 dBZ contour rise within 250 m (approximately the -8.2º C isotherm) -10º C isotherm before the first VHF source was recorded. Twenty-seven flashes were recorded after a subsequent increase in the cell intensity as the 30 dBZ contour surpassed the -10º C isotherm. The average time from cell initiation to the time at which the 30 dBZ contour to reached the -10º C isotherm was 14.23 minutes with a standard deviation of 13.00 minutes as shown in Table 7.

Although most cases did not record any VHF sources until the average 30 dBZ contour was located above the -10º C isotherm, VHF sources were recorded in all but one case (cell 1) after the average 30 dBZ contour dropped below the -10º C isotherm. VHF sources lasted for approximately 51% of the lifespan of each cell, with the last source, on average, occurring 18 minutes before the end of the cells' lifespan. However, it must be noted that cases 1, 11, 15, and 16 displayed temporal gaps in VHF sources beyond 18 minutes during the mature phase; therefore if the LDAR network does not record any VHF sources for 18 minutes and maximum reflectivity values greater than 25 dBZ exist within the cell (i.e. the cell is still "alive"), then the cell may continue to produce lightning.

Flash heights were highly variable as shown in the median, 95th percentile, and 75th percentile flash heights in Fig. 24. Due to the very close correlation between each height parameter, only the 75th percentile heights were plotted on the figures. Although the flash rates associated with the storms used in this study are relatively low when compared more complex convective modes (e.g. Steiger et al. 2005, Carey et al. 2005), the variability within the flash height information does not appear to significantly change

Table 7. The time (hh:mm) from cell initiation to the time at which the average 30 dBZ contour crosses the -10° C isotherm. Average and standard deviation for all 22 case are listed at bottom of table.

CASE #	INTN TO -10°C
1	0:27
2	0:11
3	0:09
4	0:05
5	0:11
6	0:02
7	0:07
8	0:00
9	0:14
10	0:34
11	0:14
12	0:00
13	0:47
14	0:06
15	0:00
16	0:14
17	0:30
18	0:10
19	0:02
20	0:35
21	0:22
22	0:13
AVERAGE	**0:14:14**
STDEV	**0:13:00**

as the max flash rates change. With the exception of cases 2, 20, and 21 the cases show maximum values in 75th percentile heights occurring after peaks in total flash rate. As each case enters into the dissipating stage (as inferred by radar reflectivity), the overall trend of 75th percentile flash is a slow descent as seen in all but 4 (11, 13, 17,18) cases. Generally, however, there is a fairly wide scatter for the heights of flash origins (depicted by an x on Figs. 20 to 41). The correlation between 75th percentile heights and total flash rates is very low, with an r^2 value of .17 for all 22 cases (Fig. 41).

Table 8 displays the times of first and last VHF source, NLDN detected CG flash, and radar reflectivity values larger than 20 dBZ for each of the 22 cells. The average time between the first and last 20 dBZ radar reflectivity contour (herein referred to as the cell "lifespan") was 82 minutes with a median lifespan of 76 minutes, which follows the findings of Byers and Braham (1949) for an airmass (i.e. ordinary) thunderstorm. However, a few of the cells had lifespans greater than 90 minutes suggesting the thunderstorm may have gone through multiple cell generations. Examination time height cross-sections of average radar reflectivity for cases 4, 10, 11, 13, and 14 show multiple peaks in radar inferred cell intensity suggesting multiple pulses in the main updraft occurred. This is in contrast to cases such as 2, 3, 7, and 22, which show a simple increase to peak radar inferred cell intensity with a subsequent collapse of the storm, suggesting the storm went through all three stages (cumulus, mature, dissipating) only once.

Cells displaying multiple peaks in radar inferred cell intensity were taken into consideration for comparisons in the time between the first VHF source and the first NLDN detected CG. Table 8 shows a mean time from the cell initiation to the first VHF

Table 8. Times of initiation (INTN), first VHF source (1st VHF), first NLDN detected CG (1st CG), and the times between cell initiation and the first VHF source (1st VHF – INTN), the time between the first CG and cell initiation (1st CG – INTN), and the time between the first CG and first VHF source (1st CG – 1st VHF) with negative times representing the cases in which the first CG occurred prior to the first VHF source (Note: negative times treated as a zero minute lead time (i.e. 00:00) in averages). All times are reported in hh:mm format with INTN, 1st VHF, and 1st CG reported in UTC. The average for all Dallas cases (DFW average), Houston cases (HOU average) and all cases combined (HOU and DFW average) are reported.

Cell #	INTN	1st VHF	1st CG	1st VHF - INTN	1st CG - INTN	1st CG - 1st VHF
1	13:01	13:32	13:54	0:31	0:53	0:22
2	14:22	14:33	14:35	0:11	0:13	0:02
3	20:21	20:37	20:43	0:16	0:22	0:06
4	17:30	17:50	17:57	0:20	0:27	0:07
5	17:45	18:03	18:10	0:18	0:25	0:07
6	19:50	19:54	20:00	0:04	0:10	0:06
7	19:55	20:18	20:20	0:23	0:25	0:02
8	22:08	22:21	22:22	0:13	0:14	0:01
9	19:09	19:31	19:33	0:22	0:24	0:02
DFW AVERAGE				**0:17**	**0:23**	**0:06**
10	15:47	16:29	16:38	0:42	0:51	0:09
11	12:39	13:06	14:04	0:27	1:25	0:58
12	20:02	20:21	20:27	0:19	0:25	0:06
13	15:11	15:36	16:08	0:25	0:57	0:32
14	20:37	20:53	20:57	0:16	0:20	0:04
15	20:46	21:10	21:07	0:24	0:21	-0:03
16	21:27	21:53	22:09	0:26	0:42	0:16
17	21:27	22:04	22:04	0:37	0:37	0:00
18	18:32	18:46	19:14	0:14	0:42	0:28
19	20:02	20:11	20:14	0:09	0:12	0:03
20	16:16	17:02	17:01	0:46	0:45	-0:01
21	20:27	20:58	20:57	0:31	0:30	-0:01
22	17:51	18:09	18:19	0:18	0:28	0:10
HOU AVERAGE				**0:25**	**0:38**	**0:12**
HOU AND DFW AVERAGE				**0:22**	**0:32**	**0:10**

source of 22 minutes for all cells, which varies slightly between Houston and Dallas cases. On average, the first NLDN detected CG occurs 12 minutes after the first VHF source for Houston cases, and 6 minutes for Dallas cases. However, the longer time span between the first VHF and CG for Houston cases is likely attributed to the two Houston cases with lifespans over 90 minutes. These two cases display radar reflectivity signatures suggesting that multiple main updrafts occurred throughout the lifespan of the storm, which is seen as multiple spikes in the height of the cell's radar reflectivity contours. If these two cases are excluded, then the time from first VHF source to first CG is reduced to 6 minutes for Houston. In every case, the onset of the first VHF sources is marked by a rapid increase in the intensity in the mixed phase region of the cell as inferred from radar reflectivity. During the peak intensity of the cells, the main positive charge region for 20 out of the 22 cases remained above the -20º C isotherm. The location of the main positive charge region, as inferred by the maximum VHF source density, shows a noticeable increase in heights during peak radar inferred cell intensity for cases 3, 4, 5,14, 15, 19, and 20 and an often more dramatic decrease in height after peak intensity for cases 3, 5, 6, 7, 8, 9, 10, 14, 15, 19, 20, and 22. This is further supported in the flash height information, which (with the exclusion of cases 6, 13 and 21 due to insufficient data) show the 75^{th} percentile of VHF flash source heights are maximized an average of 5.1 minutes (standard deviation of 4.5 minutes) after peak flash rates. Only three cases (cases 2, 3, and 20) show local maxima in flash heights prior to the maximum flash rate. This suggests that the upper positive charge region increases in height during times of maximum flash rates, which is consistent with the results of Krehbiel (1986). After the maximum intensity is reached, the flash heights tend to

descend. Since most IC flashes form between the main negative and upper positive charge layers, this shows strong support for decreasing charge regions as the cell weakens.

Although trends in the radar-inferred intensity appear to follow trends in the total flash rate, Fig. 42 shows that maximum values of radar reflectivity within the entire volume scan do not display strong correlations to the total flash rate. In addition, during the examination of time height cross-sections, it was mentioned that the onset of lightning occurred just after a significant increase in radar inferred cell intensity within the mixed phase zone. This "increase in intensity" was inferred by the increase in the slope (i.e. the increase in height with time) of the 20 dBZ or 30 dBZ contours within the mixed phase zone. However, the total flash rate did not appear to be correlated to the rate at which the radar reflectivity contours increased in height. Fig. 43 shows only 0.01% of the variance in the flash rate can be explained by the rate (km min^{-1}) at which the 20 dBZ contour crosses the -20° C isotherm to it's height at the time of maximum flash rate.

Since radar reflectivity is highly dependent on the size of the hydrometeors, and to a lesser extent the phase of the hydrometeors, it only partially captures the mechanisms responsible for charging via the non-inductive charging process. If, however, we utilize radar reflectivity values to hone in on the locations within the storm at which the noninductive ice-ice collisional processes dominate, (i.e. the mixed phase zone), then more concrete correlations may become evident. For this reason we examined the correlation between VII (eqn 14) and the total flash rate for all 22 cases. Scatter plots of the total flash rate (flashes min^{-1}) vs. vertically integrated ice (VII) (kg) multiplied by cell area and 10^{-6} for both Houston and Dallas cases are shown in Figure 44. Unlike the

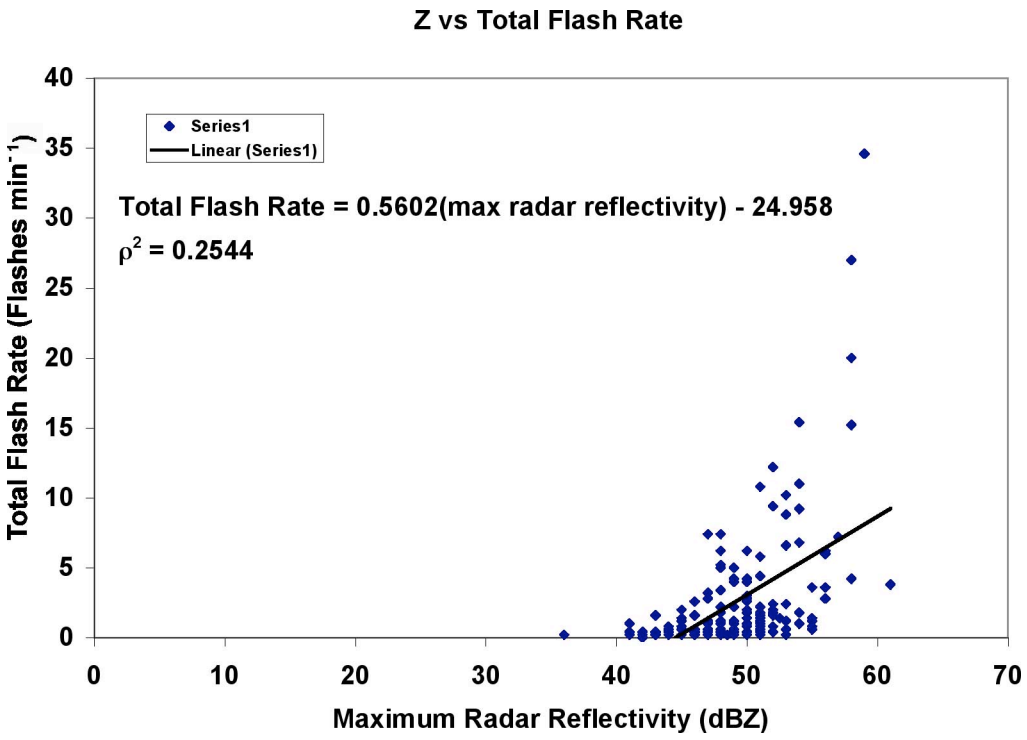

Fig. 42. The maximum radar reflectivity (dBZ) in a given volume scan versus total flash rate (flashes min^{-1}).

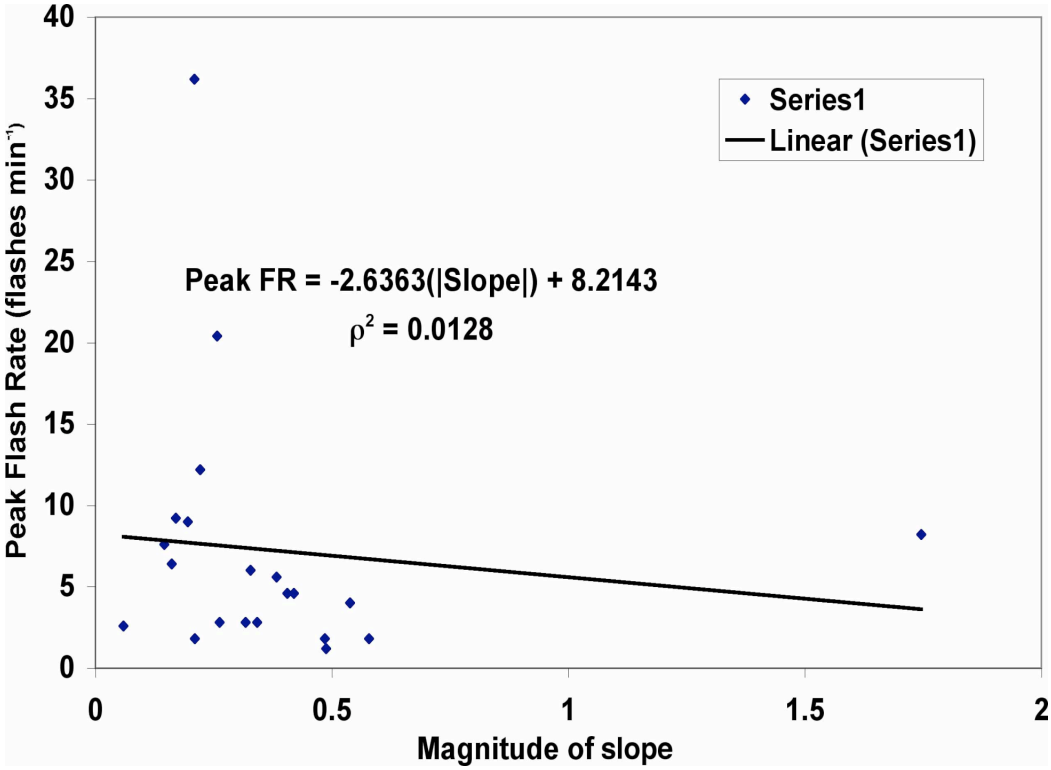

Fig. 43. Rate of ascent (km min^{-1}) of 20 dBZ contour from the point at which it crosses the -20° C contour to the time of peak flash rate.

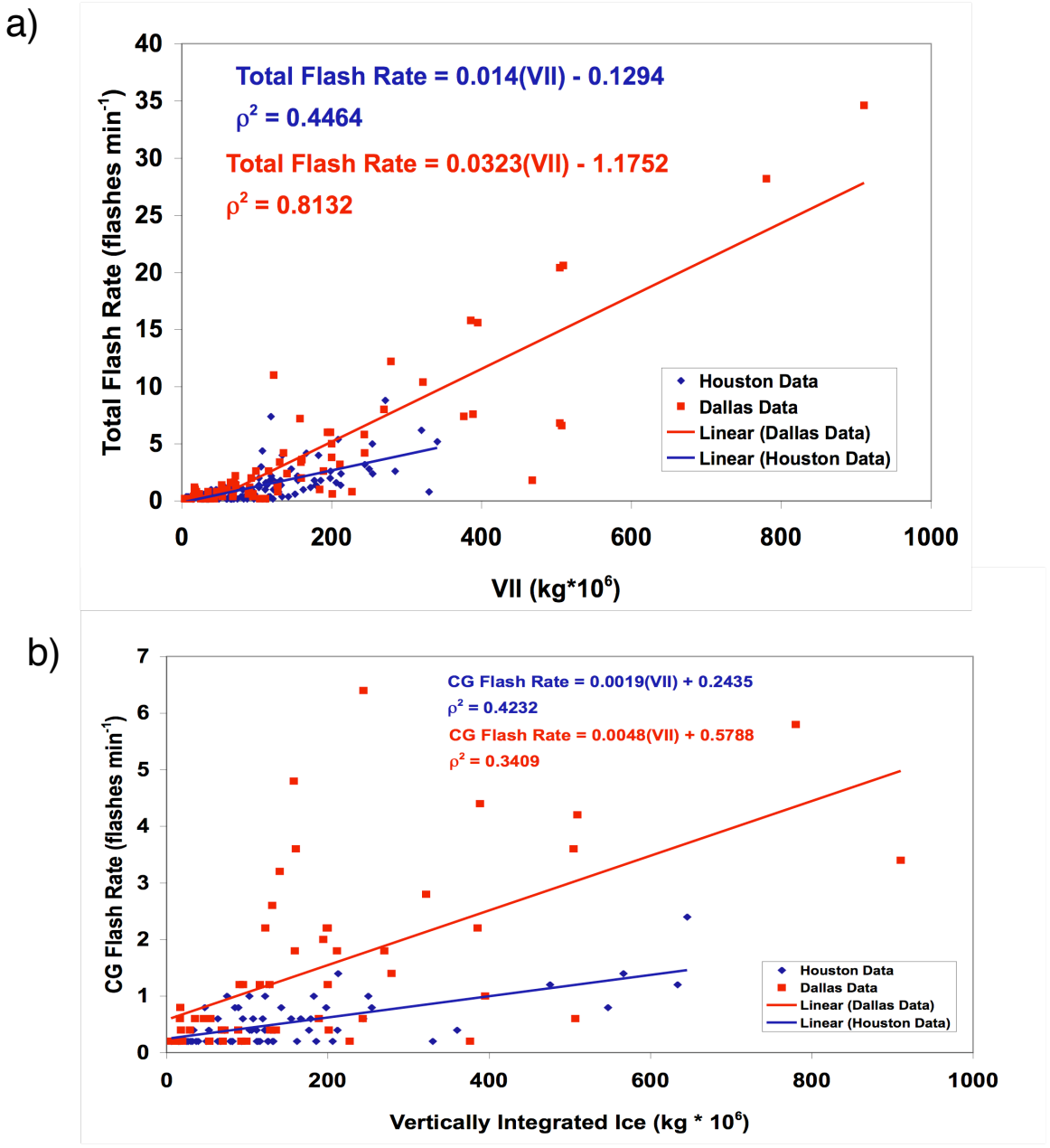

Fig. 44. a) Scatter plot of the total flash rate (flashes min^{-1}) vs. vertically integrated ice mass (kg) multiplied by cell area and 10^{-6} for both Dallas and Houston cases. Red points indicate individual data values for Dallas and blue points indicate individual data values for Houston. The red and blue lines represent the equation of best fit for Dallas and Houston data, respectfully. The R squared values are also displayed for both Dallas (red) and Houston (blue) showing strong correlations between the total flash rate and vertically integrated ice mass. This strong correlation is likely attributed to increase in charge that occurs with an increase in the ice available for non-inductive charging. b) Same as (a), but with CG flash rate for both Dallas (red points) and Houston (blue points).

correlations between other radar parameters shown, the r^2 values for both Houston and Dallas suggest that a significant amount (81% for Dallas and 45% for Houston) of the variance in the total flash rate can be explained by changes in VII. The differences in correlations between the two locations may be due to a number of factors, which will be further explored in the discussion section. However, differences in the slopes of the best-fit lines between Dallas and Houston suggest potential differences in the LDAR networks, radar calibrations, and/or storm microphysics, may exist between both locations. These issues are discussed in further detail within Appendix A.

Similar plots were created for the VII vs. CG flash rate in figure 44b. Again, different slopes between the two locations are likely attributed to the issues discussed in Appendix A. However, the scatter is much wider for the CG flash rates as compared to the total flash rates suggesting that VII serves as a much better source of proxy data for total rather than CG flash rates. Reasons for this weaker correlation will be discussed later.

4. DISCUSSION

The results from past studies examining correlations between three-dimensional lightning flash characteristics and convective intensity have shown promising results. (e.g. Ray et al. 1987; Coleman et al. 2003; Lang et al. 2004a,b; Carey et al. 2005; Wiens et al. 2005; Steiger et al. 2005). However, the three-dimensional flash characteristics of ordinary convective cells, which represent the most fundamental and ubiquitous thunderstorm type, have received relatively little recent attention. Our examination of 22 ordinary convective cells provides a more basic approach to the questions surrounding the relationship between total lightning and convective state. The microphysical and electrical characteristics for all cases will now be compared and discussed.

4.1. Comparisons to Conventional Model of Lightning and Cell Evolution

Past research has shown that the lightning development within convective cells follows a general trend with IC lightning dominating in the initial stages followed by an increase in CG activity as the cell weakens (e.g. Workman and Reynolds 1949; Lhermitte and Krehbiel 1979; Lhermitte and Williams 1985; Williams et al. 1989a; Goodman et al. 1988; Carey and Rutledge 1996). Our results from 18 out of a total of 22 cases show similar trends in the total lightning activity, with the first few flashes occurring as IC flashes with an average of 19 IC flashes occurring before the first CG. Peak IC flash rates typically occur during peak radar inferred intensity (e.g. maximum VIL, VII, or SHI), with maximum IC flash rates leading maximum CG flash rates by and average of 2 minutes (Table 9). Although IC lightning tends to dominate during the early stages of

Table 9. The times after initiation (h:mm) of maximum IC flash rates (max IC) and maximum CG flash rates (max CG). The time between the maximum IC and maximum CG flash rates are given showing most cases display maximum IC flash rates prior to maximum CG flash rates.

CASE #	MAX IC	MAX CG	MAX IC - MAX CG
1	0:54	0:51	-0:03
2	0:34	0:15	-0:19
3	0:23	0:25	0:02
4	0:49	0:51	0:02
5	0:36	0:43	0:07
6	0:06	0:08	0:02
7	0:43	0:48	0:05
8	0:20	0:24	0:04
9	0:23	0:28	0:05
10	0:45	0:53	0:08
11	0:57	1:24	0:27
12	0:25	0:24	-0:01
13	1:01	0:55	-0:06
14	0:19	0:23	0:04
15	1:13	1:04	-0:09
16	0:43	0:46	0:03
17	0:40	0:43	0:03
18	0:16	0:40	0:24
19	0:16	0:13	-0:03
20	0:54	0:53	-0:01
21	0:46	0:35	-0:11
22	0:25	0:29	0:04
		AVERAGE	**0:02**

vertical development, four of our cases reported CG flashes at or before the time of the first IC flash. Only one case, case 17, recorded a CG as the first flash. However, cases 15, 20, and 21 recorded CG flashes up to 3 minutes before the first VHF sources were observed.

The LDAR network's inability to detect any VHF sources associated with each CG flash for these particular cases could be due to a number of issues. Errors in the flash algorithm are discounted since the first VHF sources registered by the LDAR are also the first IC flashes as determined by the algorithm. Therefore, it appears as though the absence of VHF sources is associated with detection of the actual VHF sources. This could be due to the fact that all the CG flashes not detected by the LDAR network in these cases have low negative peak currents (< 10 kA). Therefore, the source powers could be too low for detection by the LDAR network. In addition, Mazur et al. (1997) points out that LDAR systems are unable to adequately map radiation sources that are associated with stepped and dart leaders propagating toward the ground. CG flashes also radiate VHF radiation at lower elevations than IC flashes; therefore, VHF radiation could have undergone multipath interference due to the local infrastructure. This appears even more likely when taking into consideration that cases 15, 20, and 21 fell at average distances of 62, 74, and 47 km from the center of the network, respectively. The average distance of all 22 cases from the center of the network is 55 km; therefore range effects were relatively high for these three cases. In addition, variable sensitivities in the network could also account for the lack of VHF radiation recorded with these particular flashes.

The inability of the LDAR network to capture the VHF radiation from CG flashes also occurred during the mature stages of a number of cells, most notably cases 4, 9, 14,

and 21 when the CG flash rates were higher than the total flash rates. Except for one CG flash occurring in case 9, all the CG flashes in cases 4, 9, 14, and 21 were negative; therefore, the CG rate most likely exceeds the total flash rate due to the aforementioned limitations of VHF source detection.

Despite the rare case in which CG flash rates exceed the IC flash rate, IC flashes tended to dominate over CG flashes with an average ratio between CG flashes to total flashes of 0.247 for all 22 cases. A few cases displayed noticeably lower IC/CG flash ratios (cases 4, 15, 18, and 21). This typically occurred within cells displaying low total flash rates (maximum flash rates below 2 flashes min^{-1}), a result which was also documented by Rutledge et al. (1992) (Fig. 45). They suggest a possible reason for the lower IC/CG ratio may be due to the transport of the upper positive charge region to lower regions of the storm. Stronger updrafts within storms displaying higher total flash rates tend to prevent the main positive charge from descending to lower levels, thereby limiting CG lightning and promoting IC lightning. Also noteworthy is the fact that the decrease in IC/CG flash ratios for the lower flash rate storms in our study are not only due to a decrease in the IC flash rate, but a higher than average CG flash rate when compared to other cells. Therefore, the results do seem to support the idea proposed by Rutledge et al. (1992) in which the lower positive charge region quickly develops due to the inability of stronger updrafts to sustain the ice at higher regions of the storm. Moreover, since dielectric strength influences the breakdown process (Williams et al. 1989b), the decrease in ice mass at higher levels of these lower flash rate storms (as inferred by average radar reflectivity in the mixed phase zone) may also play a role in the decreased IC activity.

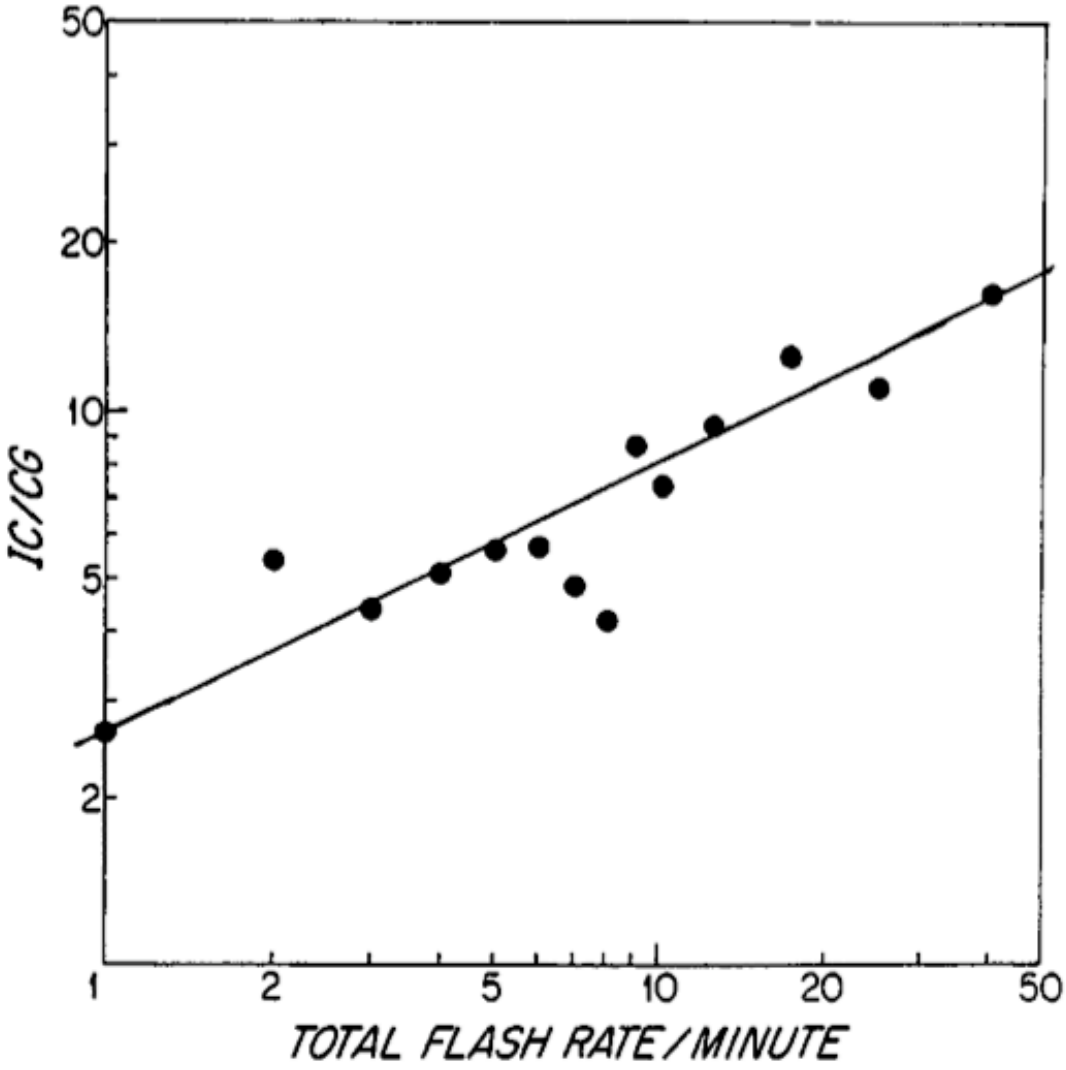

Fig 45. Plot of the IC/CG ratio as a function of the total flash rate showing the IC/CG ratio decreases for decreasing total flash rate. (From Rutledge et al. 1992)

The development of a lower positive charge region leading to CG lightning has been attributed to the mixed phase hydrometers falling below the charge reversal temperature. Lhermitte and Williams (1985), Goodman et al. (1988), Williams et al. (1989a) and Carey and Rutledge (1996) all noted a descent of the main precipitation core contours prior to the onset of the first CG activity. It is hypothesized that descent of the radar reflectivity core suggests large quantities of ice are descending at levels below the inferred height of the main negative charge region. This would, in turn, lead to the development of a lower positive charge region due to ice particles descending below the charge reversal temperature.

Upon the development of the lower positive charge region, enough charge may be generated between the main negative and lower positive charge regions to result in the breakdown process leading to CG lightning. Although several cases do show the peak CG flash rates occurring after the descent of the main reflectivity core (e.g. cases 3, 4, 5, 8, 9, 14, 16, 17, 18, 19, 22), there are those cases which do not display the same sequence of events (e.g. cases 2, 10, 12, 20, 21). A very interesting example is shown by case 14 in which the CG activity peaks after the first descent of the main precipitation core at t = 20 min after cell initiation, which is followed by a sudden end to CG activity the main precipitation core begins to reascend at t = 30 min and is again followed by an increase in CG activity once the precipitation core descends for the final time at t = 39 minutes. This strongly supports the idea that a descent in the precipitation core indicates the development of a lower positive charge region and the potential for an increase in CG lightning activity.

4.1.2 Bimodal Distributions in VHF Source Densities

As described in Rison et al. (1999), negative polarity breakdown is noisier than positive polarity breakdown at the radio frequencies used by the LDAR. Therefore, if the development of a lower positive charge layer is a significant contributor to the onset of CG activity as suggested by Williams (1989b), it seems logical that we should observe an increase in VHF source density at lower levels of the storm during times of CG activity. Many studies have documented the occurrence of a bimodal distribution of flash heights (e.g. MacGorman et al. 1981, Taylor 1984; Proctor 1991; Carey et al. 2005). The results from Taylor et al. (1984) show a bimodal distribution VHF sources heights with the upper (lower) mode located at the 12 km (4.5-6 km) level. Three of our cases, which fell within close proximity to the center of the LDAR network, show similar results. Cases 4, 8, and 19 (located an average distance of 27, 9, and 10 km, respectively, from the center of the LDAR network) each show a bimodal distribution in VHF source heights at later stages of convective development as the CG flash rate increases. The bimodal distribution is less obvious for case 19 due to the unusually high number of sources per flash (average of 77.5 sources flash^{-1}), which resulted in a bias towards the depiction of higher VHF source densities in Fig 39. Each of the inferred lower positive charge regions develop after a significant descent in the main (i.e. average 30 dBZ) reflectivity core occurs. This strongly supports the idea of a lower positive charge region developing as mixed phase hydrometers fall below the charge reversal temperature.

The absence of a bimodal distribution in VHF sources in other cases is most likely attributed to the larger distance at which the cases fall from their respective LDAR networks. Steiger (2005) points out that lower-level VHF sources occurring in storms

displaying a multimodal height distribution are weaker than sources associated with the upper-level. Similar results were shown by Thomas et al. (2001) in which larger source powers were detected in upper portions of the storm. Therefore, the weaker power amplitudes associated with lower-level sources may lead to decreased detection efficiency of the low-level peak in VHF sources as the distance from the storm to the LDAR network increases. This is especially apparent when comparing case 8 to case 9, which fell at average distances of 9 and 59 km from the center of the LDAR network, respectively. Although the progression of the radar inferred cell intensity of case 9 closely follows that of case 8 (with max values of VIL differing by 5 kg m^{-2}, max values of VII differing by 16×10^6 kg, and similar average radar reflectivity values), the bimodal distribution in flash origins and VHF source density is not as obvious for case 9. Due to the apparent reduced detection efficiency of lower power sources for lower heights, it is not possible to infer information regarding a lower positive charge region in every case. However, the results from these few cases strongly support the development of a lower positive charge layer coinciding with the onset of CG lightning.

4.1.3 Flash Heights

Although cases falling within close proximity to the LDAR network may provide additional VHF source information, the increase in VHF sources at lower levels leads to significant issues regarding the interpretation of flash height information. The development of the lower mode of flashes results in highly variable height information as seen in Fig 27b, which shows both the 75^{th} and 95^{th} percentile heights for case 8. At time t = 27 minutes the 75^{th} percentile heights drop to 6.1 km while the 95^{th} percentile heights

jump to 13.8 km, suggesting the potential exists for misinterpretation of flash height information of cases falling close to the LDAR network. This has significant implications for nowcasting storm intensity as described by Steiger et al. (2005), since misinterpretations could lead to inaccurate inferences of storm intensity. Therefore, future work exploring the utility of flash height information with respect to storm intensity may consider the implementation of a distance based weighting function to flash height information. Height information from storms occurring beyond a given distance threshold may yield more reliable information regarding storm intensity than others occurring within close proximity to the LDAR network.

Aside from distance issues associated with the flash height information, our results imply that the flash height information does not provide consistently reliable information of storm intensity or total flash characteristics. Although several different methods of calculating height information were performed (e.g. mean, median, and 75^{th} and 95^{th} percentile heights) 75^{th} percentile heights contained the least noise. Nevertheless, the correlation between 75^{th} percentile heights and VII is low, with an r^2 value of 0.16 for all 22 cases (Fig. 46). However, with the exception of three cases (i.e. cases 2, 20, 21), all other cases show maximum values of 75^{th} percentile heights occurring after peaks in radar inferred cell intensity with local maxima in flash heights occurring an average of 5.1 minutes after peaks in total flash rates. This provides strong evidence that the ice available for non-inductive charging is lofted up to higher levels within the storm as the updraft reaches it's maximum velocity as inferred by radar reflectivity and VIL (Greene and Clark, 1972). This leads to a higher positive charge region and increased flash heights. The stronger correlations between flash heights and radar inferred cell intensity

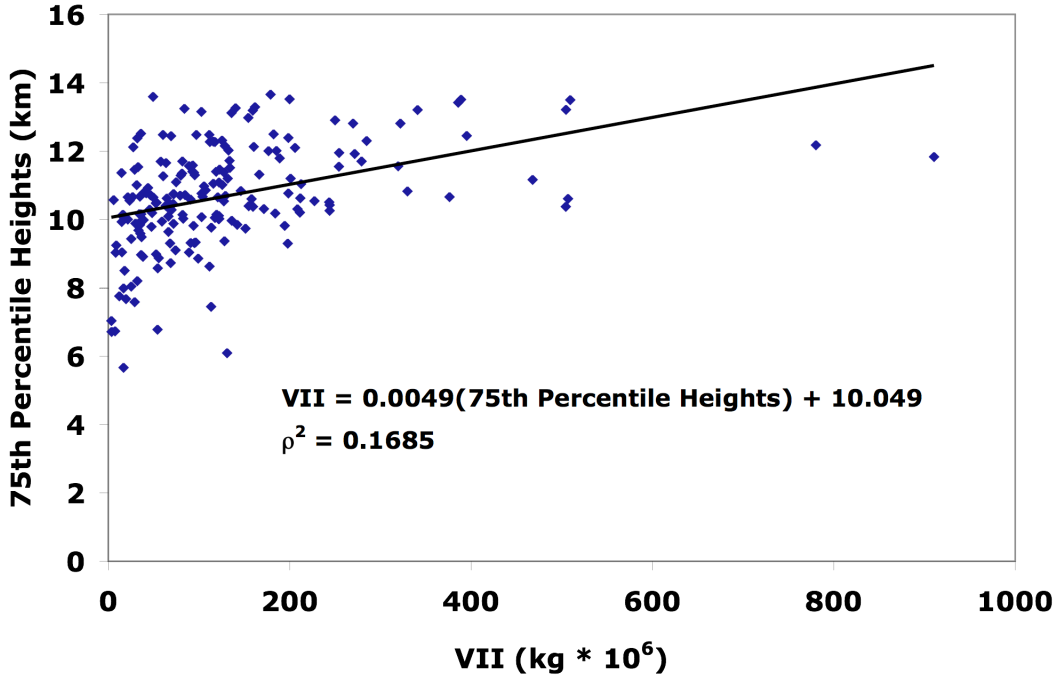

Fig. 46. Scatter plot of VII versus 75th percentile heights for all 22 cases.

observed by Steiger et al. (2005) could be attributed to differences in the microphysics of ordinary and supercellular convection or, differences in the analysis of the data. For example, we examined the entire lifespan of convective cells, which, unlike the pseudo-steady state of a supercell, undergoes significant microphysical and kinematic changes. These major changes likely contribute to the highly variable flash heights observed in our study.

4.1.4 Location of Upper Positive Charge Region

Several cases (cases 3, 4, 5, 14, 15, 19, 20) show an increase in the height of the upper positive charge region, as inferred from VHF source densities, during peak intensity. In addition the majority of the observed cases (cases 3, 5, 6, 7, 8, 9, 10, 14, 15, 19, 20, 22) show a decrease in the upper positive charge region as the cell weakens. These results closely resemble those of Krehbiel et al. (1986), which show an increase in the height of the upper positive charge region during the maximum total flash rate. Our results are consistent with the development of an upper positive charge region as a result of non-inductive charging as ice is lofted to higher portions of the storm with a slow descent of the ice as the storm updrafts weaken.

4.1.5 Correlations Between Total Flash Characteristics and Radar Parameters

The correlation between total ice mass and the total lightning flash rate documented in all 22 cases is similar to previous observations of mid-latitude thunderstorms (MacGorman et al. 1986; Goodman et al. 1988; Williams et al. 1989a; Carey et al. 1996) and is consistent with a non-inductive ice-ice charging mechanism for

particle-scale charge separation (e.g. Takahashi; 1978; Jayaratne et al. 1983; Saunders et al. 1991). Although SHI serves as an indicator of the ice available for charging, the values are typically too low for ordinary convection to provide a reliable source of information for ordinary thunderstorms. VIL, on the other hand, provides an indication of the kinematic properties of the storms (Greene and Clark, 1972), but past results examining CG data suggest it does not appear to serve as a consistently accurate proxy for lightning data (Watson et al. 1995). Our results of total lightning data also show inconsistencies as peaks in VIL do not always correspond to peaks in total flash rate as seen in cases 1, 4, 11, 13 and 18. In case 13, the VIL increases to 10 kg m^{-3} twice during the life cycle of the storm, but the first occurrence corresponds to a flash rate of 0.5 flashes min^{-1} and the second occurrence corresponding to a flash rate of 2.8 flashes min^{-1}. In addition, correlations between maximum radar reflectivity values within a volume scan and total flash rates show very little correlation, with an r-squared value of 0.25 for all 22 cases. Thus, our results suggest that rapid increases in radar inferred cell intensity especially at low levels ($T > 0°$ C) do not necessarily correspond to increased flash rates unless the increase in cell intensity occurs in and above the mixed phase zone ($T < -10°$ C) as represented by VII.

The results from all 22 cases show the temporal evolution in the magnitude of VII closely follows that of the total flash rate. Although other radar reflectivity parameters occasionally follow the trends in total flash rate, the VII is the only variable examined that consistently follows trends in total flash rate. Scatter plots of VII versus total flash rate (Fig. 44a) for both Houston and Dallas show that strong correlations exist between the amount of ice available for non-inductive charging and the total flash rate. Similar to

the results of Carey et al. (2000), lightning is only observed after values of VII exceed 0 kg, suggesting electrification does not occur in the absence of ice. The r^2 values show that VII is responsible for 81% (45%) of the variance in total flash rate in Dallas (Houston). This information provides strong evidence supporting the non-inductive charging hypothesis in addition to showing the ability to infer flash characteristics through the radar inferred microphysics of a convective cloud. Until three-dimensional lightning systems become ubiquitous across the U.S., it appears as though the best proxy for the amount of total lightning occurring within a given storm is the Vertically Integrated Ice mass. However, the assumptions used in the VII calculations (i.e. assumed solid ice density, the assumed intercept parameter for an assumed inverse exponential distribution for ice, and the assumption of a perfectly calibrated radar) leads to potential errors when comparisons of VII are made between different locations.

In effort to test the sensitivity of these assumptions, we adjusted the values of N_o, ρ_i, and Z_e^{ice}, for each case. The results of these adjustments are provided in Appendix A and show that each of the three variables can account for the differences observed in both the slopes and the y-intercepts of the best fit lines between Dallas and Houston cases (Fig. 44a). However, the results show that significant regional differences in the bulk density would have to occur between Dallas and Houston to account for the variations in Fig. 44a. Based on past findings it is unlikely that such significant differences in the bulk density exist between these two locations (e.g. Gilmore et al. 2004). In addition, radar calibration bias can only account for the Dallas Houston variations if the Dallas radar (KFWS) is calibrated approximately 3 dB too high and the Houston radar (KHGX) is calibrated approximately 3 dB too low. Although past studies suggest that this is certainly

possible (Anagnostou et al. 2001), it does not seem extremely likely that the biases would occur in the exact manner to account for the differences between Dallas and Houston. However, N_o definitely appears to be a viable candidate for the observed differences in Fig 44a as variations in N_o are possible within the bounds used in Appendix A (Gilmore et al. 2004). N_o is correlated to particle size, which changes based on the environmental conditions and convective state. Therefore, given the very large effect that adjustments in N_o have on the slopes of the best-fit lines in figure 44a, it seems reasonable to assume the regional differences in slopes are primarily attributed to variations in N_o.

Despite the potential bias originating from the assumptions used in the calculations of VII, it is also possible that the differences between Dallas and Houston cases are a result of physical differences. Examination of Fig. 44 suggests that for a given precipitation ice mass, the flash rate will tend to be higher in Dallas than in Houston. If we assume that VII is calculated perfectly, without any of the potential sources of error discussed above, then it is possible to speculate that thunderstorm charging is more efficient in Dallas when compared to Houston. This could be due to a number of physical reasons, including greater availability of supercooled water or ice crystals in Dallas, which may be plausible due to the more continental environment of Dallas when compared to Houston. The continental environment of Dallas may contribute to a larger availability of condensation nuclei leading to increased number of small hydrometeors. It is also possible that stronger updrafts could lead to more efficient differential sedimentation of charged particles thereby enhancing charge separation. To account for the increase in charge that would likely accompany an increase in the mass flux of a storm, Deierling et al. (2006) examined the correlation of a combined mass flux and

precipitation ice mass estimate to total lightning data. They noted improvements to the correlation by including mass flux, however the significance was not great enough to exclude the utility of VII as a proxy for total lightning flash rates.

However, with all the potential errors and biases in mind, a rather large portion of the bias between Houston in Dallas in Fig. 44 appears to be associated with an anomalously high flash rate case that occurred in Dallas (case 7). This case had the highest flash rate out of any case examined (36.2 flashes min^{-1}; see Table 4), and appears to have a significant influence on the best-fit line in Fig 44. If this case were removed from the sample, the differences in the slopes of the best-fit lines for Dallas and Houston are minimized. In addition, the r^2 value for Dallas decrease from 0.81 to 0.69, suggesting the higher flash rate case had a strong influence on the correlation of the Dallas data. Although we can not say for certain whether or not the slope of the Houston data would change for higher flash rate cases, we can at least speculate that for lower flash rate cases, both the Dallas and Houston total flash rates seem to be similar for a given value of VII (Fig 47).

4.1.6 Benefits of Total, Over CG, Lightning Data

When compared to CG lightning data alone, total lightning data from systems like the LDAR provide a significant increase in the amount of lightning data available for a particular storm. For example cases 1, 6, 11, 18, and 22 all had extremely high IC/CG ratios with and average ratio of 14.3. Considering the case in which only CG data were available, case 11 would have appeared to be an electrically inactive storm, with only 5 CG flashes observed. However, a total of 157 IC flashes were recorded with the LDAR

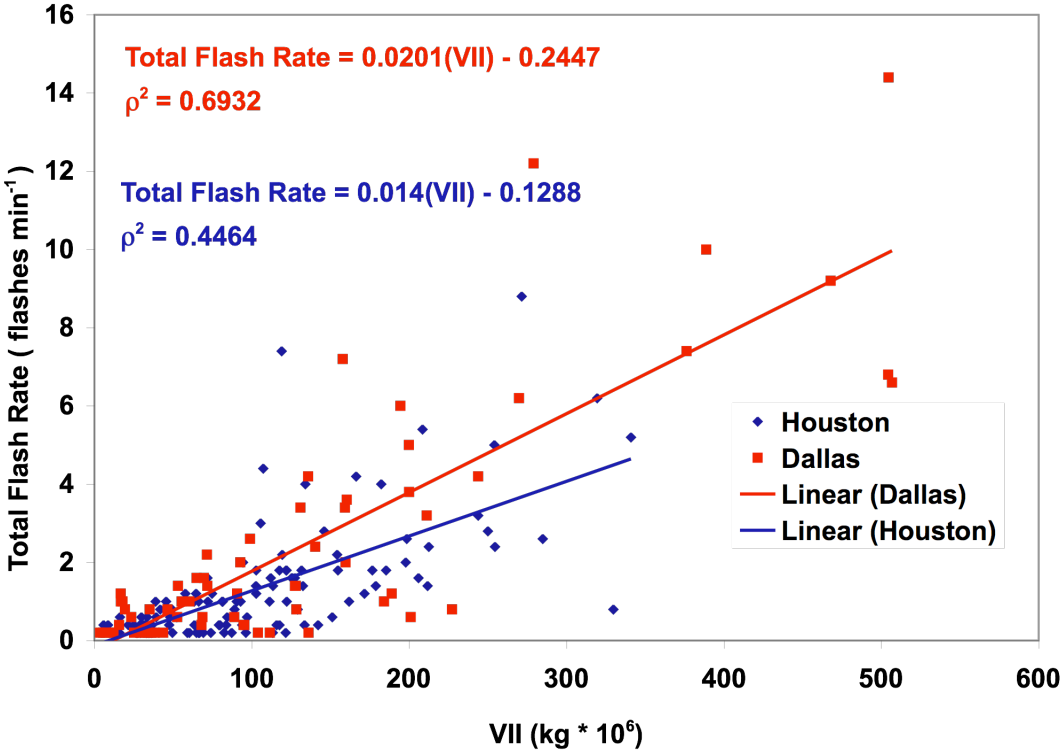

Fig. 47. Similar to Fig. except with the exclusion of case 7.

network, with the first CG occurring 58 minutes after the first LDAR detected source. The inability to acknowledge an electrically active storm such as this poses a significant threat to the aviation industry. This is especially crucial in Houston as three international airports are located within the Houston Metro area (IAH, HOU, and EFD). Therefore, applications in which lightning data is an essential aspect of public safety should strongly consider the use of total, rather than only CG, lightning data. In addition, comparisons between Figs. 44a and 44b suggest that total, rather than CG, lightning is better correlated to VII. Therefore, total lightning is preferred over CG lightning alone for inferences of storm intensity.

4.1.7 CG Lead Times

The average lead time between the first VHF source and first CG was 6 minutes for Dallas and 12 minutes for Houston. The difference between these two times is likely attributed to Houston cases 11 and 13 in which the first IC flashes occurred during very weak initial pulses in the storm's lifecycle. These pulses were apparently sufficient to generate enough charge to produce a few IC flashes, but a quick decrease in radar inferred cell intensity led to a period of no lightning activity. Although this brief increase in cell intensity may have resulted in charge for IC activity, it may not have been sufficient to generate enough ice particles to descend and lead to the subsequent development of the lower positive charge region. The fact that initial peaks in cell intensity for cases 11 and 13 were followed by much stronger increases in cell intensity, suggests that the SCIT algorithm implemented in WDSS-II is an imperfect indicator of identifying cells as defined in the classic airmass thunderstorm model. If we ignore both

case 11 and 13, we find the average time from the first VHF source to the first CG is 6 minutes for Houston, just as it is for the Dallas cases. However, the variability in the delay between the first VHF source and first CG is very high, with a standard deviation of 14 minutes for all 22 cases. These results suggest that the use of the LDAR network to forecast the onset of CG flashes is fairly risky, since the first CG flashes may occur as the first LDAR detected flash, or, in rare cases, may occur before the first LDAR detected source. The LDAR network appears to serve best as an additional tool to be used alongside radar reflectivity information (e.g. Vincent et al. 2003), in effort to effectively forecast the onset of CG flashes.

5. CONCLUSIONS

Past research has yet to uncover the exact processes leading to the development of lightning. According to MacGorman and Rust (1998), the confusion surrounding lightning stems from the inability to sample all the processes responsible for thunderstorm electrification. In addition, storms are extremely complex, with drastic changes occurring on short time scales. Thus, one of the primary objectives of this study was to examine the microphysical, kinematic, and lightning flash characteristics of the most fundamental thunderstorm type: ordinary convective cells.

Using two LDAR total lightning networks (Vaisala's Dallas LDAR network and the TAMU Houston LDAR network) and WSR-88D radars (KFWS, KHGX), we have demonstrated that lightning production in ordinary convection critically linked to the amount of precipitation ice available for non-inductive charging. Although our measurements were remotely measured, we have shown that a clear correlation exists between the vertically integrated ice mass and total lightning.

This was accomplished by increasing the sample size of earlier studies to obtain a higher statistical significance in the correlation between lightning characteristics and radar obtainable parameters. With mounting evidence supporting non-inductive charging (e.g. Takahashi, 1978), much of our emphasis was placed on the amount of ice available in each storm and the possible correlations to the total and CG flash rates. This was accomplished by integrating the radar reflectivity data through the mixed phase zone. The specific scientific findings from the study are as follows:

1) *Vertically Integrated Ice mass (VII) is well correlated to the total flash rate.*

   Rapid increases in radar inferred cell intensity did not have a significant impact

on the total flash rate unless the increase occurred within the mixed phase zone. This supports the idea that non-inductive ice-ice charging is the primary charging mechanism responsible for thunderstorm electrification. This also suggests that VII is best suited for lightning nowcasting or as a means to connect lightning observations to numerical models.

2) *Flash heights show very little correlation to storm intensity or total flash rate.* Peaks in the 75th percentile heights tend to occur after peaks in total flash rates, with an average peak in the heights occurring 5.1 minutes after peaks in total flash rates. However, the magnitude of the increase varies considerably from case to case. The general trend of the 75th percentile heights is for a slow descent as the convective cells weaken, however consistent trends were not evident.

3) *Bimodal distribution of flash heights develop in cases falling in close proximity to the center of the network.*

   This is likely due to the enhanced detection efficiency of the weaker power sources located at lower heights as cases occur closer to the network center. The lower mode suggests the development of a lower positive charge center, which has been shown to be an important factor in the onset of CG flashes. Our results show the development of CG flashes follow the development of the lower mode. The enhanced detection efficiency could lead to misinterpretations in flash height information as lower flashes lead to wide variations on 75th, and 95th percentile height information.

4) *Inferred main positive charge region is responsive to changes in storm intensity.*

   Following past results (e.g. Krehbiel 1986) the upper positive charge region, as inferred from VHF source density, is shown to increase in height as the total flash rate increases. Twelve out of the twenty-two cases show noticeable correlations between the inferred positive charge region and convective state (e.g. cumulus, mature, or dissipating stages). The upper positive charge regions typically reaches maximum heights after the radar inferred mature stage and subsequent lowering during the dissipating stage.

5) *Cases follow the conventional model of cell and lightning development.*

   IC lightning dominates during the initial stages of thunderstorm electrification in 18 out of the 22 cells examined. An average of 19 IC flashes occur before the first CG. The average lead-time from the first VHF source to the first NLDN detected CG is 6 minutes for Dallas cases and 12 minutes for Houston case. Slightly higher lead times occur in Houston due to a few cases that experienced a few IC flashes during initial weak pulses, with a subsequent end to all lightning activity until the next pulse occurs. Since there are questions as to whether these cells were truly individual ordinary convective cells, we also present the findings if these cases are ignored, which gives an average lead-time of 6 minutes for Houston cases.

6) *Total lightning data provides a significant increase to the amount of lightning data available from CG data alone.*

   Several cases show average CG/IC ratios less than 10%, which may appear as electrically inactive storms if only CG data are available. This is particularly important when considering that higher IC flash rates do not necessarily

correspond to higher CG flash rates, and often times the exact opposite is observed. Therefore, a binary yes no response to whether a storm has IC lightning based on the occurrence of CG lightning could prove disastrous to applications in which IC lightning is a safety hazard, such as the aviation industry.

Integration of the results from this study into operational forecast settings could lead to improvements in the nowcasting of lightning threats using radar, numerical weather prediction via the assimilation of total lightning data, and the nowcasting of severe weather and lightning hazards to aviation. Future work may consider examining some of the "null" cases discovered through this project, in which detected lightning was absent in cases that displayed radar reflectivity values above 30 dBZ in the mixed phase zone. Due to the incredibly robust correlation between trends in VII and total flash rate, it is possible that VII could serve as an advanced warning tool for the onset of lightning, especially when used in conjunction with other radar observable parameters (e.g. echo top height, height of radar reflectivity values in relation to isotherm levels, SHI, VIL). Moreover, future work may further explore the utility of flash height information and whether the information flash heights provide is dependent on the convective mode. In addition, acquiring total lightning information on additional isolated ordinary convective cells could provide a more statistically significant data set, which may reduce some of the discrepancies noted between Dallas and Houston networks.

REFERENCES

Amburn, S. A., P. L. Wolf, 1997: VIL density as a hail indicator. Weather and Forecasting, 12, 473-478.

Anagnostou, E.N., C.A. Morales, T. Dinku, 2001: The use of TRMM precipitation radar observations in determining ground radar calibration biases. Journal of Atmospheric and Oceanic Technology, 18, 616-628.

Avila, E. E., G. G. A. Varela, G. M. Caranti, 1995: Temperature dependence of static charging in ice growing by riming. Journal of the Atmospheric Sciences, 52, 4515-4522.

Avila, E. E., C. P. R. Saunders, H. Bax-Norman, N. E. Castellano, 2005: Charge sign reversal in irregular ice particle-graupel collisions. Geophysical Research Letters, 32

Baker, B., M. B. Baker, E. R. Jayaratne, J. Latham, C. P. R. Saunders, 1987: The influence of diffusional growth-rates on the charge-transfer accompanying rebounding collisions between ice crystals and soft hailstones. Quarterly Journal of the Royal Meteorological Society, 113, 1193-1215.

Baker, M. B., J. G. Dash, 1989: Charge-transfer in thunderstorms and the surface melting of ice. Journal of Crystal Growth, 97, 770-776.

Boccippio, D. J., 2002: Lightning scaling relations revisited. Journal of the Atmospheric Sciences, 59, 1086-1104.

Bringi, V. N., K. Knupp, A. Detwiler, L. Liu, I. J. Caylor, and R. A. Black, 1997: Evolution of a Florida thunderstorm during the convection and precipitation/electrification experiment: The case study of 9 August 1991. Monthly Weather Review., 125**,** 2131–2160.

Brown, R. A., V. T. Wood, D. Sirmans, 2000a: Improved WSR-88D scanning strategies for convective storms. Weather and Forecasting, 15, 208-220.

Brown, R. A., J. M. Janish, V. T. Wood, 2000b: Impact of WSR-88D scanning strategies on severe storm algorithms. Weather and Forecasting, 15, 90-102.

Buechler, D. E., S. J. Goodman, 1990: Echo size and asymmetry - impact on NEXRAD storm identification. Journal of Applied Meteorology, 29, 962-969.

Carey, L. D., S. A. Rutledge, 1996: A multiparameter radar case study of the microphysical and kinematic evolution of a lightning producing storm. Meteorology and Atmospheric Physics, 59, 33-64.

Carey, L. D., S. A. Rutledge, 2000: The relationship between precipitation and lightning in tropical island convection: A C-band polarimetric radar study. Monthly Weather Review, 128, 2687-2710.

Carey, L. D., S. A. Rutledge, 2003: Characteristics of cloud-to-ground lightning in severe and nonsevere storms over the central United States from 1989-1998. Journal of Geophysical Research-Atmospheres, 108

Carey, L. D., M. J. Murphy, T. L. McCormick, N. W. S. Demetriades, 2005: Lightning location relative to storm structure in a leading-line, trailing-stratiform mesoscale convective system. Journal of Geophysical Research-Atmospheres, 110, D03105, doi:10.1029/2003JD00437

Cheze, J. L., H. Sauvageot, 1997: Area-average rainfall and lightning activity. Journal of Geophysical Research-Atmospheres, 102, 1707-1715.

Christian, H., C. R. Holmes, J. W. Bullock, W. Gaskell, A. J. Illingworth, J. Latham, 1980: Airborne and ground-based studies of thunderstorms in the vicinity of Langmuir Laboratory. Quarterly Journal of the Royal Meteorological Society, 106, 159-174.

Coleman, L. M., T. C. Marshall, M. Stolzenburg, T. Hamlin, P. R. Krehbiel, W. Rison, R. J. Thomas, 2003: Effects of charge and electrostatic potential on lightning propagation. Journal of Geophysical Research-Atmospheres, 108

Crabb, J. A., J. Latham, 1974: Corona from colliding drops as a possible mechanism for triggering of lightning. Quarterly Journal of the Royal Meteorological Society, 100, 191-202.

Cressman, G., 1959: An operational analysis system. Monthly Weather Review, 87, 367-374.

Cummins, K. L., M. J. Murphy, E. A. Bardo, W. L. Hiscox, R. B. Pyle, A. E. Pifer, 1998: A combined TOA/MDF technology upgrade of the US National Lightning Detection Network. Journal of Geophysical Research-Atmospheres, 103, 9035-9044.

Cummins, K. L., J. A. Cramer, C. J. Biagi, E. P. Krider, J. Jerauld, M. A. Uman, V. A. Rakov, 2006: The U.S. National Lightning Detection Network: Post-upgrade status. Preprints, 2nd Conf. on Meteorological Applications of Lightning Data, Atlanta, GA, American Meteorological Society, CD-ROM, 6.1.

Curran, E. B., R. L. Holle, R. E. Lopez, 2000: Lightning casualties and damages in the United States from 1959 to 1994. Journal of Climate, 13, 3448-3464.

Demetriades, N., M. J. Murphy, K. L. Cummins, 2001: Cloud and cloud-to-ground lightning detection at LF and VHF: Early results from Global Atmospherics Dallas-Fort Worth LDAR II and IMPACT/ESP research networks. Eos Trans. AGU, 82, Abstract AE21A-07.

Deierling W., W. A. Peterson, J. Latham, S. M. Ellis, H. J. Christian Jr., 2006: Towards the relationship between total lightning activity and downward as well as upward ice mass fluxes in thunderstorms. American Meteorological Society, 1st Met. Light Conf. Paper P8.4.

Dye, J. E., J. J. Jones, W. P. Winn, T. A. Cerni, B. Gardiner, D. Lamb, R. L. Pitter, J. Hallett, C. P. R. Sunders, 1986: Early electrification and precipitation development in a small, isolated Montana cumulonimbus. Journal of Geophysical Research, 91, 1231-1247.

Dye, J. E., A. J. Weinheimer, W.P. Winn, 1988: Observations within 2 regions of charge during initial thunderstorm electrification. Quarterly Journal of the Royal Meteorological Society, 114, 1271-1290.

Dye, J. E., W. P. Winn, J. J. Jones, D. W. Breed, 1989: The electrification of New Mexico thunderstorms .1. Relationship between precipitation development and the onset of electrification. Journal of Geophysical Research-Atmospheres, 94, 8643-8656.

Ely, B. L., R. E. Orville, L. D Carey, 2006: Houston LDAR network performance, data usage, and first results. Second Conference on the Meteorological Applications of Lightning Data, Paper P2.3.

Gaskell, W., 1981: A laboratory study of the inductive theory of thunderstorm electrification. Quarterly Journal of the Royal Meteorological Society, 107, 955-966.

Gaskell, W., A. J. Illingworth, J. Latham, C. B. Moore, 1978: Airborne studies of electric-fields and charge and size of precipitation elements in thunderstorms. Quarterly Journal of the Royal Meteorological Society, 104, 447-460.

Gaskell, W., A. J. Illingworth, 1980: Charge-transfer accompanying individual collisions between ice particles and its role in thunderstorm electrification. Quarterly Journal of the Royal Meteorological Society, 106, 841-854.

Gilmore, M. S., J. M. Straka, E. N. Rasmussen, 2004: Precipitation uncertainty due to variations in precipitation particle parameters within a simple microphysics scheme. Monthly Weather Review, 132, 2610-2627.

Goodman, S. J., D. E. Buechler, P. D. Wright, W. D. Rust, 1988: Lightning and precipitation history of a microburst-producing storm. Geophysical Research Letters, 15, 1185-1188.

Greene, D. R., R. A. Clark, 1972: Vertically integrated liquid water--A new analysis tool. Monthly Weather Review, 100, 548-552.

Gremillion, M. S., R. E. Orville, 1999: Thunderstorm characteristics of cloud-to-ground lightning at the Kennedy Space Center, Florida: A study of lightning initiation signatures as indicated by the WSR-88D. Weather and Forecasting, 14, 640-649.

Hobbs, P. V., S. Chang, Locatell.Jd, 1974: Dimensions and aggregation of ice crystals in natural clouds. Journal of Geophysical Research, 79, 2199-2206.

Hondl, K. D., 2003: Capabilities and components of the Warning Decision Support System – Integrated Information (WDSS-II). Preprints, 19th Conf. On Interactive Info. Processing Systems, Long Beach, CA, American Meteorological Society, CD preprints.

Hondl, K. D., M. D. Eilts, 1994: Doppler radar signatures of developing thunderstorms and their potential to indicate the onset of cloud-to-ground lightning. Monthly Weather Review, 122, 1818-1836.

Illingworth, A. J., J. M. Caranti, 1985: Ice conductivity restraints on the inductive theory of thunderstorm electrification. Journal of Geophysical Research-Atmospheres, 90, 6033-6039.

Jameson, A. R., M. J. Murphy, E. P. Krider, 1996: Multiple-parameter radar observations of isolated Florida thunderstorms during the onset of electrification. Journal of Applied Meteorology, 35, 343-354.

Jayaratne, E. R., C. P. R. Saunders, J. Hallett, 1983: Laboratory studies of the charging of soft-hail during ice crystal interactions. Quarterly Journal of the Royal Meteorological Society, 109, 609-630.

Jayaratne, E. R. and C. P. R. Saunders, 1985: The rain gush, lightning, and the lower positive center in thunderstorms - reply. Journal of Geophysical Research-Atmospheres, 90, 10755-10755.

Johnson, J. T., P.L. MacKeen, A. Witt, E. D. Mitchell, G. J. Stumpf, M. D. Eilts, K. W. Thomas, 1988: The storm cell identification and tracking algorithm: An enhanced WSR-88D algorithm. Weather and Forecasting, 13, 263-276.

Keith, W. D., C. P. R. Saunders, 1990: Charging of aircraft - high-velocity collisions. Journal of Aircraft, 27, 218-222.

Khain, A., M. Pinsky, M. Shapiro, A. Pokrovsky, 2001: Collision rate of small graupel and water drops. Journal of the Atmospheric Sciences, 58, 2571-2595.

Kingsmill, D. E., R. M. Wakimoto, 1991: Kinematic, dynamic, and thermodynamic analysis of a weakly sheared severe thunderstorm over Northern Alabama. Monthly Weather Review, 119, 262-297.

Krehbiel, P. R., 1986: The Electrical Structure of Thunderstorms, in The Earth's Electrical Environment. Nat'l. Academy Press, Washington D.C.

Lang, T. J., L. J. Miller, M. Weisman, S. A. Rutledge, L. J. Barker, V. N. Bringi, V. Chandrasekar, A. Detwiler, N. Doesken, J. Helsdon, C. Knight, P. Krehbiel, W. A. Lyons, D. MacGorman, E. Rasmussen, W. Rison, W. D. Rust, R. J. Thomas, 2004a: The severe thunderstorm electrification and precipitation study. Bulletin of the American Meteorological Society, 85, 1107.

Lang, T. J., S. A. Rutledge, K. C. Wiens 2004b: Origins of positive cloud-to-ground lightning flashes in the stratiform region of a mesoscale convective system. Geophysical Research Letters, 31, L10105, 10.1029/2004GL019823.

Lhermitte, R., E. Williams, 1985: Thunderstorm electrification - a case-study. Journal of Geophysical Research-Atmospheres, 90, 6071-6078.

MacGorman, D. R., A. A. Few, T. L. Teer, 1981: Layered lightning activity. Journal of Geophysical Research-Oceans and Atmospheres, 86, 9900-9910.

MacGorman, D. R., W. D. Rust, 1998: The Electrical Nature of Storms. Oxford University Press, 422 pp.

Marshall, J. S., W. M. Palmer, 1948: The distribution of raindrops with size. Journal of Meteorology, 5, 165-166.

Marshall, T. C., W. P. Winn, 1982: Measurements of charged precipitation in a New-Mexico thunderstorm - lower positive charge centers. Journal of Geophysical Research-Oceans and Atmospheres, 87, 7141-7157.

Marshall, T. C., M. P. Mccarthy, W. D. Rust, 1995: Electric-field magnitudes and lightning initiation in thunderstorms. Journal of Geophysical Research-Atmospheres, 100, 7097-7103.

Marshall, T. C., M. Stolzenburg, C. R. Maggio, L. M. Coleman, P. R. Krehbiel, T. Hamlin, R. J. Thomas, W. Rison, 2005: Observed electric fields associated with lightning initiation. Geophysical Research Letters, 32, doi: 10.1029/2004GL021802.

Mazur, V., E. Williams, R. Boldi, L. Maier, D. E. Proctor, 1997: Initial comparison of lightning mapping with operational time-of-arrival and interferometric systems. Journal of Geophysical Research-Atmospheres, 102, 11071-11085.

McCormick, T. L., 2003: Three-dimensional radar and total lightning characteristics of mesoscale convective systems, M.S. thesis, Dept. of Marine, Earth, and Atmospheric Sciences, North Carolina State University

Orville, R. E., G. R. Huffines, 1999: Lightning ground flash measurements over the contiguous United States: 1995-97. Monthly Weather Review, 127, 2693-2703.

Orville, R. E., G. R. Huffines, 2001: Cloud-to-ground lightning in the United States: NLDN results in the first decade, 1989-98. Monthly Weather Review, 129, 1179-1193.

Oye, D., M. Cases, 1995: REORDER: A program for gridding radar data. Installation and use manual for the UNIX version. NCAR Atmospheric Technology Division, Boulder CO, 19pp.

Pflaum, J. C., H. R. Pruppacher, 1979: Wind-tunnel investigation of the growth of graupel initiated from frozen drops. Journal of the Atmospheric Sciences, 36, 680-689.

Proctor, D. E., 1971: A hyperbolic system for obtaining VHF radio pictures of lightning. Journal of Geophysical Research, 76, 1478-1489.

Proctor, D. E., 1991: Regions where lightning flashes began. Journal of Geophysical Research-Atmospheres, 96, 5099-5112.

Pruppacher, H. R., J. D. Klett, 1997: Microphysics of Clouds and Precipitation. 2nd rev. and enl. ed. Atmospheric and Oceanographic Sciences Library; v. 18, Kluwer Academic Publishers, xx, 954pp.

Rakov, V. A., M. A. Uman, 2003: Lightning: Physics and Effects. Cambridge University Press.

Ray, P. S., 1986: Mesoscale Meteorology and Forecasting. American Meteorological Society, xi, 793pp.

Ray, P. S., D. R. Macgorman, W. D. Rust, W. L. Taylor, L. W. Rasmussen, 1987: Lightning location relative to storm structure in a supercell storm and a multicell storm. Journal of Geophysical Research-Atmospheres, 92, 5713-5724.

Reynolds, S. E., M. Brook, M. F. Gourley, 1957: Thunderstorm charge separation. Journal of Meteorology, 14, 426-436.

Rinehart, R. E., 2004: Radar for meteorologists. 3d ed. Rinehart Publications.

Rison, W., R. J. Thomas, P. R. Krehbiel, T. Hamlin, J. Harlin, 1999: A GPS-based three-dimensional lightning mapping system: Initial observations in central New Mexico. Geophysical Research Letters, 26, 3573-3576.

Rutledge, S. A., E. R. Williams, T. D. Keenan, 1992: The down under Doppler and Electricity Experiment (Dundee) - Overview and preliminary-results. Bulletin of the American Meteorological Society, 73, 3-16.

Sartor, D., 1954: A laboratory investigation of collision efficiencies, coalescence and electrical charging of simulated cloud droplets. Journal of Meteorology, 11, 91-103.

Saunders, C. P. R., M. F. S. Wheeler, N. Jallo, E. R. Jayaratne, 1985: Ice crystal interactions with a riming target - charge-transfer and collection efficiencies. Journal of Geophysical Research-Atmospheres, 90, 6047-6050.

Saunders, C. P. R., W. D. Keith, R. P. Mitzeva, 1991: The effect of liquid water on thunderstorm charging. Journal of Geophysical Research-Atmospheres, 96, 11007-11017.

Saunders, C. P. R., I. M. Brooks, 1992: The effects of high liquid water-content on thunderstorm charging. Journal of Geophysical Research-Atmospheres, 97, 14671-14676.

Saunders, C. P. R., 1993: A review of thunderstorm electrification processes. Journal of Applied Meteorology, 32, 642-655.

Saunders, C. P. R., S. L. Peck, 1998: Laboratory studies of the influence of the rime accretion rate on charge transfer during crystal/graupel collisions. Journal of Geophysical Research-Atmospheres, 103, 13949-13956.

Shao, X. M., P. R. Krehbiel, 1996: The spatial and temporal development of intracloud lightning. Journal of Geophysical Research-Atmospheres, 101, 26641-26668.

Steiger, S. M., R. E. Orivlle, M. J. Murphy, N. W. S. Demetriades, 2005: Total lightning and radar characteristics of supercells: Insights on electrification and severe weather forecasting. American Meteorological Society, Conference on the Meteorological Applications of Lightning Data, Paper P1.7.

Stolzenburg, M., W. D. Rust, T. C. Marshall, 1998: Electrical structure in thunderstorm convective regions - 3. Synthesis. Journal of Geophysical Research-Atmospheres, 103, 14097-14108.

Takahashi, T., 1978: Riming electrification as a charge generation mechanism in thunderstorms. Journal of the Atmospheric Sciences, 35, 1536-1548.

Takahashi, T., 1984: Thunderstorm electrification - a numerical study. Journal of the Atmospheric Sciences, 41, 2541-2558.

Takahashi, T., T. Tajiri, Y. Sonoi, 1999: Charges on graupel and snow crystals and the electrical structure of winter thunderstorms. Journal of the Atmospheric Sciences, 56, 1561-1578.

Taylor, W. L., E. A. Brandes, W. D. Rust, D. R. MacGorman, 1984: Lightning activity and severe storm structure. Geophysical Research Letters, 11, 545-548.

Thomas, R. J., P. N. Krehbiel, W. Rison, T. Hamlin, J. Harlin, D. Shown, 2001: Observations of VHF source powers radiated by lightning. Geophysical Research Letters, 28, 143-146.

Thomas, R., P. Krehbiel, W. Rison, J. Harlin, T. Hamlin, N. Campbell, 2003: The LMA flash algorithm. Versailles, France, International Commission on Atmospheric Electricity, 655-656.

Tuttle, J. D., V. N. Bringi, H. D. Orville, F. J. Kopp, 1989: Multiparameter radar study of a microburst - comparison with model results. Journal of the Atmospheric Sciences, 46, 601-620.

Uman, M. A., 1986: All About Lightning. General Publishing Company.

Uman, M. A., 1987: The Lightning Discharge. International Geophysics Series ; v. 39, Academic Press, xii, 377pp.

United States. Weather Bureau., H. R. Byers, R. R. Braham, and Thunderstorm Project (U.S.). 1949: The Thunderstorm. Report of the Thunderstorm Project. U.S. Government Printing Office, 287pp.

Vincent, B. R., L. D. Carey, D. Schneider, K. Keeter, R. Gonski, 2003: Using WSR-88D reflectivity data for the prediction of cloud-to-ground lightning: A central North Carolina study. National Weather Digest, 27, 35-44.

Vonnegut, B., 1963: Some facts and speculation concerning the origin and role of thunderstorm electricity. Meteorological Monographs, 5, 224-241.

Wacker, R. S., R. E. Orville, 1999: Changes in measured lightning flash count and return stroke peak current after the 1994 U.S. National Lightning Detection Network upgrade - 2. Theory. Journal of Geophysical Research-Atmospheres, 104, 2159-2162.

Watson, A. I., R. L. Holle, R. E. Lopez, 1995: Lightning from 2 national detection networks related to vertically integrated liquid and echo-top information from WSR-88D radar. Weather and Forecasting, 10, 592-605.

Weisman, M. L., J. B. Klemp, 1982: The dependence of numerically simulated convective storms on vertical wind shear and buoyancy. Monthly Weather Review, 110, 504-520.

Williams, E. R., M. E. Weber, R. E. Orville, 1989a: The relationship between lightning type and convective state of thunderclouds. Journal of Geophysical Research-Atmospheres, 94, 13213-13220.

Williams, E. R.,1989b: The tripole structure of thunderstorms. Journal of Geophysical Research-Atmospheres, 94, 13151-13167.

Williams, E. R., 2001: The electrification of severe storms. Chapter 13 in Severe Convective Storms, Ed., C.A. Doswell, III, Meteorological Monongraph, 28, 527-561.

Witt, A., M. D. Eilts, G. J. Stumpf, J. T. Johnson, E. D. Mitchell, K. W. Thomas, 1998: An enhanced hail detection algorithm for the WSR-88D. Weather and Forecasting, 13, 286-303.

Workman, E. J., S. E. Reynolds, 1949: Electrical activity as related to thunderstorm cell growth. Physical Review, 74, 1231-1232.

APPENDIX A

In effort to examine the amount of precipitation ice available for non-inductive charging, a measure of the vertically integrated ice (VII) was employed for this study. As discussed in Carey and Rutledge (2000) and section 2.3.3, the VII is given by:

$$VII = 1000\pi\rho_i N_o^{3/7}\left(\frac{5.28\times10^{-18}}{720}\right)^{4/7}\int_{-10^\circ}^{h_{top}}(Z_e^{ice})^{4/7}dh$$

where Z_e^{ice} is the equivalent radar reflectivity factor, N_o is the intercept parameter for an assumed inverse exponential distribution for ice (4.0×10^6; Carey and Rutledge 2000), and ρ_i is the assumed solid ice density (0.917×10^6 g m^{-3}). Calculations of VII were obtained from each radar volume scan during the lifespan of all 22 cases. This information was then compared to the total and CG flash rate to test for possible correlations between lightning flash rate and VII (Figs. 44a,b). Linear regression lines were placed on the plots and display noticeable variations in slope, and to a lesser extent y-intercept, between both Dallas and Houston. The differences noted between these two locations could be due to a number of issues including regional biases in the in the microphysics and kinematics driving lightning production, the VHF detection efficiencies of each network, or the calibration of the radars. However, without in-situ measurements, it is not possible to know whether are assumed values of N_o, ρ_i, are representative of the microphysics and kinematics of *both* locations.

The differences in slopes between Houston in Dallas are present with both LDAR data (Fig. 44a) and NLDN data (Fig 44b). These similarities make it difficult to believe

that the network errors are responsible for the difference in slope, since two separate networks would need to produce similar biases. However, since the actual values of N_o and ρ_i likely varied as each convective cell evolved through its lifespan, it is more likely that the assumptions used in the calculation of VII account for the observed differences.

In effort to test the sensitivity of cloud microphysical assumptions (N_o, ρ_i) and radar calibration errors (Z_e^{ice} [bias]), adjustments were made to N_o, ρ_i, and Z_e^{ice} based on reasonable values suggested by previous research. Within thunderstorms the internal structure of the riming hail or graupel is a function of the impact velocity, water drop size, air temperature, and particle temperature (Pflaum and Pruppacher 1979; Gilmore et al. 2004). All of these factors can contribute to the variations in the bulk particle density within convective cells, which leads to a wide variation of accepted bulk particle densities reviewed in past studies (Pruppacher and Klett 1997; Gilmore et al. 2004). According to Pruppacher and Klett (1997) the observed bulk particle densities for hail range from 0.70-0.90×10^6 g m^{-3} and range from 0.50-0.89×10^6 g m^{-3} for graupel. Wide variability in the hail and graupel intercept parameters has also been documented with ranges from 10^2 m^{-4} to 10^{10} m^{-4} (Gilmore et al. 2004). In addition to differences in assumed storm microphysics, errors in VII may also arise from errors in radar power calibration, which are not uncommon for the WSR-88D (Anagnostou et al. 2001). Anagnostou et al. used the Tropical Rainfall Measuring Mission (TRMM) satellite to examine WSR-88D bias. They found systematic differences between +2 and -7 dB. Therefore, it was generally assumed that an error of ±3 dB for KFWS and KHGX was a reasonable estimate to test for variations in the slopes between Houston and Dallas cases.

Tests of the sensitivity of VII to each variable were performed by adjusting the original values based on the aforementioned observations in the variations in N_o, ρ_i, and Z_e^{ice}. For the test, each variable was adjusted while the other two variables were held at their original value. The adjustments made are as follows:

$\boldsymbol{N_o}$ - Original Value: 4.0×10^6
Upper Limit: 4.0×10^7
Lower Limit: 4.0×10^5

$\boldsymbol{\rho_i}$ – Original Value: 0.917×10^6 g m^{-3}
Lower Limit: 0.417×10^6 g m^{-3}

Z_e^{ice} - Original Value: No bias adjustment
Assumed dB bias: +3 dB
Assumed dB bias: -3 dB

The results from the adjustments are depicted in Figs. A1, A2, and A3. Figure A1 shows that in order for errors in the calibration of KHGX and KFWS to account for the differences in slope, both radars would have to have an approximate 3 dB calibration error of opposite sign (i.e., with KHGX being calibrated 3 dB too low and KFWS being calibrated 3 dB to high). Therefore it seems fairly unlikely that calibration effects alone can account for the difference in best fit lines in Figs. 44a,b. Similar results are noted in ρ_i, (Fig. A2) in that the effect of lowering ρ_i results in changes to the slopes that are unlikely to account for the extent of the differences observed. The adjustments on N_o, however, show a very wide variation in the slopes for both Houston and Dallas (Fig. A3). Therefore, the results suggest that errors in the assumed values of N_o, are the most likely parameter to account for the differences in slopes. However, it is also possible that a combination of error from all three parameter contributed to the differences seen in Figs.

44a, b

Although our assumed values likely contain errors, this study examines the trends in the storm integrated ice mass as it relates to lightning characteristics. Therefore, it is assumed that the assumptions and calculations used are sufficient.

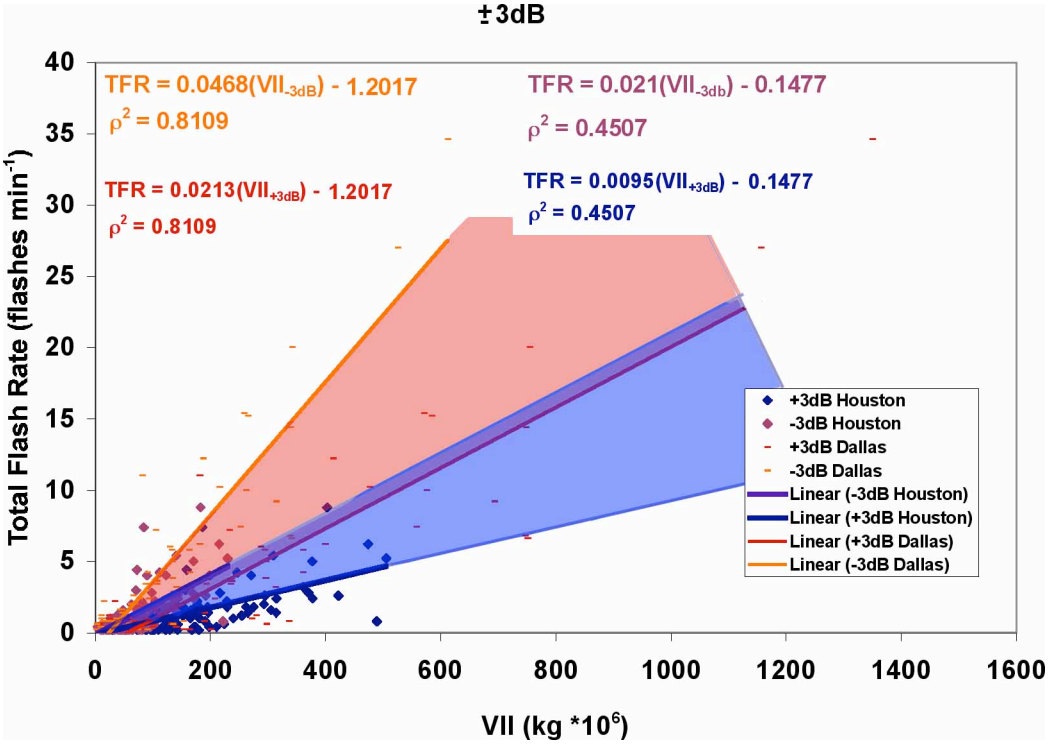

Fig. A1. Similar to figure 44 except values of Z_e^{ice} are adjusted by ±3 dB in eqn. (14). -3 dB means 3 dB were subtracted from the observed value of Z_e^{ice} and +3 dB means 3 dB were added to the observed value of Z_e^{ice}. Houston points are represented by blue (purple) diamonds for +3 dB (-3 dB) and Dallas points are represented by short, red (orange) lines for +3 dB (-3 dB) all of which are visible. Best-fit lines are shown for each scatter with the area spanning the slopes Houston (Dallas) highlighted in blue (red).

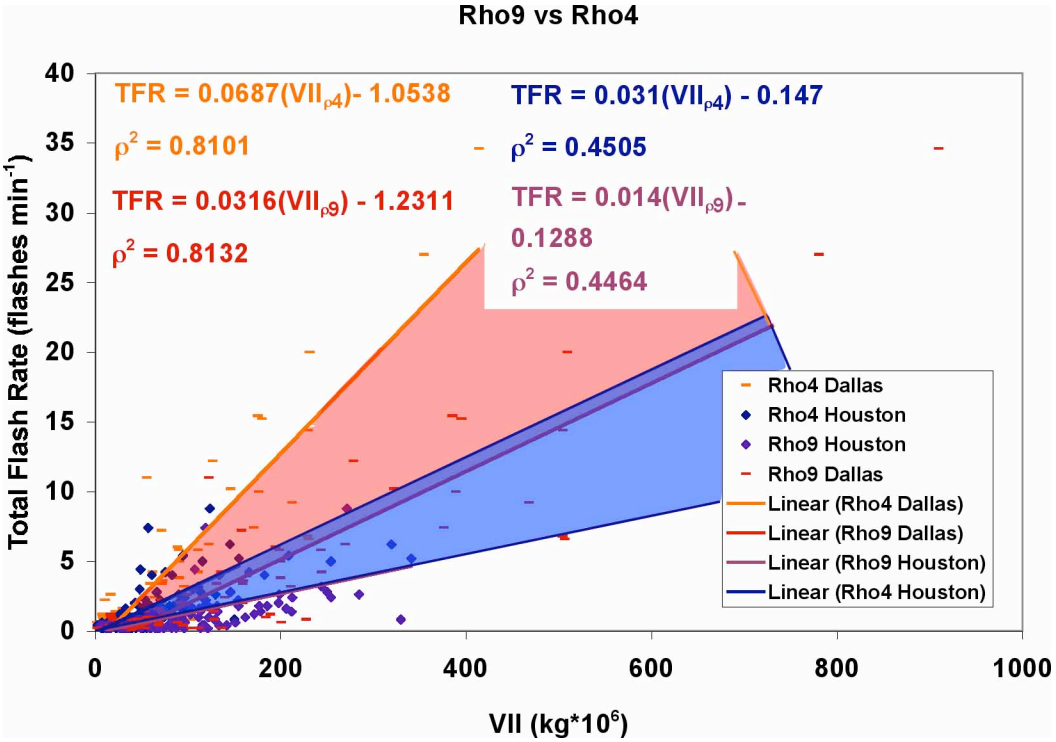

Fig. A2. Similar to A1 except for different values of ρ_i.

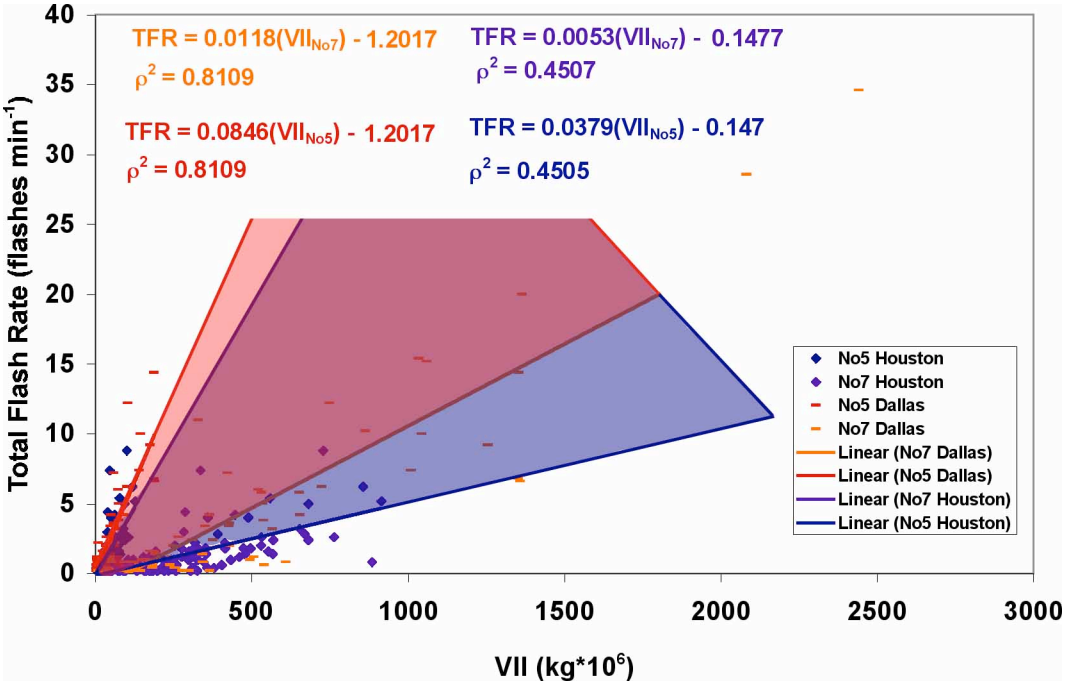

Fig. A3. Similar to A1 except for different values of N_o.

VITA

Shane Motley was born on the 25th day of July 1979 to Dr. and Mrs. Michael T. Motley of Davis, CA. He graduated from Davis Senior High School in June 1998.

In December of 2002, Shane Motley received his B.S. degree in atmospheric sciences from the University of California at Davis. He spent the following two quarters in post-graduate research at UC Davis. He received his M.S. degree in atmospheric sciences from Texas A&M in August 2006. His current address is:

512 Citadel

Davis, CA 95616